Investigating the origin of a Greenland ice core geochemical anomaly near the Bølling-Allerød/Younger Dryas boundary

GREEN, CHARLOTTE,EMILY

Investigating the origin of a Greenland ice core geochemical anomaly near the Bølling-Allerød/Younger Dryas boundary

By

Charlotte Emily Green

Thesis

For the degree of:

Master of Science by Research

Department of Earth Sciences

Durham University

2019

Investigating the origin of a Greenland ice core geochemical anomaly near the Bølling-Allerød/Younger Dryas boundary

Charlotte E. Green

The source of a platinum peak identified in the Greenland Ice Sheet Project 2 (GISP2) ice core that occurs almost synchronously with Younger Dryas (YD) cooling is poorly understood. The GISP2 Pt spike is associated with high platinum/iridium (Pt/Ir) and platinum/aluminium (Pt/Al) ratios, and previous research attributed the anomaly to an unusual iron-rich Ir-poor meteorite impact. The Pt spike timing is also broadly contemporaneous with the Laacher See eruption (LSE), Germany, suggesting a possible source. However, this link is understudied because of perceived chronological mismatches (reconciled recently), and the lack of Pt and Ir data from the Laacher See tephra (LST). To explore this link further, proximal tephra deposits from the LSE were sampled at localities around the volcano and the relevant geochemistry analysed. This report presents evidence that the LSE is not the Pt spike source because: i) the LST has low Pt concentrations, ii) the LST's geochemical ratios are dissimilar to the GISP2 Pt spike and iii) conversion of the Pt spike timing to the newest ice core age-depth model shows a chronological offset of ~60 years between the two events. Further comparison of the Pt spike's geochemical ratios against magmas and meteorites, YD Boundary sediments and others suggests that the Pt spike geochemistry is incomparable to any known source. Therefore, the Pt spike origin is interpreted as either: i) a noncataclysmic impact of an undiscovered iron meteorite or ii) an unidentified Pt-rich volcanic eruption contemporaneous with the anomaly, whose aerosol fractionated in the atmosphere or ice. This report supports the LSE as the simplest explanation for the YD trigger, because the LSE was synchronous with Greenland Stadial-1 (GS-1) and contained enough sulfur to cause substantial cooling. The event resulting in the Pt spike occurred ~60 years after GS-1 cooling, and was therefore not the primary trigger. The Pt spike may however represent a subsequent radiative cooling event that prolonged the YD.

Table of Contents

Acknowledgements

This research project was supported by funding from Prof. James Baldini and Dr. Richard Brown, Department of Earth Sciences, Durham University.

A huge thank you to my supervisors James and Rich for their guidance throughout the duration of the project, and for answering my endless questions (no matter how small). This year helped me realise I wanted to continue with further study through a PhD, and I have James and Rich, amongst others in the department, to thank for the inspiring discussions that fuelled this decision. I would also like to thank Hans-Ulrich Schmincke and Mari Sumita for their indispensable help on fieldwork and compelling discussions throughout; their knowledge of the local area, the Laacher See eruption and its tephra deposits ensured we got all the samples needed in good time, which ultimately helped the project run smoothly. Special thanks are due to Thomas Miesel, for helping with data interpretation and aiding my understanding of geochemistry, and to Michail Petaev for the discussion of the original GISP2 ice core data in his paper. Lastly, I'd like to thank everyone I've met along the way, particularly my friends in the department who have navigated through their own journeys this year as well.

1. Introduction

During the last deglaciation, the period ~12.9-11.7 ka BP was characterised by an abrupt return to cold conditions across the North Atlantic and Europe known as the Younger Dryas (YD) climate anomaly (Rasmussen et al, 2006; Carlson, 2013). A reduction in North Atlantic deep-water (NADW) formation (Boyle & Keigwin, 1987; Lowe & Walker, 2014) coupled with sea ice growth may explain much of the YD's climate signature, but the trigger of this reorganisation is poorly understood (Broecker, 2006a, Broecker et al. 2010). The most extensively studied hypothesis involves a meltwater pulse that caused Atlantic Meridional Overturning Circulation (AMOC) weakening by halting NADW formation in the northern North Atlantic (e.g. Johnson and McClure, 1976; Rooth, 1982; Broecker et al., 1989; Berger, 1990; Alley, 2000; Broecker et al., 2010). Another hypothesis first introduced in the late 1980s is that the sulfur-rich Laacher See eruption (LSE) in Germany catalysed rapid climate shifts in the YD (van den Bogaard et al., 1989; Berger, 1990). However, perceived chronological mismatches (Hajdas et al., 1995; Brauer et al, 1999a, b) and the widespread acceptance of the meltwater pulse hypothesis at the time meant that the LSE hypothesis was quickly discarded (Baldini et al, 2018). Around a decade ago, Firestone et al. (2007) proposed the YD impact hypothesis (YDIH), which argues that at ~12.9 ka BP one or more bolides struck or exploded over the Laurentide Ice Sheet. Subsequent research supports a bolide impact by presenting more apparent evidence derived from terrestrial sediments, lake cores, and ice cores (e.g., Kennett et al. 2009; Kinzie et al. 2014; Moore et al., 2017; Wolbach et al. 2018a, b). However, the YDIH has drawn much criticism (e.g. Daulton et al., 2010; Pinter et al., 2011; Van Hoesel et al., 2014; Holliday et al., 2016, Sun et al., 2018). The LSE YD hypothesis regained traction in 2018 following: i) an updated Meerfelder Maar lake core tephrochronological framework by Lane et al. (2015), ii) a proposed explanation for delayed YD onset in Europe compared to Greenland Stadial 1 (GS-1) in the Greenland ice cores (Lane et al., 2013; Rach et al., 2014) and iii) the discovery of a potential LSE volcanogenic sulfur spike in the Greenland Ice Sheet Project 2 (GISP2) ice core (Baldini et al., 2018). The sulfur spike was indistinguishable from the start of GS-1 within the same ice core and correlated precisely with GS-1 onset in the NGRIP ice core as well (Baldini et al., 2018). Understanding the cause of the YD is crucial, particularly with modern climate in a state of change enhanced by anthropogenic forcing. Climate feedback is mostly unpredictable and a catastrophic event such as AMOC weakening, a large, sulfur-

rich eruption or large bolide impact(s) could “tip” the climate, as it may have ~12900 years ago.

Petaev et al. (2013) discovered a platinum (Pt) anomaly in the GISP2 ice core, which occurs almost synchronously with the YD onset. Despite Pt being depleted in the continental crust (Wedepohl, 1995), but enriched in chondritic meteorites (Anders & Grevesse, 1989), the GISP2 Pt spike is associated with a high Pt/Ir and Pt/Al ratio that is difficult to link to magma and meteorite geochemistry in the literature. Therefore, Petaev et al. (2013) attribute the Pt anomaly to an unusual highly differentiated, iridium-poor iron meteorite, but the precise nature of the possible impactor remains unknown. Petaev et al. (2013) do not consider volcanism as the source, despite the Pt anomaly’s age broadly coinciding with the LSE. The chronological mismatches discussed previously, combined with a lack of Pt and Ir analyses of the Laacher See tephra (LST), complicate establishing a definitive link. A number of terrestrial sediments across Europe and North America also contain Pt spikes at the YD boundary layer. For example, Wolbach et al. (2018a, b) identify 26 YD boundary sites with high Pt concentration, some with other potential impact-related proxies, and attribute the anomaly to a bolide impact that triggered catastrophic biomass burning and ultimately led to the YD climate shifts. Wolbach et al. (2018a, b) consider volcanism as the Pt anomaly’s origin, but ultimately disregard this because previous research (Firestone et al., 2007; Moore et al., 2017) detected no volcanic tephra in the North American terrestrial samples. Wolbach et al. (2018a, b) directly considered Laacher See as the Pt origin, but use of out-of-date age constraints for the LSE (that placed it ~200 years too early) and because one distal sample of LST suggested Pt is below detection limit (0.1 ppb), this concept was dismissed.

However, research shows that well-defined Pt concentration peaks correspond to recent volcanic eruptions. Platinum concentrations in Greenland ice cores, analysed alongside other typical “volcanic” elements, suggest that the Pt anomalies originated from the 1991 eruptions of nearby Hekla volcano (Iceland) ash fallout and potentially the more distal Mt Pinatubo (Philippines) (Gabrielli et al., 2008). Similarly, Soyol-Erdene et al. (2011) discovered Pt spikes in Antarctic snow linked to several 20th century volcanic eruptions, with the most prominent peak coinciding with the 1991 Cerro Hudson (Chile) eruption. A recent study of well-stratified North American terrestrial deposits contains characteristic Pt peaks relating to three late Holocene explosive eruptions: Laki, Iceland (CE 1783-1784),

Kuwae, Vanuatu (CE 1452-1453), and Eldgjá, Iceland (CE 934) (Tankersley et al., 2018). Considering evidence on Pt-rich volcanism in ice cores and terrestrial sediments, clear potential exists for a volcanic source of the Pt anomaly in the GISP2 ice core – the Laacher See eruption. The missing link is a detailed analysis of the LST for Pt and other elements studied by Petaev et al. (2013).

2. Background

2.1. The Last Deglaciation and the Younger Dryas

The peak of the Last Glacial Maximum (LGM) ~26.5 ka to ~20 ka years ago was characterised by vast ice sheets covering large areas of the Northern Hemisphere (NH) (Denton et al., 2010). The oscillating build-up of NH ice sheets to a maximum volume was followed by a short warming period influenced by orbitally induced NH (65°N) summer insolation increase (Alley & Clark, 1999; Denton et al., 2010). Seasonal insolation anomalies are controlled by orbital cycles of eccentricity, precession and obliquity (the 'Milankovitch' cycles), which occur on 100 ka, 41 ka and 23 ka cycles respectively and force natural climate change (Denton et al., 2010; Clark et al., 2012). The initial NH summer insolation increase induced the last deglaciation of the Late Quaternary period, and subsequent climate feedback triggered substantial reduction of ice volume from ~20 ka BP to ~7 ka BP (Clark et al., 2009; Denton et al., 2010). As the ice sheets melted and surged, sea-level rose by ~120m, global atmospheric CO_2 increased by ~100ppm and methane (CH_4) levels rose, further raising surface temperatures and propelling the climate into interglacial conditions (Denton et al., 2010; Clark et al., 2012). Within this period, several millennial-scale cold, dry periods (stadial) and warm, wet periods (interstadial) punctuated the climate. These mechanisms are characteristic of the Late Quaternary period, where a recurring pattern of ice sheet growth and decay tipped the climate from glacial to interglacial and vice versa (Denton et al., 2010).

2.1.1. Younger Dryas Climate in the Northern Hemisphere

More abrupt than the last deglaciation itself, although not a complete reversal to glacial conditions, a millennial-long period of cold, dry conditions known as the Younger Dryas stadial marked the end of the Pleistocene period. In comparison to the preceding warm period (the 'Bølling-Allerød' interstadial), climatic extremes in the YD were heightened around North Atlantic margins, resulting in colder summers and severely cold winters (Rasmussen et al., 2014; Lowe & Walker, 2014). Greenland ice cores best express NH climate at the time - the renewed cooling period is referred to as GS-1 in the Greenland ice cores (Rasmussen et al. 2006, 2014; Lowe & Walker, 2015). As such, in this report, when discussing the Greenland ice cores the terminology GS-1 is used, but in reference to the wider North Atlantic region for the cold period that started ~12.9 ka and terminated ~11.7 ka, the term

YD is used (Rasmussen et al., 2006, 2014; Carlson, 2013). GS-1 is marked by a shift in $\delta^{18}O$ isotopic values in Greeenland ice cores reflecting Arctic sea ice changes, and thus moisture availability and decreasing temperatures (Lowe & Walker, 2014; Sime et al., 2019). A review of wider YD paleoclimate records suggests ~5°C cooling in high latitudes and ~2°C in mid latitudes (Shakun & Carlson, 2010), and cooling was accompanied by increasing dust content and thus increased windiness (Mayewski et al., 1994), and decreasing Greenland Ice Sheet accumulation (Cuffey & Clow, 1997; Alley, 2000). Despite a rapid decrease in surface air temperatures, the YD is warmer than the previous stadial GS-2.1a around 17.5ka to 14.7ka (or in less archive-specific context, 'Heinrich Stadial 1'; HS1). This is expressed by NGRIP $\delta^{18}O$ (see Rasmussen et al., 2014), and recent research on nitrogen isotopes ($\delta^{15}N$) in three Greenland ice cores (North Greenland Eemian Ice Drilling; NEEM, GISP2 and NGRIP) combined with simulations inclusive of a coupled ocean-atmosphere climate model suggest the YD was 4.5 ± 2°C warmer than HS1 (Buizert et al., 2014). Furthermore, the Bølling-Allerød to YD transition is one of many interstadial-stadial transitions of the Last Glacial period (see Rasmussen et al., 2014) – the nature of the YD and its climatic conditions are not necessarily uncommon in the last glacial cycle.

2.1.2. Younger Dryas Climate in the Southern Hemisphere and Tropical Regions

The Southern Hemisphere (SH) exhibits warming over the NH YD period, reflected by increasing $\delta^{18}O$ and deuterium excess (δD) in Antarctic ice cores (EPICA Community Members, 2006), as opposed to cooling; this anticorrelation in temperature during millennial-scale climate change between the NH and SH is referred to as the bipolar see-saw (Carlson, 2013). SH mid to high latitude warming during this period was ~1°C – a much smaller amplitude than NH cooling (Shakun & Carlson, 2010). Increasing localised SH rainfall is shown by a speleothem isotopic time-series from northern Australia; higher summer monsoon rainfall corresponds with the YD and other Quaternary stadials, while decreased summer monsoon rainfall coincides with interstadials (Denniston et al 2013; Lowe & Walker, 2014). In tropical regions, temperature anomalies were less pronounced and average 0°C in both hemispheres (Shakun & Carlson, 2010). Temperature anomalies (>2°C) are focused around the North Atlantic region at deepwater formation sites with

associated sea ice feedback. Shakun and Carlson (2010) estimate a global mean cooling of ~0.6°C during the YD.

2.2. Causes and Mechanisms of the Younger Dryas

The precise cause of the rapid climate changes discussed above is poorly understood. Although it is widely accepted that suppression of NADW formation (Boyle & Keigwin, 1987; Denton et al., 2010) and weakening of the AMOC (Lane et al., 2013) coupled with sea ice growth may explain much of the YD climate change, the catalyst of this major oceanic reorganisation remains under debate (Broecker, 2006a, Broecker et al., 2010). The three hypotheses introduced in Chapter 1: i) a meltwater pulse, ii) bolide impact(s) and iii) the Laacher See eruption, are all plausible explanations as triggering events during a sensitive and unstable deglaciation climate feedback system, and as such warrant further discussion in this section.

2.2.1. The Meltwater Pulse Hypothesis

The most extensively studied YD trigger hypothesis is the meltwater pulse hypothesis: a North Atlantic meltwater injection on a sufficient scale and time period to promote AMOC weakening (or halting) by slowing NADW formation rate (Broecker et al., 1989; Lowe & Walker, 2014). The NADW is an enormous source of heat for the North Atlantic region's atmosphere, therefore, the shutdown caused North Atlantic atmospheric temperatures to decrease and promoted sea ice growth (Lowe & Walker, 2014).

The idea of pulsed meltwater input to explain deglaciation in YD Europe was discussed in the 1960s (e.g. Olausson, 1963; Mercer, 1969). Mercer (1969) suggested the YD was triggered by warm water addition to Arctic regions, causing abrupt Arctic ice shelf melting. Johnson and McClure (1976) argued that warm water introduction into Arctic region waters began earlier than proposed by Mercer (1969), and that Arctic ice would not have accumulated to such a degree because of polar region oceanic and atmospheric forcing. Instead, Johnson and McClure (1976) suggested that Great Lakes drainage rerouting from the Mississippi River to St. Lawrence Valley reflected glacial front retreat in the St Lawrence River area, subsequently increasing central northern Atlantic glacial meltwater input, reducing surface salinity and hence water density, and prompting pack ice growth. Further

research attributed the Great Lakes catastrophic drainage to a large glacial lake (Lake Agassiz) that formed along the southwestern front of the Laurentide Ice Sheet (LIS) during ice sheet decay (Rooth, 1982; Broecker et al., 1989). Prior to LIS retreat, Lake Agassiz meltwater overspilled to the Gulf of Mexico via the Mississippi River (Broecker et al., 1989). According to this hypothesis, LIS retreat opened channels leading to the Lake Superior basin, driving Lake Agassiz water eastward to the northern Atlantic, through the Great Lakes and St Lawrence Valley (Broecker et al., 1989). This is supported by oxygen isotope and radiocarbon measurements on planktonic foraminifera in marine cores, revealing a notable meltwater flow decrease from the Mississippi River outlet (Kennett & Shackleton, 1975; Broecker et al., 1989). Approximately 30,000 m^3s^{-1} water was rerouted, causing Lake Agassiz water level to drop ≥40m (known as the Moorhead phase) – a hypothesis supported by exposed lake bottom material radiocarbon dated to the YD (Broecker et al., 1989; Teller & Leverington, 2004). Alternatively, the meltwater may have followed another, more northern route to the North Atlantic – the Mackenzie River – as supported by geological and modelling evidence (Condron and Winsor, 2012; Murton et al., 2010).

Although rerouting of meltwater was an attractive explanation for NADW slowdown, decreasing meltwater input from other LIS fronts and the Fennoscandian Ice Sheet (FIS) may have offset the YD meltwater pulse through St Lawrence valley (Broecker et al., 1989; Muschitiello et al., 2015). Muschitiello et al. (2015) dated a FIS meltwater pulse ending at 12.880 ka BP, therefore indicating YD cooling and related positive feedback may have reversed insolation-controlled FIS melting. Secondly, a similar meltwater diversion dated to ~10,000 radiocarbon yr BP unsuccessfully fabricated another YD equivalent cold snap (Broecker et al., 1989). Despite these issues, the meltwater pulse hypothesis remained prominent in YD research (e.g. Berger, 1990; Alley, 2000), and the compatibility of estimated meltwater volume outflow to the North Atlantic with model estimates required to affect ocean circulation supported this (Teller & Leverington, 2004). Lowell et al. (2005) challenged the accuracy of radiocarbon measurements of terrestrial macrofossils within Lake Agassiz lake sediments. Later radiocarbon age testing confirmed that Ojata Beach sediments, representing the low-water Moorhead phase, were younger than previously assumed, and the deposits reflect YD termination lake level transgression as opposed to YD onset lake level regression (Fisher et al., 2008). Furthermore, no geomorphic evidence was discovered along

the Gulf of St Lawrence or a northern route to the North Atlantic to suggest a significant meltwater pulse around the YD onset (Lowell et al., 2005; Broecker et al., 2010; Petaev et al., 2013). Therefore, a later deglaciation was suggested, thus questioning the timing of Lake Agassiz eastern outlet's opening and assuming that catastrophic drainage occurred as a flood because the eastern outlet remained blocked by the LIS (Lowell et al., 2005; Teller et al., 2005). However, significant AMOC strength reduction and thus North Atlantic cooling on a thousand-year scale is unlikely to arise from floodwaters (Clark et al., 2001; Meissner and Clark, 2006), and recent surface exposure ages indicate an ice-free eastern outlet (Leydet et al., 2018). Strong evidence from Icelandic sediments implies that stadial cooling commenced before iceberg discharges, therefore ruling out iceberg-sourced freshwater input as a YD trigger (Barker et al., 2015). There is evidence of a final, catastrophic drainage of Lake Agassiz through the Hudson Strait ~8200 years ago, around the onset of the North Atlantic climate anomaly, perhaps even more sudden than YD onset (Broecker et al., 2010). For this reason, Broecker et al. (2010) argued that "the YD was an integral and inevitable part of the deglaciation sequence of events", as opposed to a sudden, unexpected climatic event.

2.2.1.1. Climate Effects of a Meltwater Pulse

Whether sudden and unexpected or a natural, predestined climatic event, a large meltwater pulse directed to the North Atlantic is likely to have suppressed NADW formation to some degree. Freshwater input from glaciers reduces sea surface salinity, preventing the exchange of cold deep waters for warm surface waters (Olausson, 1965), weakening (or completely disrupting) AMOC by reducing cross-equatorial heat import and ultimately impacting the "global heat loop" (Berger, 1990). Freshwater input also encourages formation of extensive sea ice cover, blocking the release of ocean heat and increasing albedo, eventually causing a hemispherical drop in NH atmospheric temperatures (Broecker et al., 2010). Some anomalies include the YD European summer temperatures, which remained fairly warm, possibly offset by cold westerly wind obstruction over Fennsocandia (Schenk et al., 2018). Further climate feedbacks include sea ice growth directing westerlies to a southern path (e.g. Brauer et al., 2008) and southward displacement of the Intertropical Convergence Zone (ITCZ), which causes weakening of the East Asian and Indian Monsoons and eventually Antarctic warming - all characteristic of the YD (Lowe & Walker, 2014; Baldini et al., 2018).

2.2.2. The Younger Dryas Impact Hypothesis

Firestone et al. (2007) hypothesised that rapid YD cooling, megafaunal extinction, human cultural changes, and a prompt post-Clovis culture decrease of some human populations was triggered by “multiple extra terrestrial (ET) airbursts and surface impacts” over the LIS and its related catastrophic biomass burning. Some evidence interpreted as impact markers includes: i) magnetic microspherules, ii) magnetic grains, iii) iridium (up to 117ppb) and nickel, iv) soot and polycyclic aromatic hydrocarbons, v) carbon spherules, vi) Fullerenes and ET helium (^{3}He) and vii) glass-like carbon (Firestone et al., 2007). Concentration peaks of the markers were discovered within a thin sedimentary layer at 10 sites – nine in North America and one in Belgium, and extending across 15 Carolina Bays – underlying a carbon-rich black layer dated to 12.9 ka that was previously identified in sediments at >50 sites across North America (Haynes, 2005; Firestone et al., 2007). A lack of traditional impact markers in the terrestrial record such as shocked minerals, breccias, tektites and craters cast doubt upon the YDIH (Kennett et al., 2009), but lead to the suggestion of impact by an already fragmented ET object, similar to the 1908 Tunguska (Central Siberia) explosion where a stony asteroid exploded at ~10km altitude, releasing 10-20 Mt (high explosive equivalent) of energy (Chyba et al., 1993; Kennett et al., 2009). Secondly, YDIH advocates argued an impact to the LIS’ surface would preserve little evidence (Pinter et al., 2011).

Kennett et al. (2009) discovered peaks of nanometer-sized impact diamonds (nanodiamonds), consistent with the n-diamond polymorphs found in meteorites (lonsdaleite), in Younger Dryas Boundary (YDB) sediments dated to 12.9 ka BP across North America. Formation of nanodiamonds may occur through two processes: i) impact-induced shock-modification of graphite or ii) if found with silicon carbide, accretion of diamond on substrates containing silicon through an interfacial layer of silicon carbide, in a mechanism pertaining to chemical vapour deposition (Hough et al., 1997). Nanodiamonds peaked at ~ >1 billion diamonds per cm^3 in sediments at Lake Hind, Canada, Bull Creek, Oklahoma and Murray Springs, California (Kennett et al., 2009). Furthermore, nanodiamonds are observed in YDB sediments at the latter two sites outside of carbon spherules, with concentrations up to ~200 ppb (Kennett et al., 2009).

In addition to Ir analysis, Firestone et al. (2010) assessed major and trace elements of a number of impact markers at the YDB, suggesting they were unlike most known ET and terrestrial rocks, but somewhat aligned with lunar KREEP – a

potassium-rare earth element (REE)-phosphorous-rich geochemical component of some lunar rocks observed in meteorite SAU-169, which potentially struck Oman within the YD (Gnos et al., 2004; Firestone et al., 2010). The geographical distribution and composition of magnetic grains, and high water content in the ejecta indicates an airburst over the LIS (Firestone et al., 2010). Four “holes” in the Great Lakes region are proposed impact sites (Firestone et al., 2010), although these are not dated (Pinter et al., 2011).

Subsequent research highlighted problems with the YDIH, for example, Daulton et al. (2010) found no evidence of nanodiamonds at Murray Springs (Arizona, USA) and proposed they were misidentified, instead suggesting they were graphene/graphane-oxide aggregates at the YDB layer, which are not characteristic “impact markers”. Furthermore, Pinter at al. (2011) produced a critical analysis of the impact markers proposed by YDIH advocates, an example of which is the iridium peaks identified by Firestone et al. (2007). The source of Ir “peaks” were lab separates of microspherules and magnetic grains, not bulk sediment, and therefore Ir is potentially concentrated by a factor of 59 to >3000 (Pinter et al., 2011). Concentrations in bulk sediment were below detection limit at six out of 10 sites, with a maximum of 3.8 ppb at the remaining four sites and thus Firestone et al. (2007) hypothesised an Ir-poor impactor. Paquay et al. (2009) reported some Platinum Group Element (PGEs; ruthenium, rhodium, palladium, osmium, iridium, platinum) concentrations at the YDB (including some of the Firestone et al., 2007 sites), however they did not find elevated Ir concentrations and attributed small osmium (Os) and iridium peaks to natural authigenic enrichment.

Later research by Petaev et al. (2013) found a Pt spike in the GISP2 ice core, with a lack of Ir, leading the authors to suggest a Pt rich, Ir-poor bolide in agreement with Firestone et al. (2007). A “preliminary impact model” on the nature and mechanism of impact using YDB evidence was created (Wittke et al., 2013), and Wu et al. (2013) suggested an impact site on the LIS southern margin, specifically the 1.5 Ga Quebeca terrain, northeastern North America. Recent research focused on Pt enrichment in YDB sediments – Moore et al. (2017) identified Pt in bulk terrestrial sediments across 11 sites in North America. Recently, Wolbach et al. (2018a, b) report elevated Pt concentrations at 26 YDB sites, with a suggested cosmic origin, and evidence of extensive impact-induced global wildfires, including peaks in combustion aerosols ammomium, nitrate, oxalate, acetate and formate present in ice cores, and charcoal and soot in marine cores, lake cores and

terrestrial sequences. The fragments of a “disintegrating ≥100km diameter comet” are suggested as the biomass burning trigger leading to an “impact winter” (Wolbach et al., 2018a, b). The impact and biomass burning is recently supported by further evidence in Patagonia, southern Chile (Pino et al., 2019). Some prominent issues with the YDIH include: i) a lack of chronological control between YDB sites (Meltzer et al., 2014), ii) problems with impact marker reproducibility (Holliday et al., 2016; Sun et al., 2018) and iii) misunderstanding of airburst physics in regards to the nature of impact, for example, iron meteorites explode too low (or not at all) to cause atmospheric distribution of the object following widespread air shocks (Chyba et al., 1993; Boslough et al., 2013). However, a recent discovery of a large impact crater beneath Hiawatha Glacier in NW Greenland interpreted as the mark of a >1km diameter iron meteorite has brought recent attention to the YDIH, although the age of the impact crater is poorly constrained (Kjaer et al., 2018).

2.2.2.1. Climate Effects of a Meteorite Impact

Nonetheless, if an impactor did strike the Earth as proposed by Firestone et al. (2007), there is potential for resulting climate effects (Table 2.1). The following possibly occurred after the hypothesised YD impact: i) ozone depletion caused by nitrogen compounds (NO_x) impacting wind patterns and atmospheric circulation, and with time, allowing increased harmful UV radiation to reach the surface (although a sustained sulfate aerosol haze could reverse this) (Toon et al., 1997), ii) widespread wildfires, burning 9% of global biomass (Wolbach et al., 2018a, b) releasing soot, sulfates, dust and NO_x into the atmosphere which causes climate cooling by scattering incoming solar radiation and secondary impacts such as photosynthesis cessation and increasing toxicity in surface waters and soils (resulting in poisoning of plant and animal life), iii) introduction of vast amounts of water vapour and ice into the atmosphere, increasing cloudiness and forming noctilucent clouds, reducing solar irradiance (particularly at high latitudes) and ultimately causing climate cooling and iv) impact-induced destabilisation of the LIS, triggering a meltwater pulse and causing climatic effects discussed in Section 2.2.1 (Toon et al., 1997; Firestone et al., 2007). Acting independently these factors would influence climate on a year-scale, but to cause millennial-scale climate perturbation observed in the YD, initial impacts require amplification by climate-feedback mechanisms. For example, persistent noctilucent cloud cover reduces solar insolation in high latitudes, increases snow accumulation, which increases albedo

and reduces heat exchange between the surface and the atmosphere, thus causing atmospheric cooling (Toon et al., 1997; Firestone et al., 2007).

Table 2.1: Potential Environmental Perturbations of a Meteorite Impact (adapted from Toon et al., 1997).

Agent	**Environmental effect**	**Timescale**	**Geographic scale**
Injection of Nitrogen compounds (NOx) into the atmosphere	Ozone depletion Acid rain Cooling	Years Months Years	Global Regional Global
Biomass burning – injection of soot and other pyrotoxins into the atmosphere	Acid rain Soot cooling	Months Months	Global Global
Dust loading	Cooling Cessation of photosynthesis	Years Months	Global Global
Toxic chemicals – heavy metals into soils and watercourses	Increased toxicity	Years	Global
Sulfur dioxide (SO_2) injection into the atmosphere and sulfur into oceans	Cooling Acid rain Ocean acidification	Years Years	Global Global
CO2 injection into the atmosphere	Warming	Decades	Global
Water vapour/ice particles into the atmosphere	Warming or cooling	Months	Global
Impact with Earth's surface	High winds/shock wave	Instantaneous	Regional
Earthquake	Ground shaking	Instantaneous	Regional
Tsunami	Flooding	Instantaneous	Regional

2.2.3. The Laacher See Hypothesis

2.2.3.1. The Laacher See Eruption

The Laacher See volcano is located in western Germany (Fig. 2.1) and is part of the East Eifel volcanic field which is fed by the Central European intraplate alkaline province (Reide, 2016). The East Eifel volcanic field became active around 0.7 myr ago following uplift caused by seismotectonic activity in the West European Rift Zone (Baales et al., 2002). The VEI 6 eruption, similar in magnitude to the 1991 Mt Pinatubo eruption, produced approximately 6.3 km^3 of sulfate-rich evolved phonolite and sulfide-rich mafic phonolite magma and 20 km^3 pumice and ash, from a compositionally zoned magma chamber, that covered >230, 000 km^2 of Europe (Bogaard & Schmincke, 1985; Harms & Schmincke, 2000; Baales et al., 2002; Baldini et al., 2018). A lake was left in its wake (Fig. 2.1) through which intraplate mantle plume activity, recently modelled by seismic tomography methods (Zhu et al., 2012), is reflected by degassing of CO_2 promoting 'bubbling' in certain areas of the lake. Underlying country rock comprises Devonian slate and greywacke, overlain by tertiary basalts and quaternary phonolites, leucitites and trachytes (Schmitt et al., 2010).

The eruption timing is well constrained, dated at ~12.880±0.040 ka BP through varve-counting methods of regional lake deposits such as the Meerfelder Maar (MFM) (e.g. Brauer et al., 1999a; Lane et al., 2015). Laacher See erupted in alternating Plinian and phreatomagmatic phases, emplacing widespread fallout deposits and medial base surge and pyroclastic flow deposits, and producing three major compositionally different tephra sequences based upon contrasts in eruptive and depositional processes, lithology and geochemistry: i) the Lower Laacher See Tephra (LLST); ii) the Middle Laacher See Tephra (MLST) and iii) the Upper Laacher See tephra (ULST) (Bogaard & Schmincke, 1985). The eruption comprised the following main phases (Fig. 2.2): i) initial phreatic-phreatomagmatic blast, ii) first Plinian phase, iii) major hiatus with conduit collapse and crater shift (the 'big bang'), iv) transitional mud rain phase and column collapse, v) further column collapse and ash fountaining, vi) pyroclastic Plinian phase (max eruption rate), vii) pyroclastic-phreatomagmatic phase, viii) final phreatomagmatic phase and chamber wall subsidence and ix) waning and post-eruptive erosional phases (Schmincke et al. 1999; Schmincke, 2004; Park & Schmincke, 2019 in press).

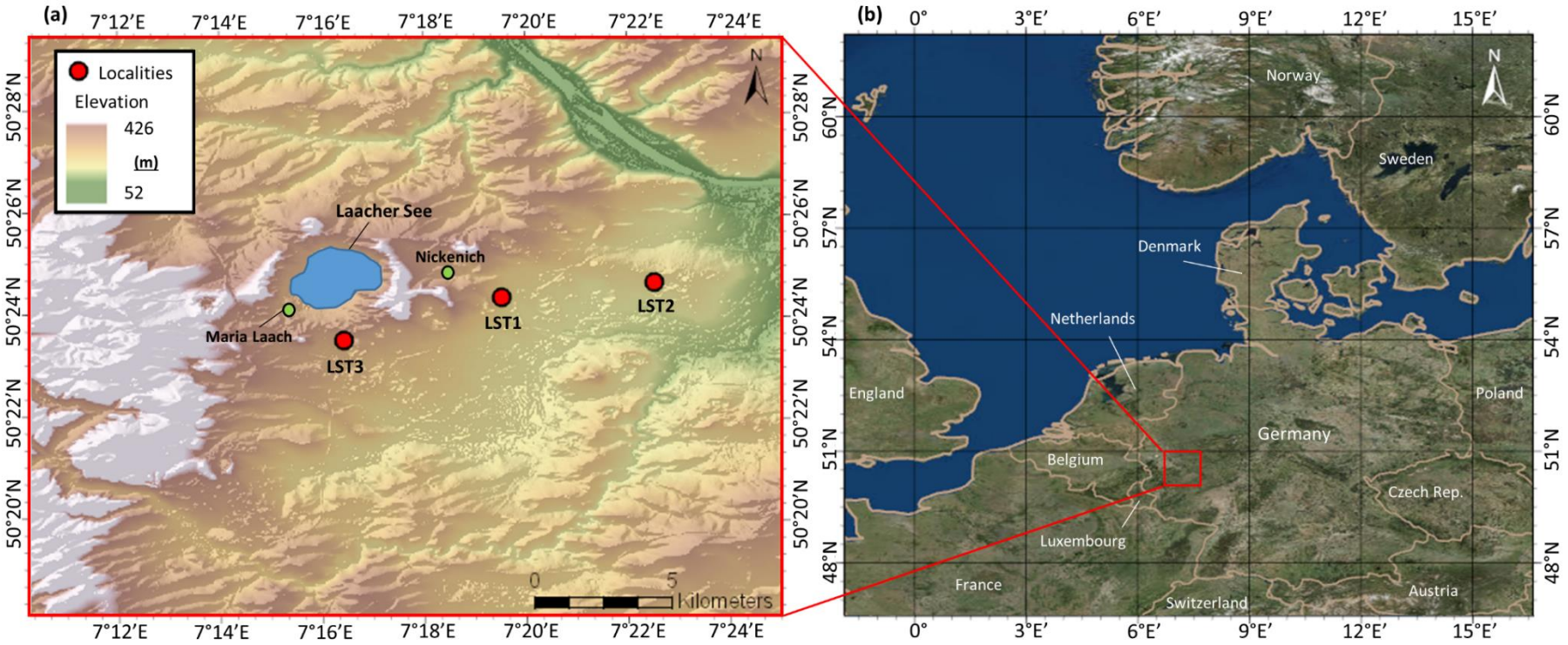

Figure 2.1: (a) Digital Elevation Model (DEM) of the local area around Laacher See with localities discussed in this report and (b) wider location of the field area within NW Europe (red box indicates the local area of the Laacher See). DEM is modified by "Sonny", available from http://data.opendataportal.at/dataset/dtm-Germany; satellite imagery sources: (a) Esri, HERE, Garmin, Intermap, increment P Corp, GEBCO, USGS, FAO, NPS, NRCAN, GeoBase, IGN, KadasterNL, Ordnance Survey, Esri japan, Esri China (Hong Kong), © OpenStreetMap contributors and the GIS User Community; (b) Esri, DigitalGlobe, GeoEye, Earthstar Geographics, CNES/Airbus DS, USDA, USGS, AeroGRID, IGN and the GIS User Community.

The LSE was unusually sulfur-rich, and recent estimates suggest ~83 Mt sulfur dioxide (SO_2) was released into the atmosphere (Baldini et al., 2018). This value is ~4x the SO_2 released by the 1991 Mt Pinatubo eruption (~20 Mt) and perhaps higher than the 1815 Tambora eruption (~70 Mt) (Shinohara, 2008). The LSE's sulfur-rich nature in comparison to its magnitude meant that, despite having the same magnitude as the 1991 Mt Pinatubo eruption, amplified climate cooling was entirely possible because SO_2 release controls cooling effects more so than magnitude (Rampino and Self, 1982; Robock and Mao, 1995). The nature, timing and location of the LSE would have amplified its climate forcing potential, and thus its likelihood as a YD cooling catalyst.

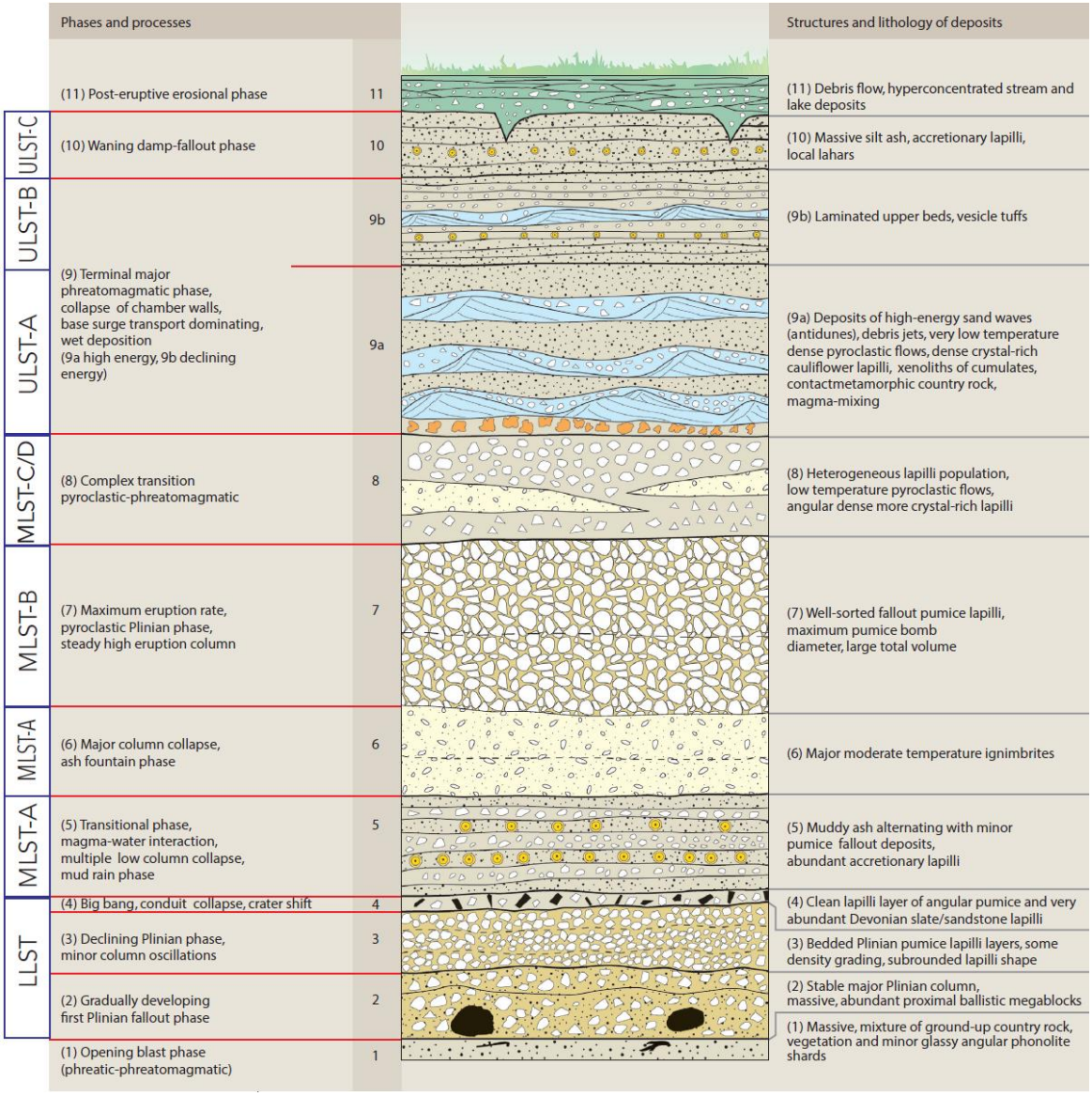

Figure 2.2: Schematic stratigraphic log of the Laacher See tephra with eruption phases (Park & Schmincke, 2019 in press).

2.2.3.2. A Review of the Laacher See Hypothesis

The link between the LSE and the YD was first introduced in the late 1980s, where it was suggested the LSE potentially caused at least 0.5°C of short-term surface cooling, and thus may have dramatically affected NH climate (van de Bogaard et al., 1989). At the time, the ^{14}C (radiocarbon) age of the LSE was estimated ~11,000 BP (van den Bogaard and Schmincke, 1985) – coincident with decreased tree ring thickness of fossils firs (van den Bogaard et al., 1989), implying shorter growing seasons and a cooler, drier climate (Fritts, 1966). Van den Bogaard et al. (1989) acknowledged the LSE's sulfur-rich nature, and the potential climate impact from a sulfur-rich aerosol injected into the atmosphere. The climatic impact of sulfur-rich volcanism was discussed in the early 1980s using the historical eruptions of Mt Agung, Indonesia (1963) and El Chichón, Mexico (1982) as examples of small-volume eruptions producing significant stratospheric sulfuric acid aerosol clouds that caused atmospheric effects (Rampino and Self, 1982). However, quantification of the climate effects of volcanic eruptions did not occur in detail until after the 1991 Mt Pinatubo eruption (Baldini et al., 2018). Later research on the YD suggested a volcanic trigger, particularly in unstable deglaciation conditions, could interfere with the complex climate feedback system and acknowledged the LSE occurred close to YD onset (Berger, 1990). Despite this, the hypothesis was dismissed considering the meltwater pulse hypothesis' (Section 2.2.1) wide acceptance. Furthermore, subsequent dating of the LSE in varved lake sediments (e.g. MFM, Soppensee, Holzmaar and Schalkenmehrener Maar) implied the eruption occurred ~200 years before evidence of the YD transition in Europe in the same lake sediments (Lotter et al., 1992, 1995; Hajdas et al., 1995; Brauer et al., 1999a; 1999b) and therefore could not have triggered the YD (Schmincke et al., 1999). Additionally, estimates of SO_2 injection into the atmosphere from the early phase LSE were estimated at 15 ± 5 Mt using Mt Pinatubo as an analogy (Graf and Timmreck, 2001), which is far from recent estimates of ~83 Mt (Baldini et al., 2018). The suggested climate impact was restricted to "midlatitude continental winter warming" with the chronological mismatches making it difficult to suggest the LSE triggered the YD (Graf and Timmreck, 2001).

An updated chronological framework of the MFM was produced using the discovery of the Vedde Ash in the varved lake sediments and subsequent correlation with Greenland ice core chronology, which also contains the Vedde Ash (Lane et al., 2013; 2015). Furthermore, a decrease in hydrogen isotope values (δD)

of both aquatic and terrestrial lipid biomarkers at 12.85 ka BP in the MFM (Rach et al., 2014) implied cooling synchronous with abrupt Greenland cooling shown in the ice cores at 12.846 ka BP (Rasmussen et al., 2014; Fig. 2.3). Rach et al. (2014) also found another reduction of δD ~170 years after the initial drop, but mostly in aquatic lipids and less so in terrestrial lipids. Moisture pathway alterations over time can affect δD at mid- to high-latitudes (Gat, 1996; Rach et al. 2014), and therefore a δD decrease may suggest atmospheric circulation reorganisation (Rach et al., 2014). A suggested cause is a time-lag between initial YD cooling and hydrological and environmental changes in western Europe caused by sea-ice expansion which forced the westerlies southward (Lane et al., 2013; Rach et al., 2014; Baldini et al., 2018). Therefore, recent research has shown the LSE as synchronous with GS-1 cooling, and biomarkers show immediate changes following the eruption in western Europe (Fig 2.3).

Further evidence favouring the LSE hypothesis are volcanic 'signatures' found in European sediments at the Bølling-Allerød to Younger Dryas transition ~12.9 ka BP, with the LSE as a suggested source (Andronikov et al., 2014; 2015; 2016). More recently, a large volcanogenic sulfate peak in the GISP2 ice core was attributed to the LSE because the timing (12.867 ka BP) was synchronous with the LSE in MFM sediments (Baldini et al., 2018). The spike is coetaneous with a drop in $\delta^{18}O$ values in the NGRIP ice core, marking GS-1 onset. However, Baldini et al. (2018) acknowledge a large sulfate spike is not indicative of the source and could result from a proximal eruption, possibly from Iceland (Coulter et al., 2012). Furthermore, particular focus is given the relationship between Pt and the YD because of the YDIH (Petaev et al., 2013; Moore et al., 2017; Tankersley et al., 2018; Wolbach et al., 2018a, 2018b), as discussed in Section 2.2.2.1, but the LSE was briefly considered as a source of Pt (Moore et al., 2017). Perceived discrepancies with the YD chronology and a lack of Pt data in the LST meant the LSE hypothesis is often dismissed as a plausible explanation for the YD trigger (Moore et al., 2017; Wolbach et al., 2018a).

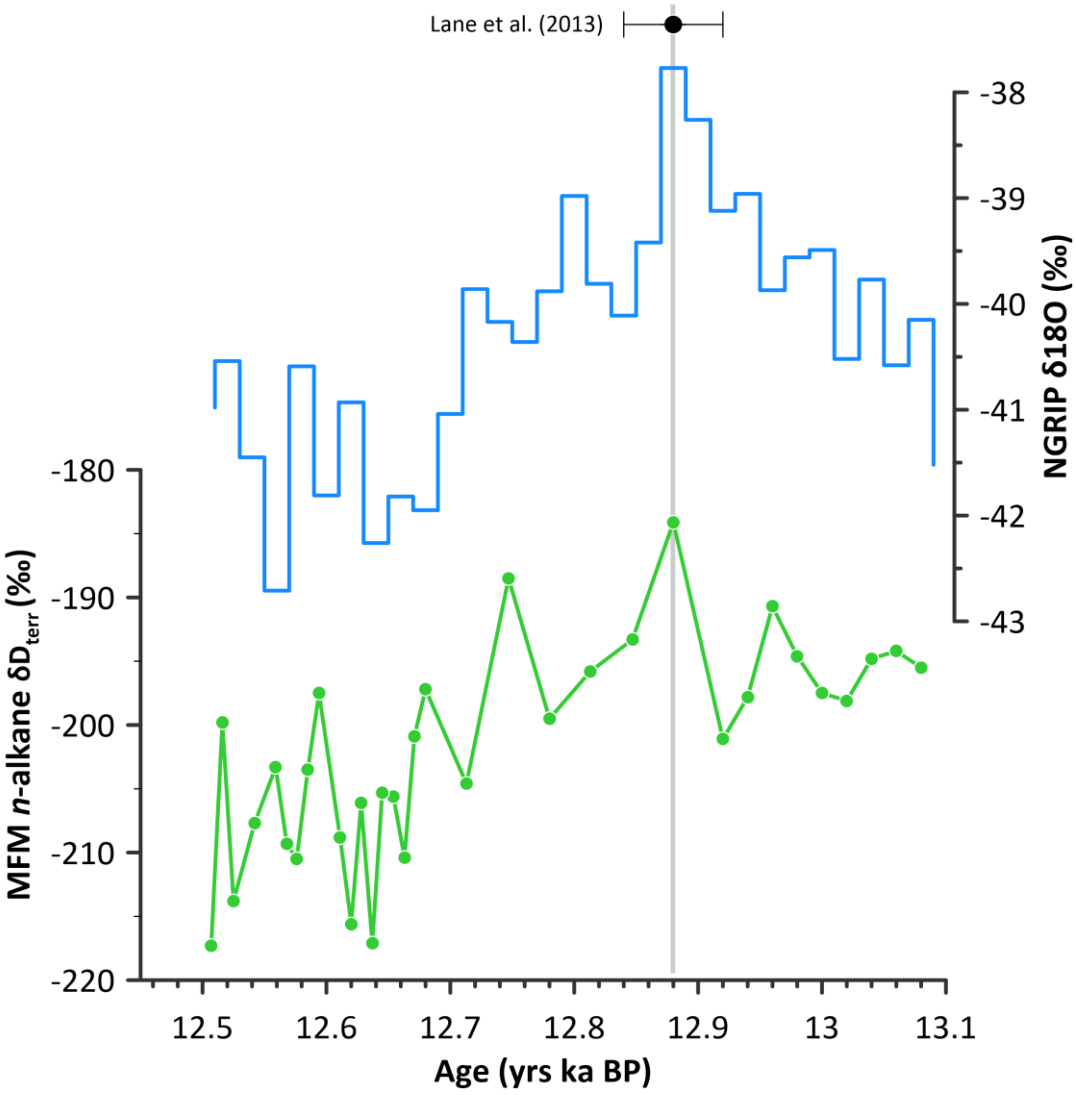

Figure 2.3: Comparison of δD values (‰) in MFM lake sediments and $\delta^{18}O$ values (‰) in the NGRIP ice core or the period ~12.5 ka BP to 13.1 ka BP. The black dot indicates the timing of the LSE dated in MFM lake sediments, and the grey line shows the correlation between the LSE, δD and $\delta^{18}O$ at 12.88 ka BP. Values for $\delta^{18}O$ are from Seierstad et al. (2014) and references therein, δD values are from Rach et al. (2014) and the LSE date is from Lane et al. (2013).

2.2.3.3. Climate Impact of the LSE

Considering the explosive and sulfur-rich nature of the LSE, considerable amounts of sulfur-rich volatiles were likely delivered to the stratosphere in the form of sulfur dioxide (SO_2) or hydrogen sulfide (H_2S), causing atmospheric effects (Rampino and Self, 1984). A sulfuric acid vapour (H_2SO_4) of low volatility is formed when the sulfur-rich gases are oxidised, which then reacts with water and condenses to create a sulfate aerosol haze (Robock & Mao, 1995; Robock, 2000).

The volcanic aerosols are carried around the globe in a few weeks by lower stratospheric zonal winds then pushed equatorward or poleward by atmospheric circulation, where they remain in the atmosphere for approximately 1-3 years, although this varies between eruptions depending on a number of factors (Robock & Mao, 1995; Robock, 2000; Baldini et al., 2018). Volcanic aerosols cause direct implications on the Earth's radiative budget by backscattering incoming solar radiation to space (Robock and Mao, 1995), and indirect effects on atmospheric circulation which influence the Earth's surface temperature (Robock, 2000). These short-term effects are well studied for the tropical 1991 Pinatubo and 1982 El Chichón eruptions (Rampino and Self, 1984; Robock, 2000, 2002), and it is commonly suggested that tropical eruptions have a greater climatic impact (Robock, 2000) owing to greater global advection of aerosols and a longer stratospheric residence time (Schneider et al., 2009). However, recent research suggests confinement of volcanogenic aerosol to one hemisphere (in this case, the NH) results in radiative impact amplification, and NH extratropical eruptions cause up to 80% more time-integrated radiative forcing than their tropical counterparts (Toohey et al., 2019).

In addition to sulfate aerosol, eruptions may release volcanogenic halogens that deplete stratospheric ozone (Cadoux et al., 2014). Ozone loss may result in surface cooling by negative radiative forcing and amplification of volcanic sulfate aerosol radiative effects, because ozone absorbs thermal infrared and solar ultraviolet radiation (Cadoux et al., 2014; Baldini et al., 2018).

Long-term climate effects are less recognised, owing to the complex interaction between short-lived volcanic aerosols and the ocean-atmospheric system. A well-studied example is the anomalously cold summers of Little Ice Age (LIA; ~1400 – 1700 AD) that were possibly triggered by four NH explosive sulfur-rich volcanic eruptions with global sulfate loading >60 Mt (equivalent to ~40 Mt SO_2) over a period of 50 years (Miller et al., 2012). The repeated explosive volcanism occurred during low summer insolation across the NH, particularly in the Arctic where solar insolation decrease is largest, leading to climate change amplification by strong positive feedbacks (Serreze and Francis, 2006; Miller et al., 2012). Reduction of solar radiation reaching the Earth's NH caused by the volcanic aerosol leads to cooler sea surface temperatures (SSTs), which allows for Arctic sea ice expansion (Miller et al., 2012). An extension of sea ice areal extent results in higher surface albedo and less insolation absorption, reducing heat flux between the

ocean-atmosphere system and thus causing lower surface air temperatures and sea level pressure (SLP) anomalies, eliciting further cooling and more sea-ice growth (Broecker, 2006b; Serreze and Francis, 2006; Lehner et al., 2013). As sea ice extends southward into warmer waters, it melts and causes a surface temperature and salinity decrease, thereby increasing ocean stratification and weakening oceanic circulation – a feedback mechanism demonstrated by modelling of the Barents Sea's role in LIA cooling (Lehner et al., 2013). This also mimics the previously discussed NADW shutdown that is significant in YD cooling, and there is evidence for sea-ice growth following GS-1 (Broecker, 2006b; Baldini et al., 2015b). A NADW shutdown would cause AMOC weakening (McManus et al., 2004) in the same way as a meltwater pulse (Section 2.2.1). Warm water delivery to the North Atlantic is impacted by AMOC weakening, as the AMOC comprises thermohaline and wind-driven elements (Baldini et al., 2018).

Asymmetric volcanogenic sulfate loading may also induce atmospheric circulation effects, for example, the forcing of Intertropical Convergence Zone (ITCZ) migration away from the eruption's hemispheric origin which causes Asian monsoon deterioration, Hadley circulation cell changes and a cascade of climate impacts globally (Chiang et al., 2014). Southward ITCZ migration may also further amplify NH atmospheric circulation alteration, by extending the NH polar cell and forcing the NH polar front towards the SH, leading to southward extension of sea ice and thus initiating further cooling and AMOC weakening (Baldini et al., 2015a, 2018). A combination of radiative forcing, AMOC weakening and atmospheric circulation perturbation is consistent with simulations of YD cooling (Renssen et al., 2015).

At the time of YD onset, the fragility of the deglacial climate likely contributed to amplification of initial volcanic eruption-induced climate perturbations (Rampino and Self, 1982; Zielinski et al., 1996). Ice sheets of intermediate volume appear to respond more readily to environmental perturbations; Baldini et al. (2018) assessed 55 stadial initiations against ice volume (drawn from Red Sea sea level), finding that most cooling episodes occurred across 40% of sea level range, at a sea level of ~68m below modern sea level. Zhang et al. (2014, 2017) made similar observations, however they highlight the complexity of the ocean-atmosphere system, namely atmospheric CO_2 and the influence of ice volume on AMOC stability (Zhang et al., 2017; Baldini et al., 2018).

Considering the timing, magnitude and sulfur dioxide release from the LSE, it is likely the eruption caused long-term climatic effects. Baldini et al. (2018) propose

that, during intermediate ice volume conditions, a release of ~83 Mt SO_2 into the atmosphere created a sulfate aerosol-veil that was advected around the globe and caused preferential NH cooling, offsetting hemispheric temperature balance. Immediate cooling caused by volcanogenic aerosol could have triggered long-term positive feedback within the climate system, promoting sea-ice growth and impacting AMOC, whilst forcing NH mid-latitude westerlies and the ITCZ southward (forcing further cooling in the NH), prompting Hadley circulation cell changes and causing SH warming (Rampino & Self, 1984; Broecker, 2006b; Serreze and Francis, 2006; Miller et al., 2012; Lehner et al., 2013; Chiang et al., 2014; Baldini et al., 2015a; 2018). The LSE was the "only known sulfur-rich, high-latitude eruption coinciding with the most sensitive ice volume conditions during the last deglaciation" (Baldini et al., 2018 pg 11), and therefore the most likely source of the sulfate spike at 12.867 ka BP. However, smaller, local Icelandic eruptions, that are less climatologically significant, preferentially contribute sulfate to the Greenland Ice Sheet, and are therefore a potential source of sulfate peaks in the Greenland ice cores and so further research is required to distinguish between distal and local sources (Baldini et al., 2018).

2.2.4. Summary

The three main hypotheses of the YD trigger have been discussed in previous sections, including (i) the meltwater pulse (Section 2.2.1), (ii) the YDIH (Section 2.2.2) and (iii) the Laacher See eruption (Section 2.2.3). Some other hypotheses include an abrupt, significant reduction in solar irradiance as a trigger for YD cooling, perturbing NADW through precipitation increase and iceberg release (Renssen et al., 2000) and possibly through wind shifts associated with ice sheets and the cryosphere-atmosphere interaction (Wunsch, 2006; Renssen et al., 2015).

Recent YD research has focused on Pt because of the YDIH. As previously discussed, Petaev et al. (2013) found a Pt spike of ~82 ppt in the GISP2 ice core, occurring almost synchronously with GS-1 onset (characterised by a shift in $\delta^{18}O$), with an unusually high Pt/Ir and Pt/Al ratio that they attribute to numerous injections of Pt-rich dust as result of an iridium-poor iron meteorite impact. Platinum, Ir, and the other PGEs are highly depleted in the Earth's upper crust (Wedepohl, 1995) and therefore their presence in sedimentary sequences, ice cores, lake cores, and other palaeoclimate archives indicates another source. PGE enrichment may occur from the following sources: (i) extraterrestrial (meteorites, asteroids, comets or cosmic

dust), (ii) volcanoes (aerosols, ashes, exhalative hydrothermal processes, mafic and ultramafic rocks and associated ore deposits), (iii) precipitation from seawater (particularly in anoxic conditions), (iv) biological processes (microbial enhancement and remobilisation of PGEs), and (v) post-depositional processes (Sawlowicz, 1993).

Platinum concentrations in the GISP2 ice core rise over 14 years to the peak, before declining over seven years (Petaev et al., 2013), and Wolbach et al. (2018a) propose that multiple injections are due to (i) pre-impact fragmentation of the iron meteorite in deep space, (ii) ejection of impact debris into the Earth's atmosphere post-impact and re-entry away from the initial impact site or (iii) post-impact ejection of debris through the Earth's atmosphere to create a debris ring around the planet (Boslough, 2001; Napier et al., 2015). Wolbach et al. (2018a) propose that these mechanisms could cause episodic biomass burning and thus contribute to Pt influx over time. Elevated Pt is found in YDB sediments in numerous studies (e.g. Paquay et al., 2009; Andronikov et al., 2014, 2015, 2016; Mahaney et al., 2016; Moore et al., 2017; Wolbach et al., 2018; Pino et al., 2019) and most infer a meteorite impact as the source.

However, in the same YDB lake sediments in NW Russia, Andronikov et al. (2014) report enrichments in both "meteoritic" elements and "volcanic" elements alongside Pt peaks – the latter which they attribute to the LSE. Similar relationships are found in Lithuanian lake sediments (Andronikov et al., 2015), the Netherlands and Belgium (Andronikov et al., 2016). Furthermore, Pt spikes in Holocene Antarctic ice are attributed to historic volcanic eruptions (Gabrielli et al., 2008; Soyol-Erdene et al., 2011), even in the presence of anthropogenic catalytic convertor emissions that may contaminate recent ice (Rauch and Morrison, 2008). Elevated Pt values related to the Holocene eruptions of Laki, Iceland; Kuwae, Vanuatu and Eldgjá, Iceland were recently found across eight sites in the Western Hemisphere (Tankersley et al., 2018). However, no direct link currently exists between the Pt spike found by Petaev et al. (2013) within the GISP2 ice core and the Laacher See eruption.

2.2.5. Project Aims

The primary aim of this project is to compare LST geochemistry with GISP2 spike geochemistry, as reported in Petaev et al. (2013), to determine if the Pt spike could have resulted from the Laacher See eruption. Key objectives of the research

were to obtain numerous LST samples and then analyse their geochemistry for the same elements as in the GISP2 spike. Petaev et al. (2013) highlighted the unusual Pt/Ir and Pt/Al ratios of the GISP2 spike ice, and this report compares the geochemical ratios of the LST, GISP2 Pt spike, and literature values of ET and volcanogenic derived rocks; if the LST is geochemically similar to the GISP2 spike, it provides strong evidence against the YDIH, suggesting that the Pt anomaly simply reflected the eruption rather than a bolide impact. If, however, the LST is not geochemically akin to the GISP2 spike, this would eliminate the LSE eruption as a possible source of the Pt, thereby supporting an alternative hypothesis (for example, a bolide impact) if other literature values are found to match GISP2 Pt spike geochemistry. A secondary aim is to re-examine the timing of the GISP2 Pt spike on the newest available age-depth correlation and compare to the timing of other events such as the LSE and the YD. Lastly, the GISP2 Pt spike and its possible source are discussed in the context of climate implications and the YD onset.

3. Site Setting

The Laacher See volcano (50°24’48 ”N, 7°16’19 ”E) is located in Rhineland-Palatinate, western Germany, ~40km south of the city of Bonn (Fig. 2.1). The volcano is part of the active intraplate East Eifel volcanic field (Baales et al., 2002; Reide, 2016). Laacher See erupted explosively at 12.880±40 ka BP, producing sulfate-rich evolved phonolite and sulfide-rich mafic phonolite and distributing pumice and ash across Europe (Bogaard & Schmincke, 1985; Harms & Schmincke, 2000; Baales et al., 2002; Baldini et al., 2018). The eruption comprised Plinian and phreatomagmatic eruptive phases, emplacing fallout and flow deposits categorised into three major tephra units (Fig. 2.2): i) the LLST; ii) the MLST and iii) the ULST (Bogaard & Schmincke, 1985).

To assess the geochemistry of the Laacher See tephra, fieldwork was undertaken at outcrops of the eruptive products close to Laacher See. A total of seven localities were visited during fieldwork, and samples of juvenile material were taken from three sites chosen for the best exposure of the LLST, MLST and ULST (LST1, LST2 and LST3 respectively).

3.1. LST1

Locality LST1 is a quarry (50°24’38” N, 7°22’31” E) ~7km east of Laacher See’s crater. It is a ~1.8m high outcrop of the LLST which directly overlies older sediments (Plate 1a, 1c). The lowermost LLST is a poorly to moderately poorly sorted pyroclastic fall deposit composed of cream to beige fine grained (rare coarse grained), sub-rounded to sub-angular, pumice lapilli up to 2cm in diameter with tubular vesicles, mixed with 2-5% brown to black, fine grained, sub-rounded to sub-angular lithic clasts of Devonian slate (xenoliths) (Plate 1b). After ~1m, there is a gradational boundary into a diffusely bedded, moderately sorted layer (0.6m thick) of fine to coarse, sub-angular to angular pumice lapilli with 10-30% sub-angular to angular slate xenoliths (unit A; Plate 1e). A sharp boundary at ~1.6m represents a transition to a ~0.2m thick ‘big bang’ (BB) layer (see Section 2.2.3.1; Plate 1d), comprising a moderately sorted to well sorted unit of white, coarse grained, sub-angular to angular pumice lapilli, mixed with 30-50% sub-angular to angular slate xenoliths. A thin layer of ash (~1cm) is visible in the centre of the BB layer.

LST1 was chosen for its well exposed outcrop of the entire LLST, with a clear, thick BB layer comprising pumice and lithics which demonstrates conduit collapse and crater shift during the eruption, before a sharp boundary marks the MLST.

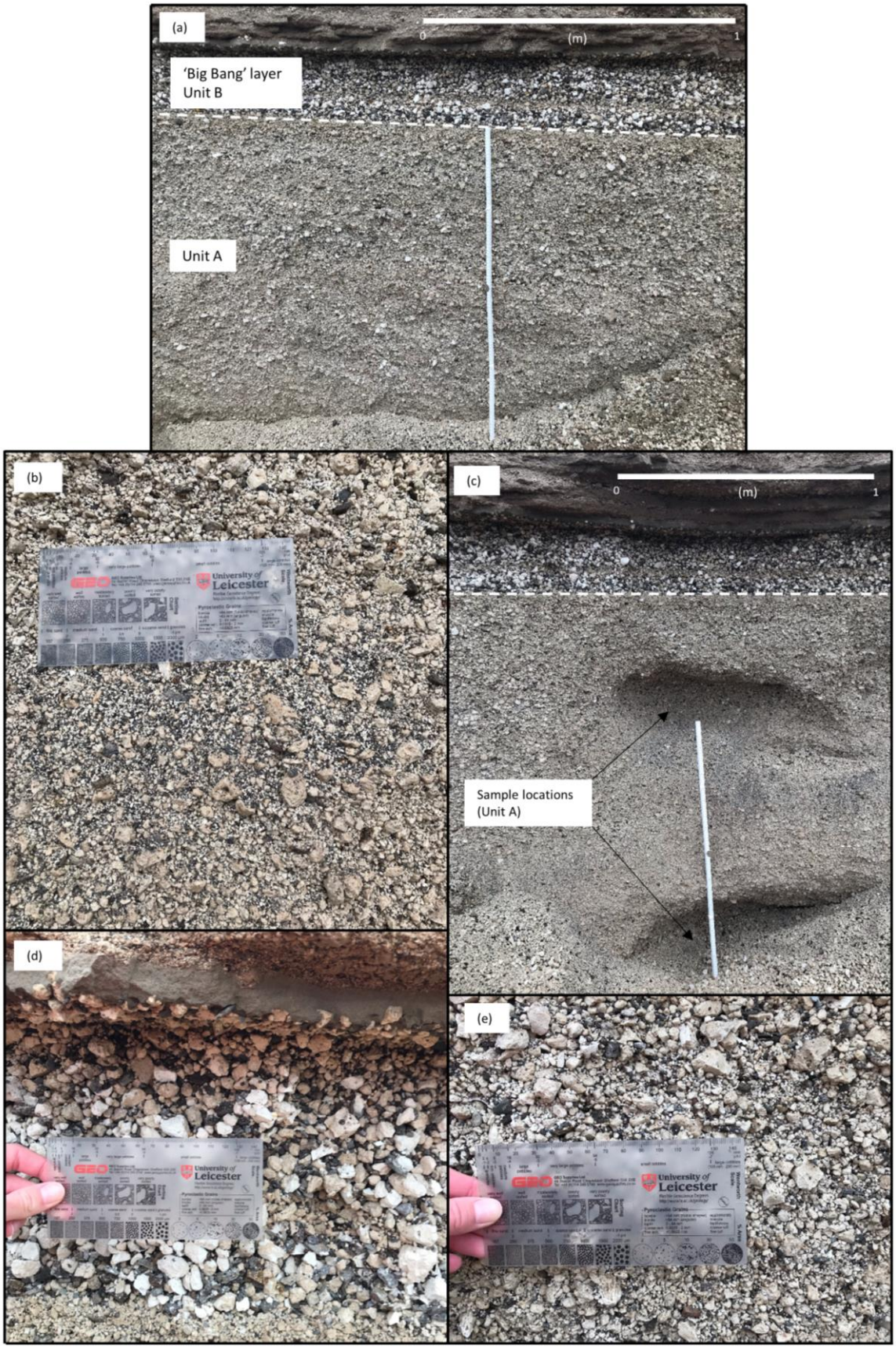

Plate 1: LST1: LLST (a) LLST outcrop, (b) lower LLST pumice-rich layer (~20cm from base of outcrop), (c) full outcrop showing sample locations for unit A, (d) 'big bang' layer in the uppermost LLST and (e) upper pumice-rich layer of unit A.

3.2. LST2

Locality LST2 is a quarry (50°24'20 "N, 7°19'31.63"E) located south of the town of Nickenich at ~4km SE from Laacher See's vent. The locality provides a ~6m high exposure of the MLST pyroclastic fallout deposits, directly above the BB layer (Plate 2a). For ~2.4m, the outcrop (Plate 2a) comprises dark grey, fine, muddy ash layers (Plate 2b, 2c; 5-8cm thick) alternating with poorly sorted pumice rich layers (10-20cm thick) (unit A). The pumice rich layer (Plate 2d) is 70% white, fine to coarse, sub-angular to angular pumice lapilli with tubular vesicles and mixed with dark brown to black, fine to coarse, sub-angular to angular slate xenoliths (30%). Lithic content decreases up through the pumice-rich layers, and they become better sorted. At ~2.4m, a sharp boundary marks the transition (Plate 2e) to a large, moderately sorted pumice rich bed (unit B; Plate 2c), with white to cream, sub-angular to sub-rounded pumice lapilli (more rounded towards the top), and 10-30% angular to sub-rounded slate xenoliths (Plate 2f). Some thin, fine-grained laterally discontinuous layers alternate with the pumice rich layers. The pumice lapilli become grey, denser and more phenocryst-rich with more rounded vesicles (Plate 2g) at around 4.5m, before the layer transitions into soil with rare pumice and slate xenoliths in a mud matrix (Plate 1h).

The locality was chosen for its accessible, clear exposure of the MLST, notably its thick fallout layers (for sampling), distinct boundary between LLST and MLST and an observable transition from lighter, cream-coloured phenocryst-poor pumice to denser, grey phenocryst-rich pumice that represents a compositional change in the magma chamber.

Plate 2: LST2: MLST (a) outcrop, looking west, (b) close-up of unit A, (c) fine ash layer above LLST 'big bang' layer, (d) unit A pumice-rich layer, (e) transition between unit A and unit B, (f) unit B pumice-rich layer, (g) grey, dense phenocryst-rich pumice in unit B and (h) weathered profile at the top of the outcrop.

3.3. LST3

Locality LST3 (50°23’30” N, 7°16’23” E) is near the tourist attraction Wingertsbergwand, north of Niedermendig and ~2km south of Laacher See’s vent. The locality has a large outcrop of ULST, approximately ~20m in vertical extent, comprising pyroclastic density current (PDC) deposits. Coarse, pumice lapilli rich layers are interbedded with ash layers and dune-bedded layers representing filled channels. Lower parts of the outcrop comprise cross-stratified layers, thin, moderately sorted pumice lapilli and ash layers and some dune-bedded layers (unit A). The middle of the outcrop comprises grey, coarse-grained poorly sorted clast rich layers with mixed lithologies of pumice lapilli, cumulate and plutonic rock fragments and slate xenoliths (unit A). The pumice is cream to grey and phenocryst rich. Pumice lapilli, slate xenoliths and cumulate clasts are angular to sub-rounded, with a maximum size of ~10cm. The upper outcrop is composed of laminated fine and coarse flow layers, with some thin, fine ash layers and blocks or bombs (some >50cm) with associated impact craters (unit B).

LST3 was chosen for its thick, well exposed outcrop of the ULST, comprising primarily PDC deposits that represent the LSE’s terminal phreatomagmatic phase, and its accessible clast-dominated coarse layers (for sampling).

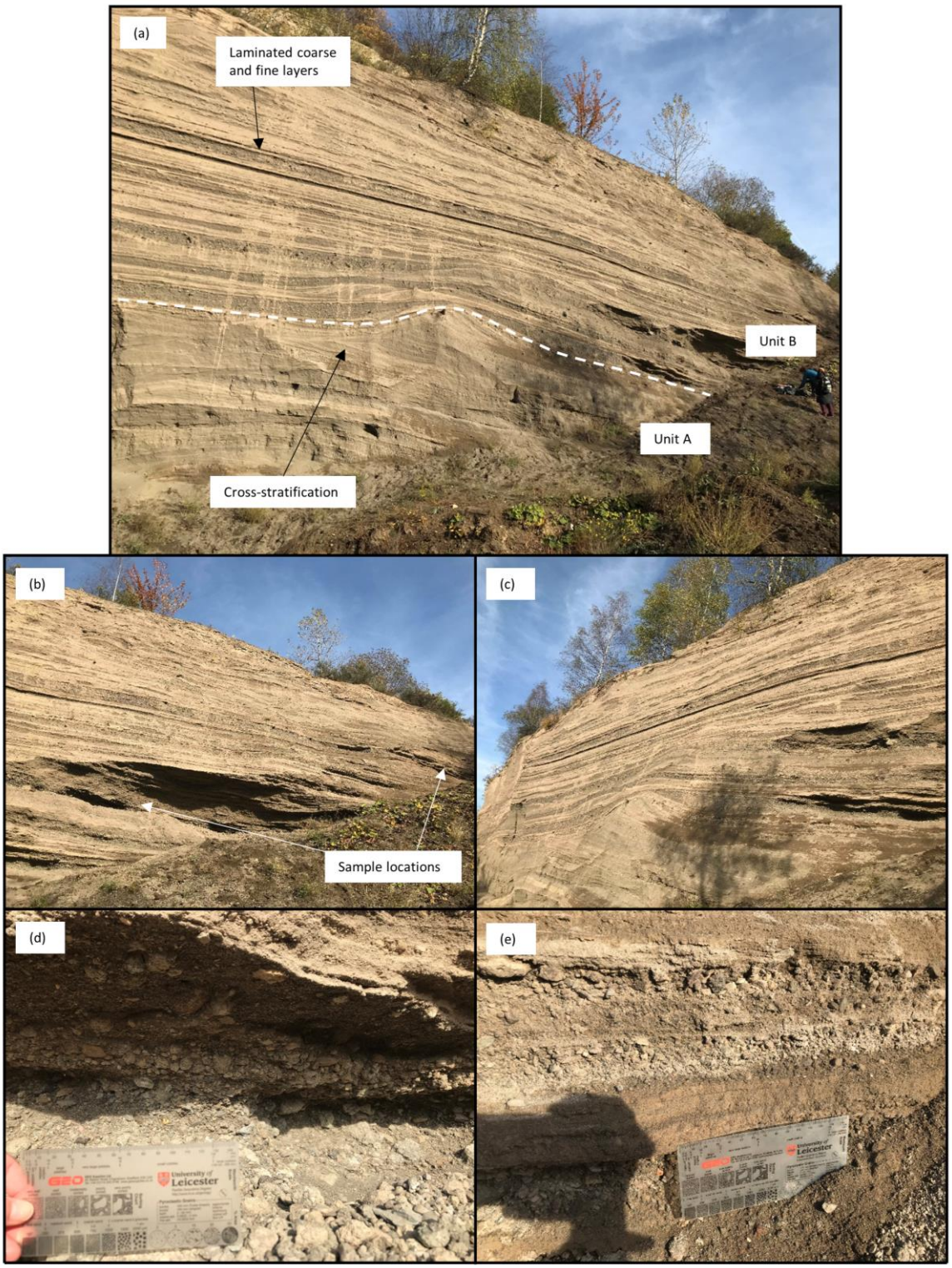

Plate 3: LST3: ULST (a) outcrop of ULST (approximately ~20m high), (b) close-up of outcrop showing sample locations, (c) close-up of outcrop showing clear laminated layers, (d) clast-dominated coarse layer and (e) alternating clast-rich layers with fine ash layers.

4. Methodology

4.1. Sample Collection

Samples were obtained from three localities within 10km of Laacher See directly from the outcrop. The face of the outcrop was cleared using a plastic spade, which was used to excavate approximately 10-20cm into the face of the outcrop. This precaution was taken to remove tephra that may have been heavily contaminated by surface contamination, considering the location of the sites within quarried areas and the use of heavy machinery (excavators) with diesel engines. Catalytic converters in diesel engines are known to emit platinum and could interfere with results (Soyol-Erdene et al., 2011). Individual pumice clasts with few to zero visible lithics were selected and picked using nitrile gloves where possible, and were placed into plastic sample bags and labelled. In total, 18 sample bags were filled from the lower Laacher See tephra (LLST), middle Laacher See tephra (MLST) and upper Laacher See tephra (ULST) units. The samples collected were as follows: LLST: LST001, LST001A, LST002, LST002A, LST003, LST003A and LST003B; MLST: LST004, LST005, LST006, LST007 and LST007A and ULST: LST008. At least 1kg of each sample was obtained as recommended by Activation Laboratories, where the samples were to be analysed. To investigate element concentrations of the general outcrop and country rock dispersed in the eruption, bulk samples and samples of lithics were collected in addition to pumice. One sample of topsoil from the LLST outcrop was collected to investigate the potential impact of diesel engine excavators on surrounding exposed facies. For transport, samples were double bagged in plastic sample bags to reduce potential damage.

4.2. Sample Preparation

Samples were handled with special attention towards reducing potential contamination, soaked for approximately two hours in glass beakers filled with deionised water and rinsed with deionised water in the laboratory. The samples were left to dry over a few days and re-bagged in labelled plastic bags, before later being placed on baking paper in an aluminium tray and dried overnight in a laboratory oven at 70°C to ensure the samples were completely dry prior to analysis. Nitrile gloves were used to handle the clean samples. Four extra samples labelled as Sample A-D were sent to the lab for quality control – Sample A was from LST003, B was LST007, C was LST005 and D was LST008.

Activation Laboratories (ActLabs) prepared the whole rock samples through crushing and pulverising, and smaller samples were pulverised to 95% passing 74µm. The topsoil sample (LST1 TS) was dried to 60°C and sieved.

4.3. Sample Analysis

The following methods used by ActLabs for sample analysis are as described on the “Geochemistry” section of their website (ActLabs, 2019).

4.3.1. Fire Assay ICP-MS

To analyse for gold (Au), platinum (Pt) and palladium (Pd), with lower detection limits of 1 parts per billion (ppb), 0.1 ppb and 0.1 ppb respectively, a fire assay and inductively coupled plasma mass spectrometry (ICP-MS) method is used after Hoffman and Dunn (2002). A sample size of at least 50g was recommended, and this addresses a “nugget effect” that may occur with Pt distribution within a medium (e.g. Firestone et al., 2007; Moore et al., 2017).

The sample is combined with fire assay fluxes (borax, soda ash, silica, litharge) and the mixture is placed in a fire clay crucible, with silver (Ag) included as a collector. The entire fusion process takes approximately 60 minutes, with the mixture preheated at 850°C, intermediate 950°C and finish 1060°C. The crucibles are extracted from the assay furnace, a lead button remaining at the bottom of the mould as the molten slag is poured from the crucible into a mould. The lead button is then positioned in a preheated cupel (cupelled at 950°C) which absorbs the lead and allows the Ag (doré bead) + Au, Pt and Pd to be recovered.

To stop the Au, Pd and Pt from adsorbing onto the test tube, the Ag doré bead is digested in hot HNO3 + HCl at 95°C with a special complexing agent. A Perkin Elmer Sciex ELAN 6000, 6100 or 9000 ICP/MS is utilised following two hours of cooling to analyse for Au, Pt and Pd. A tray of 42 samples includes two method blanks, three sample duplicates, and two certified reference materials and every 45 samples the ICP/MS is recalibrated. Smaller sample splits are utilised for high chromite or sulfide samples.

4.3.2. Nickel Sulfide Fire Assay INAA

To analyse for iridium (Ir), osmium (Os), ruthenium (Ru) and rhodium (Rh), a nickel sulfide (NiS) fire assay procedure and instrumental neutron activation analysis (INAA) technique is utilised after Hoffman et al. (1978) and Hoffman (1992) on samples up to 25g. Using HCl, the nickel sulfide button is dissolved, and the

resulting residue containing all the PGE and Au is gathered on filter paper. Two irradiations and three separate counts are used on the residue to measure PGE and Au. One batch of 34 samples includes two blanks, three certified standards and three duplicates.

The INAA analytical technique measures gamma radiation induced in the sample by irradiation with neutrons which are sourced from a nuclear reactor. A “fingerprint” of gamma radiation is released by each element which is then measured and quantified. Measurements are in ppb and detection limits are as follows: Os (2); Ir (0.1); Ru (5) and Rh (0.2).

4.3.3. Lithium Metaborate/Tetraborate Fusion ICP and ICP-MS

A combination of lithium metaborate/tetraborate fusion ICP whole rock for major elements and ICP-MS for trace elements is used.

4.3.3.1. Lithium Metaborate/Tetraborate Fusion ICP

A batch system is used, with each batch containing a method reagent blank, certified reference material and 17% replicates. Samples are fused in an induction furnace following mixing with a lithium metaborate and lithium tetraborate flux. A 5% nitric acid solution containing an internal standard is instantly mixed with the molten melt until the melt is completely dissolved (~30 minutes). Using a combination simultaneous/sequential Thermo Jarrell-Ash ENVIRO II ICP or a Varian Vista 735 ICP, major oxides and selected trace elements are analysed in the samples. Seven prepared USGS and CANMET certified reference materials are used for calibration. For every group of ten samples, one of the seven standards is utilised during analysis.

Totals should fall between 98.5% and 101%. Sulfate or other elements like Li which are not commonly scanned for may result in lower totals, following this, samples are scanned for base metals. Low totals result in re-fusion and reanalysis of the samples.

4.3.3.2. Lithium Metaborate/Tetraborate ICP-MS

Perkin Elmer Sciex ELAN 6000, 6100 or 9000 ICP/MS are used for analysis after dilution of the fused sample. Per group of samples, three blanks and five controls (three before sample group and two after) are analysed, and every 15 samples the duplicates are fused and analysed. Recalibration of the instrument occurs every 40 samples.

4.4. Timing of the Pt Spike

Original ice-core data of Pt, Ir, Hf, Lu and Al in the GISP2 ice core was obtained from Petaev et al. (2013). The data used the GISP2 Meese-Sowers timescale (Meese et al., 1997), however to compare to other ice core records and sedimentary records using the most recent GISP2 chronology, it was necessary to convert all ice ages to the newer Greenland Ice Core Chronology 2005 (GICC05) composite timescale, which utilised multi-parameter counting of annual layers in the DYE-3, GRIP and NGRIP ice cores and an ice flow-based modelling extension; GICC05modelext (Andersen et al., 2006; Rasmussen et al. 2006; Svenson et al., 2006; Vinther et al., 2006). An updated timescale (available from http://www.iceandclimate.nbi.ku.dk/data/) that synchronised the GRIP, NGRIP and GISP2 ice cores was later presented (Rasmussen et al., 2014; Seierstad et al., 2014). The GICC05modelext timescale was utilised to convert the Pt data to the newest ice core chronology, with error margins of roughly ± 140 years. After conversion, the 'middle' depth of the ice samples was calculated using the top and bottom depth, as in Petaev et al. (2013), and the age of this was calculated using top and bottom ages (b2k) then converted to years BP 1950. Therefore, an age (on the GICC05modelext timescale) was obtained for the Pt, Ir, Hf, Lu and Al data of Petaev et al. (2013) and plotted onto a graph (see Chapter 5). The $\delta^{18}O$ data in the GISP2 and NGRIP ice cores on the GICC05 timescale was also obtained from Seierstad et al. (2014; and references therein) and the volcanogenic sulfate from Mayewski et al. (1997) also on the GICC05modelext timescale.

4.5. Limitations

Due to time constraints, the geochemical analysis in this study was provided by ActLabs – a commercial lab – and thus the detection limits of some elements were high in comparison to other studies discussed later in this report (see Petaev et al., 2013). The methods with the lowest possible detection limit were selected for the Platinum Group Elements (PGEs), with a focus on Pt, of which the detection limit of 0.1 ppb is lower than Pt crustal abundance. Most PGEs were below detection limit, but those with detectable concentrations were close to the detection limit and this suggests uncertainties within the data. Therefore, the precise concentrations of Pt for example are uncertain, but we can safely assume that they are very low within the LST.

5. Results

5.1. Timing of the GISP2 Pt Spike

The geochemical concentrations in the GISP2 ice core presented by Petaev et al. (2013) were dated on the "Meese-Sowers timescale" depth-age scale (Meese et al., 1997). However, a newer timescale, the GICC05 composite timescale and its ice flow modelling extension GICC05modelext (Andersen et al., 2006; Rasmussen et al. 2006; Svenson et al., 2006; Vinther et al., 2006) became available, followed by a further development of the event stratigraphy that synchronised the GRIP, NGRIP and GISP2 ice cores (Rasmussen et al., 2014; Seierstad et al., 2014). Therefore, it is necessary to convert to the newest timescale for comparison to other ice cores (e.g. North Greenland Ice Sheet Project; NGRIP) and sedimentary successions. Furthermore, the GICC05modelext timescale is in years b2k (before 2000) and is converted to years ka BP (before 1950) here. The steps taken during the conversion process are explained in detail in Chapter 4.

Petaev et al. (2013) measured Pt concentrations in the GISP2 ice core in the depth interval 1719.875 to 1709.000 m, representing the age range ~12.72 to 13.00 ka BP (GICC05 timescale). The mean Pt concentration across this interval is ~3.6 ppt, which is considered a 'baseline' for the depth interval discussed in this report. The minimum concentration is 0.038 ppt at ~12.89 ka BP, and the maximum Pt concentration of 82.2ppt, which is considered a "spike", is recorded at GISP2 depth interval 1712.250 to 1712.125 m equivalent to 12.824 ka BP to 12.821 ka BP – or a "middle age" of 12.822 ka BP (Fig. 5.1). Elevated Pt concentrations (in respect of the surrounding ice baseline) are found from depths 1712.625 to 1712.000 m, which represents the age range 12.833 ka BP to 12.819 ka BP on the GICC05modelext timescale (Fig. 5.1).

5.2. Comparison with Other Records

The GISP2 Pt spike timing was compared to select ice core records of volcanogenic sulfate in the GISP2 ice core and bidecadal $\delta^{18}O$ in the NGRIP and GISP2 ice cores (Fig. 5.1). The LSE sulfate spike (12.867 ka BP; Baldini et al., 2018) and $\delta^{18}O$ decrease in the NGRIP ice core are essentially synchronous (Fig. 5.1), and the Pt spike occurs ~60 years after the LSE and $\delta^{18}O$ decline and ~20 years after GS-1 onset (Rasmussen et al. 2014). The GISP2 $\delta^{18}O$ record begins to drop ~20 years before NGRIP $\delta^{18}O$ and the LSE sulfur spike.

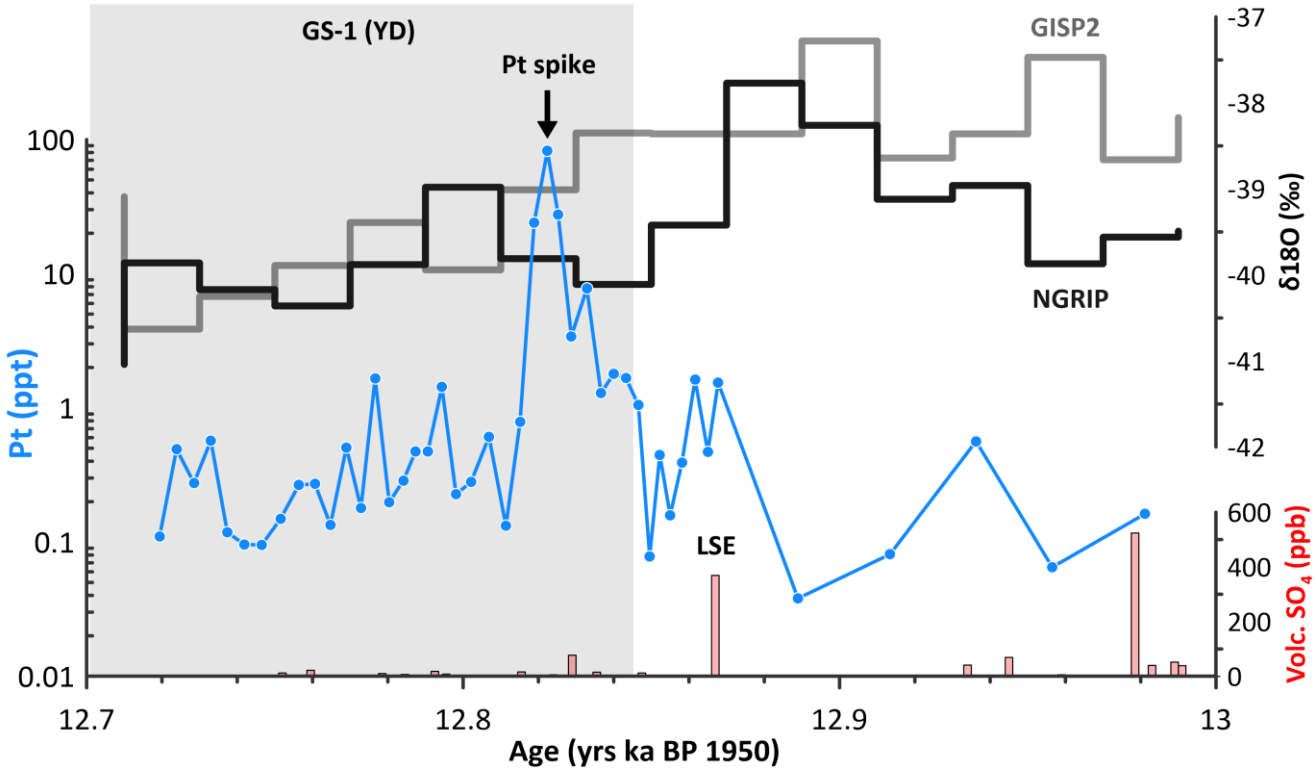

Figure 5.1: Platinum (parts per trillion; ppt) concentrations in the GISP2 ice core (Petaev et al., 2013); Volc. SO_4 (volcanogenic sulfate, recorded in parts per billion; ppb) in the GISP2 ice core with the LSE sulfate spike labelled (Mayewski et al., 1997; Baldini et al., 2018) and bidecadal (20 year mean) $\delta^{18}O$ (permil; ‰) in the NGRIP and GISP2 ice cores (Seierstad et al., 2014 and references therein). The grey box represents GS-1 onset in this age interval as defined by Rasmussen et al. (2014).

5.3. Geochemistry of the Laacher See Tephra

Whole rock geochemistry was analysed by ActLabs using fusion ICP, ICP-MS and INAA techniques (see Chapter 4) in 17 samples of pumice and lithic clasts (or both; bulk samples) of the LLST, MLST and ULST units. LST geochemistry in this section is discussed in reference to each unit of the LST, inclusive of pumice samples only, unless otherwise stated. A topsoil sample from locality LST1 was also analysed to assess the degree of contamination by pollutants in the soil (namely from catalytic convertors). A full set of chemical analyses are provided in Appendix 1, and individual elements are discussed in the sections below.

5.3.1. Absolute Abundances

5.3.1.1. Major Elements

The major elements analysed in this study by Fusion ICP-MS are: silicon (Si), measured as silicon dioxide (SiO_2); aluminium (Al), measured as aluminium oxide (Al_2O_3); iron (Fe), measured as iron(III) oxide (Fe_2O_3); manganese (Mn), measured as manganese(II) oxide (MnO); magnesium (Mg), measured as magnesium oxide (MgO); calcium (Ca), measured as calcium oxide (CaO); sodium (Na), measured as sodium oxide (Na_2O); potassium (K), measured as potassium oxide (K_2O); titanium (Ti), measured as titanium dioxide (TiO_2) and phosphorous (P), measured as phosphorous pentoxide (P_2O_5). All elements were measured in wt%. A summary of the minimum, maximum and mean values of the major elements in each unit of the LST and the LST in its entirety is provided in this chapter (Table 5.1). The same statistical analysis is applied to bulk and lithics samples (Table 5.2).

Table 5.1: Results of geochemical analyses of major elements in the pumice samples of the LST.

Unit	**Value**	SiO_2	Al_2O_3	Fe_2O_3	MnO	MgO	CaO	Na_2O	K_2O	TiO_2	P_2O_5
LLST	Min.	55.92	20.59	1.92	0.42	0.07	0.40	10.18	4.88	0.14	0.01
	Max.	56.73	21.37	1.99	0.48	0.09	0.50	10.53	5.11	0.16	0.03
	Mn.	56.31	20.93	1.94	0.45	0.08	0.46	10.35	4.96	0.15	0.02
MLST	Min.	56.63	19.19	2.07	0.18	0.12	0.98	5.94	5.64	0.22	0.03
	Max.	58.72	20.60	2.93	0.27	0.37	1.91	8.74	6.59	0.54	0.09
	Mn.	57.60	20.09	2.50	0.23	0.24	1.40	7.51	6.04	0.36	0.05
ULST	Min.	54.72	17.92	3.40	0.13	0.65	5.34	4.82	6.53	0.83	0.16
	Max.	55.29	18.75	3.82	0.14	0.76	7.03	4.83	6.72	0.95	0.18
	Mn.	55.01	18.34	3.61	0.14	0.71	6.19	4.83	6.63	0.89	0.17
LST*	Min.	54.72	14.52	1.92	0.13	0.07	0.32	1.16	2.68	0.14	0.01
	Max.	68.02	21.37	6.75	0.48	1.50	7.03	10.53	6.72	0.95	0.18
	Mn.	58.52	19.24	2.93	0.29	0.39	1.53	7.36	5.25	0.39	0.07

All values are in weight percent (wt%) to 2 decimal places (d.p.). Min. = Minimum; Max. = Maximum, Mn. = Mean value.

*LST refers to the entire Laacher See tephra unit.

Table 5.2: Geochemical analysis results for major elements in bulk and lithics samples from the LLST.

	Element									
Sample	SiO_2	Al_2O_3	Fe_2O_3	MnO	MgO	CaO	Na_2O	K_2O	TiO_2	P_2O_5
LST 001A	61.73	17.65	3.24	0.38	0.55	0.65	7.11	3.83	0.33	0.08

	Element									
Sample	SiO_2	Al_2O_3	Fe_2O_3	MnO	MgO	CaO	Na_2O	K_2O	TiO_2	P_2O_5
LST 002A	63.57	16.88	3.53	0.37	0.61	0.58	6.82	3.64	0.34	0.07
LST 003A	63.08	17.08	3.83	0.33	0.57	0.43	6.47	3.75	0.36	0.06
LST 003B	68.02	14.52	6.75	0.17	1.50	0.32	1.16	2.68	0.78	0.17

All values are in wt% (2 d.p.).

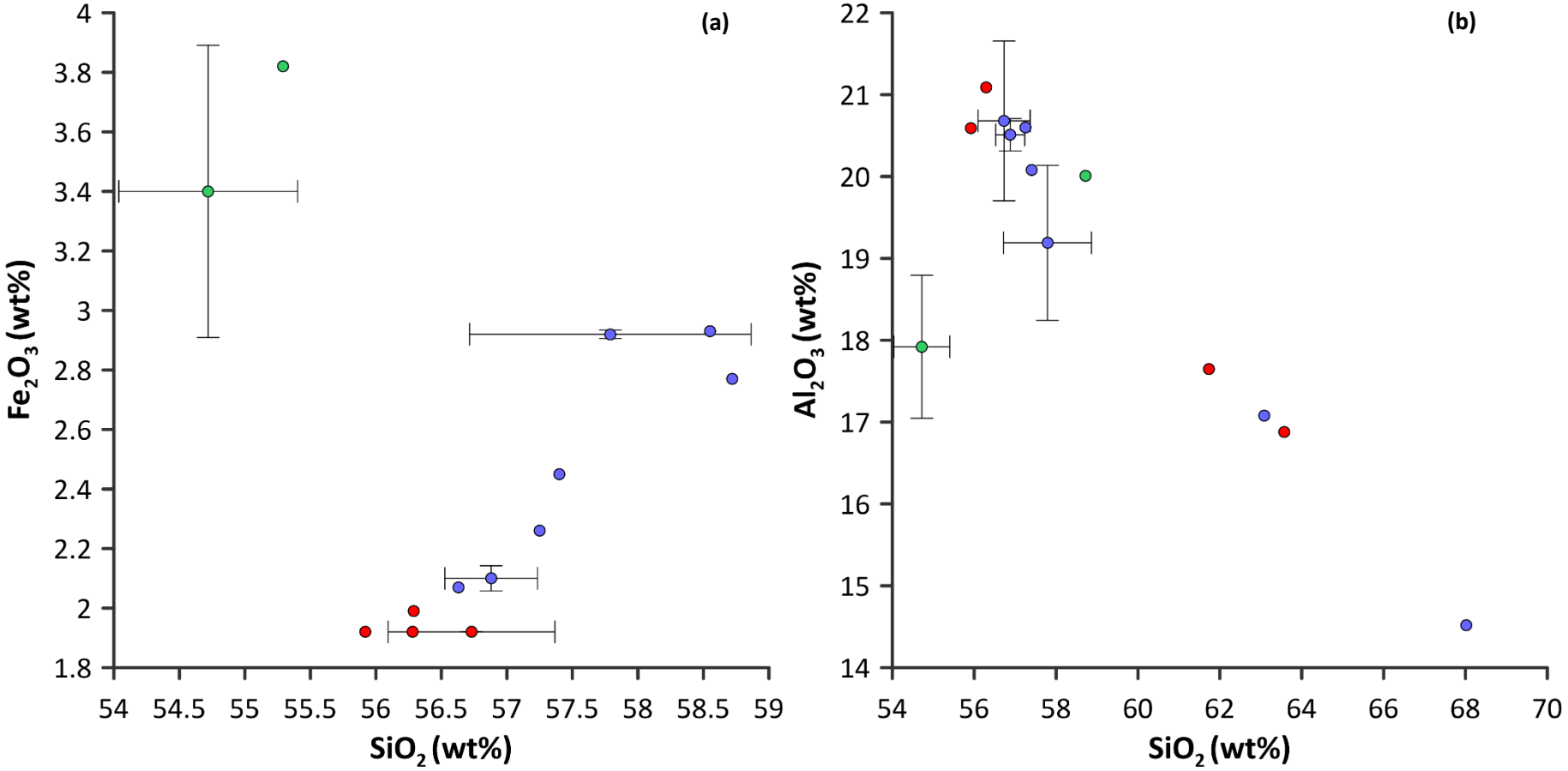

Figure 5.2: Bivariate plots of major elements a) Fe_2O_3 against SiO_2 and b) Al_2O_3 against SiO_2 (all measured in wt%) in the LST (excluding bulk and lithics). Circles are: green (ULST), purple (MLST) and red (LLST). Error bars show two times the standard deviation of samples with duplicates or triplicates.

The mean SiO_2 composition of the LST increases from the basal LLST to the MLST, then decreases from MLST to ULST (Table 5.1). Aluminium oxide ($Al_2O_{3)}$, MnO and Na_2O all demonstrate decreasing trends from LLST to ULST, whereas Fe_2O_3, MgO, CaO, K_2O, TiO_2 and P_2O_5 all show a systematic increase from LLST to ULST. These major element trends are consistent with analysis of glass shards within the LST by Bogaard and Schmincke (1985). Trends in magma composition are affected when bulk and lithic samples are included (Table 5.3), as these incorporate the country rock which varies geochemically from the Laacher See pumice. When plotted against SiO_2, Fe_2O_3 shows weak positive correlation between the LLST and MLST, however, the ULST shows no correlation (Fig. 5.2a). In comparison, Al_2O_3 against SiO_2 shows strong negative correlation in all but one ULST sample (Fig. 5.2b).

5.3.1.2. Trace Elements

The trace elements analysed in this study by ICP-MS and INAA techniques are: scandium (Sc); beryllium (Be); vanadium (V); barium (Ba); strontium (Sr); yttrium (Y); zircon (Z); chromium (Cr); cobalt (Co); nickel (Ni); copper (Cu); zinc (Zn); gallium (Ga); germanium (Ge); arsenic (As); rubidium (Rb); niobium (Nb); molybdenum (Mo); silver (Ag); indium (In); tin (Sn); antimony (Sb); caesium (Cs); lanthanum (La); cerium (Ce); praseodymium (Pr); neodymium (Nd); samarium (Sm); europium (Eu); gadolinium (Gd); terbium (Tb); dysprosium (Dy); holmium (Ho); erbium (Er); thulium (Tm); ytterbium (Yb); lutetium (Lu); hafnium (Hf); tantalum (Ta); tungsten (W); thallium (Tl); lead (Pb); bismuth (Bi); thorium (Th); uranium (U); osmium (Os); iridium (Ir); ruthenium (Ru); rhodium (Rh); platinum (Pt); palladium (Pd); gold (Au) and rhenium (Re). A summary of the minimum, maximum and mean values of the trace elements in each unit of the LST (and the entire LST) is shown in Table 5.3. Elements below detection limit (bdl) were excluded from any statistical analysis, thus the datasets shown in Tables 5.3 and 5.4 are left censored.

Table 5.3: Results of geochemical analysis of trace elements in the pumice samples of the LST.

	Element	*Sc*			*Be*			*V*			*Ba*		
	Values	Min.	Max.	Mn.	Min.	Max.	Mn.	Min.	Max.	Mn.	Min.	Max.	Mn.
Unit	**LLST**	bdl	bdl	bdl	16	20	18	8	9	9	14	22	18
	MLST	1	1	1	3	7	5	16	43	29	85	408	220
	ULST	1	2	2	2	2	2	68	78	73	1286	1472	1379
	LST*	1	2	1	2	20	9	8	78	29	14	1472	336

	Element	*Zr*			*Cr*			*Co*			*Ni*			*Cu*		
	Values	Min.	Max.	Mn.	Min.	Max.	Mn.	Min.	Max.	Mn.	Min.	Max.	Mn.	Min.	Max.	Mn.
Unit	**LLST**	1752	2109	1921	bdl	bdl	bdl	1	1	1	bdl	bdl	bdl	bdl	bdl	bdl
	MLST	438	859	670	bdl	bdl	bdl	1	2	2	bdl	bdl	bdl	bdl	bdl	bdl
	ULST	239	244	242	bdl	bdl	bdl	3	3	3	bdl	bdl	bdl	bdl	bdl	bdl
	LST*	239	2109	989	bdl	bdl	bdl	1	3	2	bdl	bdl	bdl	bdl	bdl	bdl

	Element	*Ga*			*Ge*			*As*			*Rb*		
	Values	Min.	Max.	Mn.	Min.	Max.	Mn.	Min.	Max.	Mn.	Min.	Max.	Mn.
Unit	**LLST**	49	55	52	2	3	2	9	13	11	480	540	507
	MLST	23	34	29	1	2	1	7	8	8	178	306	248
	ULST	17	18	18	bdl	bdl	bdl	bdl	bdl	bdl	114	116	115
	LST*	17	55	34	1	3	1	7	13	10	114	540	307

	Element	*Ag*			*In*			*Sn*			*Sb*		
	Values	Min.	Max.	Mn.	Min.	Max.	Mn.	Min.	Max.	Mn.	Min.	Max.	Mn.
Unit	**LLST**	4.3	5.2	4.9	bdl	bdl	bdl	2	2	2	1.3	1.7	1.5
	MLST	1.0	2.1	1.6	bdl	bdl	bdl	1	1	1	0.5	0.7	0.6
	ULST	0.5	0.6	0.6	bdl	bdl	bdl	1	1	1	bdl	bdl	bdl
	LST*	0.5	5.2	2.5	bdl	bdl	bdl	1	2	1	0.5	1.7	1.0

	Element	*Ce*			*Pr*			*Nd*			*Sm*		
	Values	Min.	Max.	Mn.	Min.	Max.	Mn.	Min.	Max.	Mn.	Min.	Max.	Mn.
Unit	**LLST**	243.0	277.0	258.0	15.10	17.00	15.98	31.2	35.3	33.2	3.1	3.4	3.2
	MLST	152.0	174.0	162.3	10.80	12.20	11.53	23.5	32.8	27.7	2.2	4.0	3.0
	ULST	154.0	165.0	159.5	15.00	16.30	15.65	47.3	52.0	49.7	6.5	7.2	6.9
	LST*	152.0	277.0	191.3	10.80	17.00	13.53	23.5	52.0	32.8	2.2	7.2	3.7

	Element	*Tb*			*Dy*			*Ho*			*Er*		
	Values	Min.	Max.	Mn.	Min.	Max.	Mn.	Min.	Max.	Mn.	Min.	Max.	Mn.
Unit	**LLST**	0.4	0.5	0.4	3.0	3.5	3.2	0.8	0.9	0.8	3.1	3.6	3.3
	MLST	0.3	0.4	0.3	1.9	2.5	2.1	0.4	0.5	0.5	1.6	2.0	1.8
	ULST	0.6	0.7	0.7	3.5	3.9	3.7	0.7	0.7	0.7	2.0	2.2	2.1
	LST*	0.3	0.7	0.4	1.9	3.9	2.7	0.4	0.9	0.6	1.6	3.6	2.3

	Element	*Lu*			*Hf*			*Ta*			*W*		
	Values	Min.	Max.	Mn.	Min.	Max.	Mn.	Min.	Max.	Mn.	Min.	Max.	Mn.
Unit	**LLST**	0.98	1.13	1.06	30.8	37.0	33.7	5.6	6.3	6.0	bdl	bdl	bdl
	MLST	0.35	0.55	0.46	7.6	14.8	11.4	3.8	4.9	4.3	bdl	bdl	bdl
	ULST	0.29	0.31	0.30	4.6	4.9	4.8	6.4	6.9	6.7	2	2	2
	LST*	0.29	1.13	0.62	4.6	37.0	17.2	3.8	6.9	5.2	2	2	2

	Element	*Bi*			*Th*			*U*			*Os (ppb)*		
	Values	Min.	Max.	Mn.	Min.	Max.	Mn.	Min.	Max.	Mn.	Min.	Max.	Mn.
Unit	**LLST**	0.4	0.4	0.4	78.6	95.6	85.8	21.6	26.2	23.7	bdl	bdl	bdl
	MLST	bdl	bdl	bdl	16.8	35.7	27.1	4.3	9.6	7.1	9	9	9
	ULST	bdl	bdl	bdl	8.6	8.8	8.7	2.2	2.3	2.3	bdl	bdl	bdl
	LST*	0.4	0.4	0.4	8.6	95.6	42.3	2.2	26.2	11.5	9	9	9

	Element	*Rh (ppb)*			*Pt (ppb)*			*Pd (ppb)*			*Au (ppb)*		
	Values	Min.	Max.	Mn.	Min.	Max.	Mn.	Min.	Max.	Mn.	Min.	Max.	Mn.
Unit	**LLST**	bdl	bdl	bdl	0.2	0.2	0.2	0.1	0.1	0.1	0.7	1.0	0.9
	MLST	bdl	bdl	bdl	0.1	0.1	0.1	0.2	0.2	0.2	0.5	1.4	1.0
	ULST	bdl	bdl	bdl	bdl	bdl	bdl	0.1	0.1	0.1	0.7	0.7	0.7
	LST*	bdl	bdl	bdl	0.1	0.2	0.2	0.1	0.2	0.1	0.5	1.4	0.9

	Element	*Y*			*Sr*			*Zn*			*Nb*		
	Values	Min.	Max.	Mn.	Min.	Max.	Mn.	Min.	Max.	Mn.	Min.	Max.	Mn.
Unit	**LLST**	27	31	29	9	14	12	210	250	228	295	352	321
	MLST	15	17	15	62	314	168	80	130	104	123	160	142
	ULST	19	19	19	1057	1217	1137	60	60	60	104	108	106
	LST*	15	31	20	9	1217	269	60	250	135	104	352	191

	Element	*Cs*			*La*			*Eu*			*Gd*		
	Values	Min.	Max.	Mn.	Min.	Max.	Mn.	Min.	Max.	Mn.	Min.	Max.	Mn.
Unit	**LLST**	10.8	12.7	11.6	197.0	224.0	208.8	0.41	0.44	0.43	2.0	2.5	2.2
	MLST	2.1	4.9	3.6	104.0	139.0	122.6	0.40	1.01	0.67	1.4	2.5	1.9
	ULST	0.9	1.0	1.0	85.9	90.6	88.3	1.82	2.11	1.97	4.2	4.7	4.5
	LST*	0.9	12.7	5.7	85.9	224.0	143.8	0.40	2.11	0.80	1.4	4.7	2.4

	Element	*Tm*			*Yb*			*Tl*			*Pb*			*Mo*		
	Values	Min.	Max.	Mn.	Min.	Max.	Mn.	Min.	Max.	Mn.	Min.	Max.	Mn.	Min.	Max.	Mn.
Unit	**LLST**	0.60	0.72	0.66	5.3	6.1	5.7	0.9	1.1	1.0	42	52	47	2	2	2
	MLST	0.28	0.36	0.32	2.0	2.9	2.5	0.2	0.6	0.4	13	25	19	3	4	3
	ULST	0.28	0.31	0.30	1.9	2.0	2.0	0.1	0.1	0.1	8	10	9	5	5	5
	LST*	0.28	0.72	0.42	1.9	6.1	3.4	0.1	1.1	0.5	8	52	26	2	5	3

	Element	*Ir (ppb)*			*Ru (ppb)*		
	Values	Min.	Max.	Mn.	Min.	Max.	Mn.
Unit	**LLST**	bdl	bdl	bdl	bdl	bdl	bdl
	MLST	bdl	bdl	bdl	bdl	bdl	bdl
	ULST	bdl	bdl	bdl	bdl	bdl	bdl
	LST*	bdl	bdl	bdl	bdl	bdl	bdl

All values in parts per million (ppm) unless stated otherwise, provided to the number of significant figures dictated by individual detection limits (Appendix 1). Bdl = below detection limit. Some samples were bdl for specific elements and this is reflected in the statistical analysis. Min. = Minimum; Max. = Maximum, Mn. = Mean value. *LST refers to entire Laacher See tephra unit.

Table 5.4: Results of geochemical analyses of trace elements in bulk and lithics samples from the LLST.

	Element																
Sample	*Sc*	*Be*	*V*	*Ba*	*Sr*	*Y*	*Zr*	*Cr*	*Co*	*Ni*	*Cu*	*Zn*	*Ga*	*Ge*	*As*	*Rb*	*Nb*
LST 001A	3	14	32	137	64	27	1422	40	6	bdl	bdl	190	41	2	18	398	210
LST 002A	4	12	35	140	62	27	1337	60	7	20	10	170	38	2	10	357	187
LST 003A	5	10	38	153	41	24	1115	60	7	20	bdl	140	35	2	9	320	157
LST 003B	14	2	96	446	85	25	187	130	18	60	20	390	19	2	9	142	11

	Element																	
Sample	*Sn*	*Sb*	*Cs*	*La*	*Ce*	*Pr*	*Nd*	*Sm*	*Eu*	*Gd*	*Tb*	*Dy*	*Ho*	*Er*	*Tm*	*Yb*	*Lu*	*Hf*	*W*
LST 001A	2	1.5	9.8	158.0	203.0	13.6	33.3	4.2	0.69	3.0	0.5	3.7	0.8	3.0	0.58	4.9	0.88	25.0	bdl
LST 002A	2	1.4	8.8	146.0	189.0	13.2	32.3	4.2	0.75	3.1	0.5	3.6	0.8	3.0	0.56	4.5	0.81	23.6	bdl
LST 003A	2	1.2	7.6	128.0	168.0	12.0	30.7	4.2	0.76	3.0	0.6	3.5	0.8	2.7	0.51	3.9	0.72	19.2	bdl
LST 003B	2	0.7	4.4	41.8	82.9	9.56	35.0	6.7	1.43	5.6	0.9	5.0	1.0	2.7	0.41	2.9	0.43	5.1	bdl

	Element															
Sample	*Tl*	*Pb*	*Bi*	*Th*	*U*	*Os (ppb)*	*Ir (ppb)*	*Ru (ppb)*	*Rh (ppb)*	*Pt (ppb)*	*Pd (ppb)*	*Au (ppb)*	*Mo*	*Ag*	*In*	*Ta*
LST 001A	0.9	45	bdl	65.0	18.1	bdl	bdl	bdl	bdl	0.1	0.1	0.8	2.0	4	bdl	4.5
LST 002A	0.9	37	bdl	59.3	16.2	bdl	0.2	bdl	bdl	0.1	0.1	0.8	2.0	3.8	bdl	4.1
LST 003A	0.8	27	bdl	49.1	13.4	bdl	bdl	bdl	bdl	0.2	0.2	1.1	2.0	2.8	bdl	3.5

	Element															
Sample	*Tl*	*Pb*	*Bi*	*Th*	*U*	*Os (ppb)*	*Ir (ppb)*	*Ru (ppb)*	*Rh (ppb)*	*Pt (ppb)*	*Pd (ppb)*	*Au (ppb)*	*Mo*	*Ag*	*In*	*Ta*
LST 003B	0.6	15	bdl	11.1	2.8	bdl	bdl	bdl	bdl	0.4	0.6	2.6	bdl	0.6	bdl	0.9

All elements measured in ppm to 1 d.p. unless stated otherwise. Bdl = below detection limit. Min. = Minimum; Max. = Maximum, Mn. = Mean value.

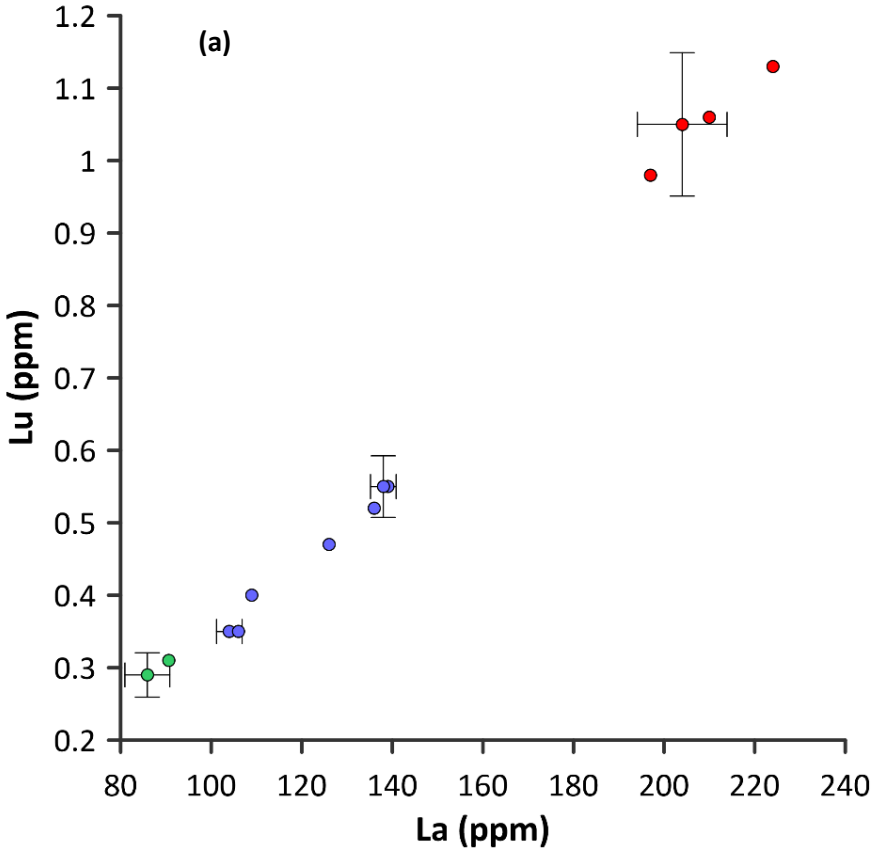

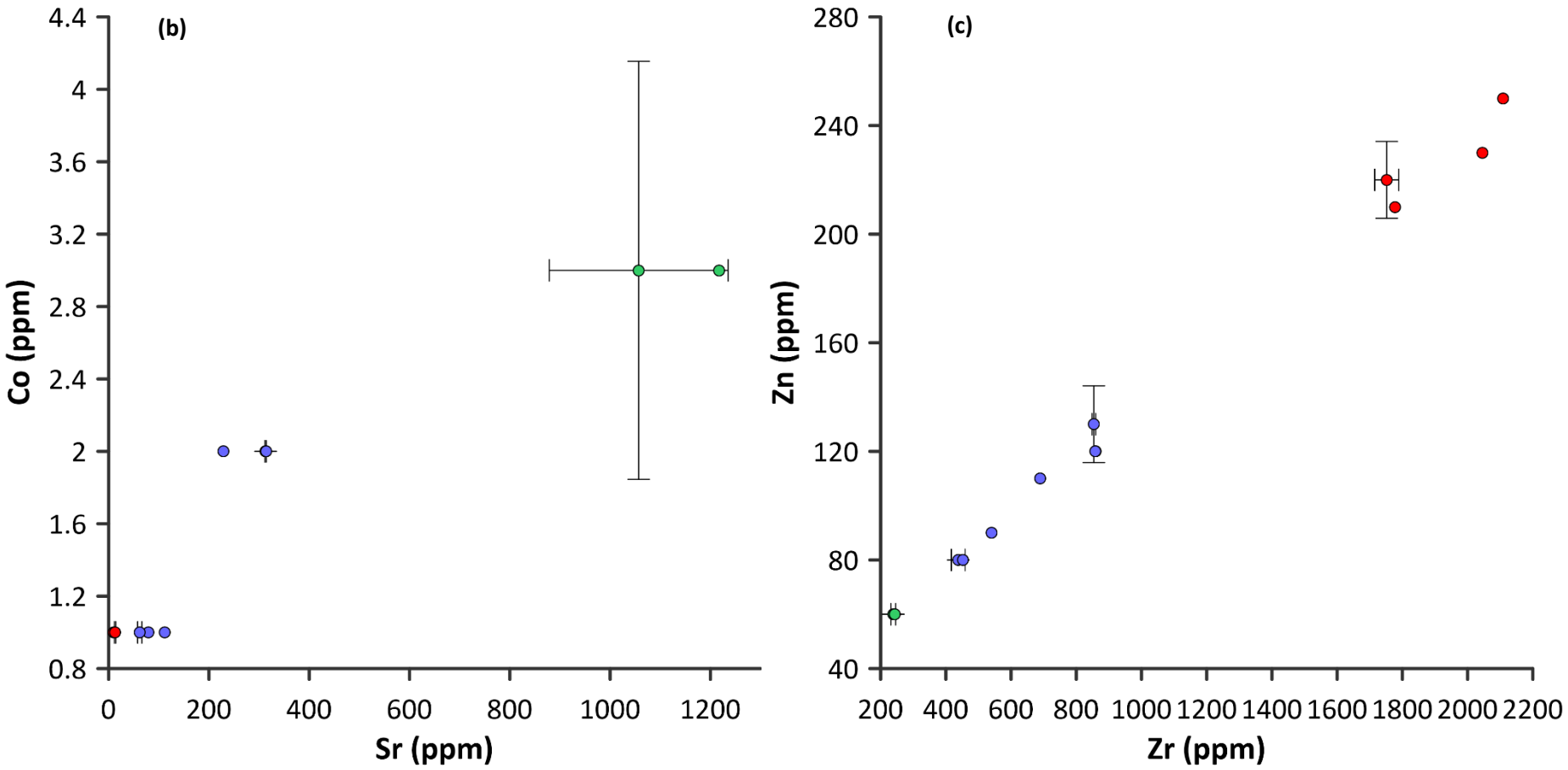

Figure 5.3: Bivariate plots of trace elements: (a) Lu against La; (b) Co against Sr and (c) Zn against Zr (all measured in ppm) in the LST (excluding bulk and lithics). Circles are: green (ULST), purple (MLST) and red (LLST). Error bars show two times the standard deviation of samples with duplicates or triplicates.

Overall, most of the trace element mean concentration values decrease upwards through the deposit. The following elements specifically show a decreasing trend: Be, Zr, Zn, Ga, Ge, As, Rb, Nb, Ag, Sb, Cs, La, Ce, Yb, Lu, Hf, Tl, Pb, Th, U and Pt. In particular, Be, Zr, Zn, Rb, Nb, La, Ce, Hf, Pb, Th and U show a strong decreasing trend from the deposit base to the top. Mean concentrations increase for the following elements as the magma evolved from the LLST to ULST: Sc, V, Ba, Sr, Co, Mo and Eu. Strontium exhibits a particularly strong increasing trend from the basal LLST towards the ULST. Some elemental concentrations increase from the LLST to the MLST, then demonstrate a decreasing trend to the top of the deposit (ULST): Os, Pd and Au. Other mean element concentrations decrease from LLST to MLST, then show an increasing trend from MLST to ULST: Y, Pr, Nd, Sm, Gd, Tb, Dy, Ho, Er and Ta. Mean Sn concentrations decrease from the LLST to MLST, then remain the same concentration of 1.0 ppm from the MLST to ULST. Similarly, Tm concentrations decrease from the deposit base to the MLST, then remain at a concentration of 3.0 ppm through to the top of the deposit. Several elements were below detection limit (bdl) throughout the entire LST: Ir, Cr, Ni, Cu, Ln, Ru and Rh. Tungsten is bdl in the LLST and the MLST before rising to 2.0 ppm in the ULST as the magma evolved. Bismuth decreases from 0.4 ppm at the deposit base to bdl in the MLST, and remains bdl in the ULST. These trends are consistent with whole rock analyses of the LST by Wörner et al. (1983) and Wörner & Schmincke (1984). Compatible element concentrations (e.g. Sr, Sc, Co) increase as the magma evolved (Wörner et al., 1983; Wörner & Schmincke, 1984) and Co against Sr shows a weak positive correlation in this report (Fig. 5.3b). Whereas, incompatible elements (e.g. Zr, Zn, Th) decrease from the basal LLST to the ULST (Wörner et al., 1983; Wörner & Schmincke, 1984), and Zn and Zr show a strong positive correlation in this report (Fig. 5.3c). In addition, the light rare earth elements show a strong positive correlation with the heavy rare earth elements (Fig. 5.3a). The “semicomptaible” elements (e.g. Nd, Y) decrease from LLST to MLST, then increase again from MLST to ULST (Wörner et al., 1983). However, Hf is considered semicompatible in the samples analysed by Wörner et al. (1983), but in this report Hf is incompatible and decreases as the magma evolves. Chromium is bdl in samples analysed in this report, similar to that observed by Wörner et al. (1983).

Selected Trace Elements. Platinum, Ir, Hf and Lu are discussed further, as these constituents were analysed in the GISP2 ice core by Petaev et al. (2013) and will be used for further data analysis in Section 5.3.2.

Platinum and Iridium. Platinum concentrations are low in the LST, close to the lab detection limit (0.1 ppb). The highest mean concentration is found in the basal LLST (0.2 ppb), and concentrations decrease upwards through the deposit until falling bdl in the ULST after magma evolution. Iridium is not detected in the LST pumice samples.

Hafnium and Lutetium. Lutetium and Hf concentrations are well above their respective lab detection limits (0.01 ppm and 0.2 ppm), and both show a decreasing trend from the deposit base to the top. Hafnium in particular shows a strong decreasing trend, from ~34 ppm to ~5ppm.

Anthropogenic Pt. The sample of topsoil (LST1 TS) had Pt concentrations of 0.9 ppb (Appendix 1) which is above crustal abundance. This is likely a result of anthropogenic contamination. Remaining samples are below crustal abundance and thus were not exposed to contamination or surface contamination was removed during sample preparation.

5.3.2. Geochemical Ratios

The elements Pt, Ir, Hf, Lu and Al, were selected for further data analysis, because these were analysed in the GISP2 ice core by Petaev et al. (2013). For comparison between the different mediums analysed in the work by Petaev et al. (2013), this report, and materials in the literature, geochemical ratios were used because absolute abundances are likely to be orders of magnitude different. Before the geochemical ratios were calculated, all values were converted to parts per billion (ppb). The geochemical ratios used are Ir/Al, Hf/Al and Lu/Al plotted against Pt/Al; Ir/Lu and Hf/Lu plotted against Pt/Lu and Ir/Hf plotted against Pt/Hf. Using a common denominator in the ratios (i.e., Al, Lu and Hf in this case) ‘straightens’ any mixing lines and eliminates the effect of magmatic processing. The geochemical ratios were calculated for each sample of the LST (Table 5.3) to represent all the LST units.

The values were normalised to chondrite values from McDonough and Sun (1995) to allow comparison between extraterrestrial and terrestrial materials. Chondrites are thought to represent the best mean estimates of non-volatile elements in the primitive solar system, prior to melting or alteration processes (White, 2013; Scott & Krot, 2014). By normalising to a standard, effects related to nuclear stability and nucleosynthesis are eliminated, smoothing the natural “saw-tooth pattern” characteristic of decreasing abundances caused by these factors and highlighting any significant anomalies (White, 2013).

5.3.2.1. Laacher See Tephra

Individual elemental ratio values were calculated using the LST geochemical data obtained for this report (Table 5.5). The ratios Hf/Lu, Pt/Lu, Hf/Al and Lu/Al show a decreasing trend in the mean values from the basal LLST to the top of the deposit. Whereas, the ratios Pt/Al and Pt/Hf demonstrate an increasing trend in mean values from the LLST to the MLST. Some Pt values were bdl (Section 5.3.1) and therefore no ratios are available (see Table 5.5). All Ir values were bdl and thus some ratios discussed above are not included for the LST data.

Table 5.5: Geochemical ratios for individual samples in the pumice samples of the LST.

	Elemental ratio					
Sample no.	**(Hf/Lu)N**	**(Pt/Al)N**	**(Pt/Hf)N**	**(Pt/Lu)N**	**(Hf/Al)N**	**(Lu/Al)N**
LST 001	7.82	2.95×10^{-6}	5.51×10^{-7}	4.31×10^{-6}	5.34	0.68
LST 002	8.07	-	-	2.30×10^{-7}	5.05	0.63
LST 003	7.12	-	-	2.32×10^{-7}	4.50	0.63
LST 004	6.43	-	-	4.43×10^{-7}	2.14	0.33
LST 005	6.25	-	-	4.43×10^{-7}	2.09	0.33
LST 006	5.74	-	-	5.18×10^{-7}	1.67	0.29
LST 007	5.19	-	-	6.96×10^{-7}	1.18	0.23
LST 007A	5.61	-	-	6.09×10^{-7}	1.40	0.25
LST 008	3.79	-	-	8.40×10^{-7}	0.76	0.20
“SAMPLE A” -LST003	7.51	-	-	2.49×10^{-7}	4.29	0.57
“SAMPLE B” -LST007	5.32	-	-	6.96×10^{-7}	1.17	0.22
“SAMPLE C” - LST005	6.57	1.49×10^{-6}	7.13×10^{-7}	4.68×10^{-6}	2.09	0.32

	Elemental ratio					
Sample no.	**(Hf/Lu)N**	**(Pt/Al)N**	**(Pt/Hf)N**	**(Pt/Lu)N**	**(Hf/Al)N**	**(Lu/Al)N**
"SAMPLE D" - LST008	3.78	-	-	7.86×10^{-7}	0.78	0.21
Mean LLST	7.63	2.95×10^{-6}	5.51×10^{-7}	1.26×10^{-6}	4.79	0.63
Average MLST	5.87	1.49×10^{-6}	7.13×10^{-7}	1.16×10^{-6}	1.68	0.28
Average ULST	3.78	-	-	8.13×10^{-7}	0.77	0.20
Average LST	6.09	2.22×10^{-6}	6.32×10^{-7}	1.13×10^{-6}	2.50	0.38

All values are to 2 d.p. N = chondrite normalised values using values from McDonough and Sun (1995). The ratios Ir/Hf, Ir/Lu and Ir/Al are excluded as all Ir values were bdl (see Table 5.3), and some Pt values were also bdl so ratios including these samples could not be calculated.

5.3.3. Comparison to Literature Values

The LST values (pumice only) for the ratios discussed in Section 5.3.2 were compared to the Petaev et al. (2013) GISP2 spike and literature values for different types of rocks obtained from published articles and online databases (see Fig. 5.4). The data included specific volcanic deposits, sorted into ultramafic, mafic, intermediate and felsic volcanics, and meteorites sorted into chondrites, achondrites, Martian and iron classes. The values generally plot within discrete fields (e.g., 'volcanics', 'meteors', etc.), which facilitate intercomparison.

5.3.3.1. Laacher See Tephra

A majority of the LST samples did not plot in the volcanic field (Fig. 5.4), although with the ratios Hf/Al against Pt/Al (Figure 5.4c) and Ir/Al against Pt/Al (Figure 5.4a) there is some overlap between the LST and volcanic fields (particularly mafic or intermediate volcanics). Most of the LST sample ratios are low in respect to other plotted values - two orders of magnitude smaller (~10^2) than literature volcanic values – perhaps because of the LSE's unusual composition (see Chapters 2 and 3). Furthermore, the LST does not plot close to the GISP2 spike identified by Petaev et al. (2013).

5.3.3.2. GISP2 Spike

The geochemical excursion within the GISP2 ice core does not plot close to the meteorite, volcanic or LST fields in a majority of the elemental ratios: Hf/Al, Lu/Al and Ir/Al against Pt/Al, Ir/Lu against Pt/Lu and Ir/Hf against Pt/Hf (Figures 5.4a-d, f). For ratios involving Ir, the GISP2 spike plots closest to the meteorite field, although GISP2 values are orders of magnitude larger than any of the literature meteorite values (at least ~10x, with some values ~100x), which demonstrates the unusually high Pt concentrations of the ice samples compared to Ir, Hf and Lu. The exception is Hf/Lu against Pt/Lu, where the GISP2 spike plots very close to the meteorite field, and particularly close to an iron meteorite value (Fig. 5.4e). Ratios including Ir have a strong correlation in literature meteorite and volcanic values, however the GISP2 spike and a majority of LST values do not plot along the same line (Figures 5.4a and 5.4d). These results are relatively incompatible with conclusions drawn by Petaev et al. (2013), who suggested an iron meteorite as the GISP2 Pt spike source.

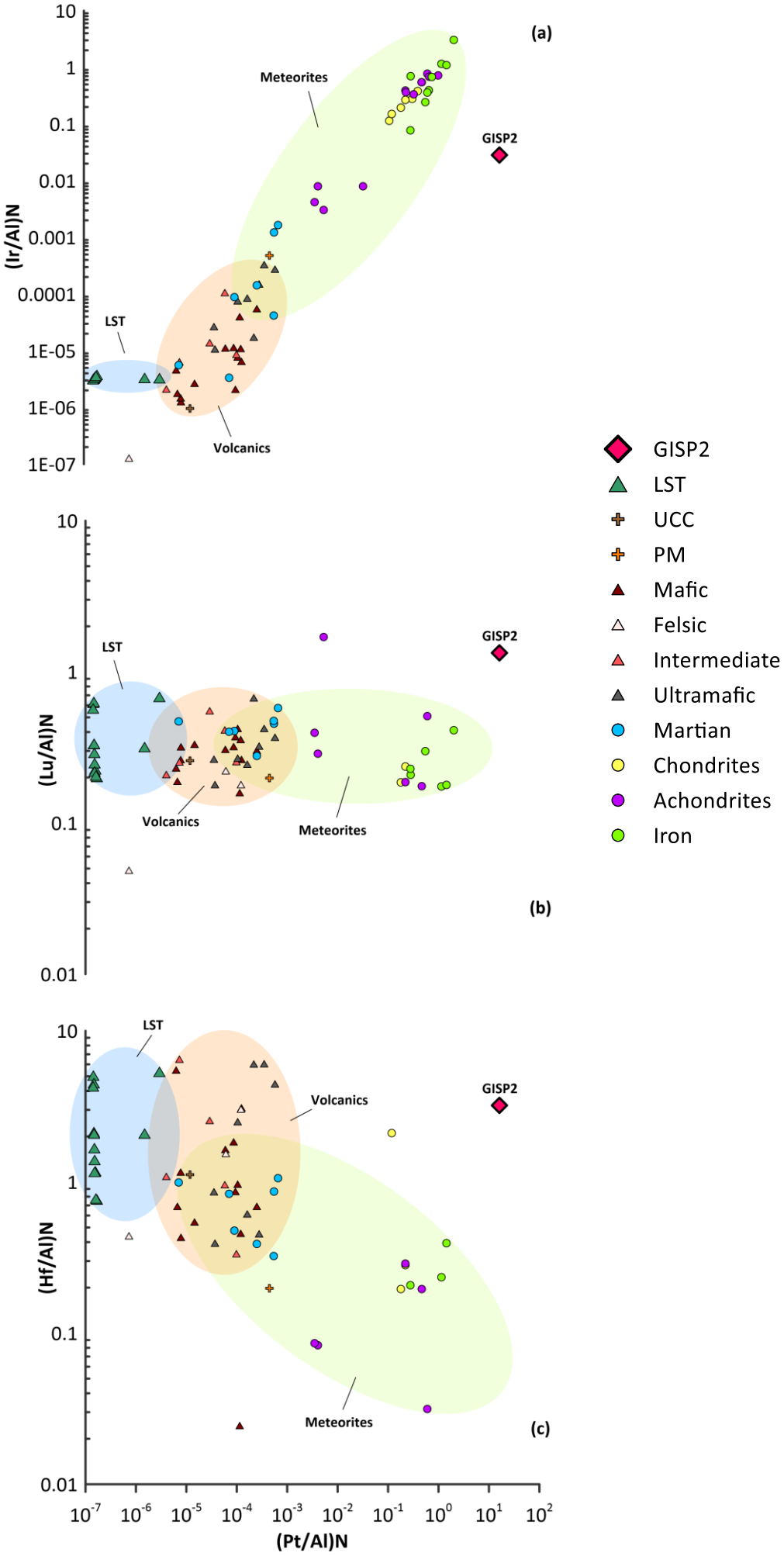
(a)
Meteorites
GISP2
LST
Volcanics
(Ir/Al)N
10
1
0.1
0.01
0.001
0.0001
1E-05
1E-06
1E-07
(b)
LST
GISP2
Volcanics
Meteorites
(Lu/Al)N
10
1
0.1
0.01
(c)
LST
Volcanics
GISP2
Meteorites
(Hf/Al)N
10
1
0.1
0.01
10^{-7} 10^{-6} 10^{-5} 10^{-4} 10^{-3} 10^{-2} 10^{-1} 10^{0} 10^{1} 10^{2}
(Pt/Al)N
GISP2
LST
UCC
PM
Mafic
Felsic
Intermediate
Ultramafic
Martian
Chondrites
Achondrites
Iron

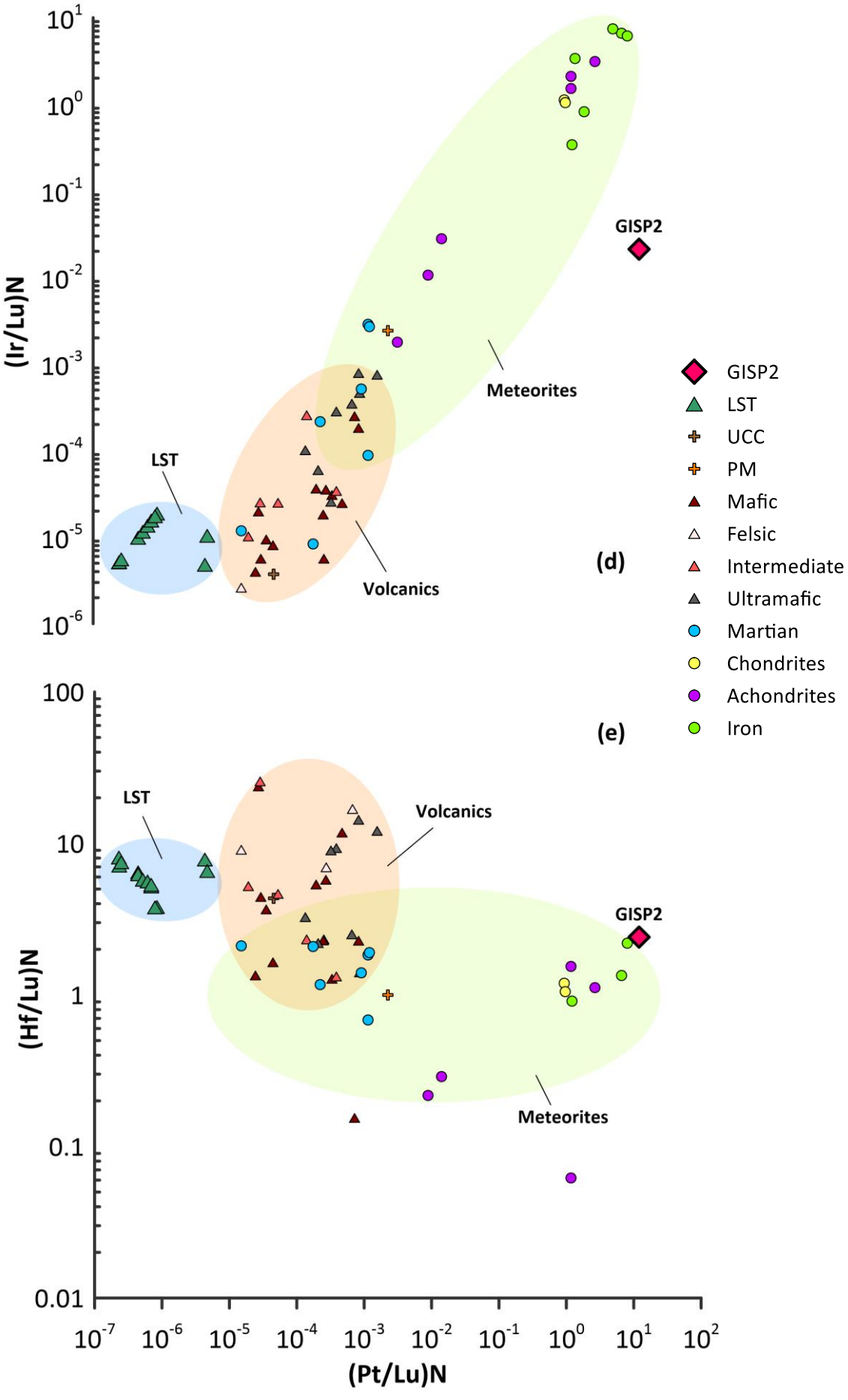
(Ir/Lu)N
(Hf/Lu)N
(Pt/Lu)N
(d)
(e)
LST
Volcanics
Meteorites
GISP2
UCC
PM
Mafic
Felsic
Intermediate
Ultramafic
Martian
Chondrites
Achondrites
Iron

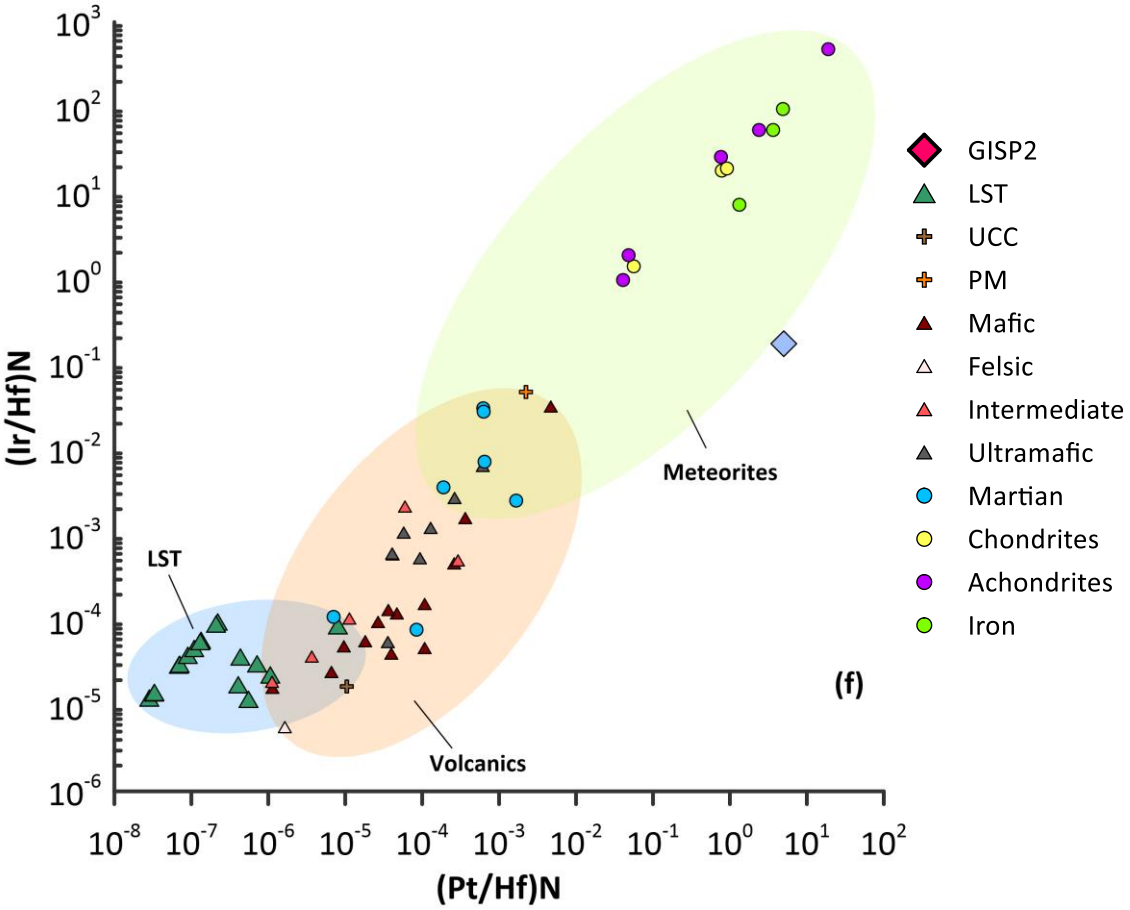

Figure 5.4: Element ratios (a) Ir/Al plotted against Pt/Al; (b) Lu/Al against Pt/Al; (c) Hf/Al against Pt/Al; (d) Ir/Lu against Pt/Lu; (e) Hf/Lu against Pt/Lu and (f) Ir/Hf against Pt/Hf. Triangles represent volcanics, and circles represent meteorites. The LST values shown are the maximum possible values (any values bdl have been set as the laboratory detection limit for the purpose of the graph). All values are normalised to C1 chondrite. Abbreviations: GISP2 = GISP2 Pt spike; LST = Laacher See Tephra; UCC = Upper Continental Crust; PM = Primitive mantle. The data was obtained from the following databases: Geochemical Earth Reference Model (GERM, 2019), Geochemistry of Rocks of the Oceans and Continents (GeoRoc, 2019) and the Meteorite Information Database (MetBase, 2019).

6. Discussion

As discussed in Chapter 2, the origin of the Pt spike in the GISP2 ice core identified by Petaev et al. (2013) is unclear, and more importantly, its hypothesised connection to the Younger Dryas equivocal. The following possible sources of the Pt spike are discussed further in this chapter:

- the LSE at 12.880±0.40 ka BP
- a different, Pt-rich volcanic eruption occurring at a similar time
- a meteorite impact or airburst
- volcanic exhalations and hydrothermal fluids
- seawater
- possible anthropogenic contamination of the ice core sections
- the Pt 'nugget' effect

The subsequent sections discuss two factors of the Pt spike that may provide a link to the sources listed above and potentially the YD – the Pt spike timing within the ice core and the Pt spike geochemistry (also utilising other measured elements in the same ice section). Importantly, atmospheric or post-depositional processes may alter depositional timing and the original geochemistry of the source.

Mechanisms of Pt enrichment in the melt and volcanic aerosol are introduced to explain the LST geochemistry and why it is a possible source.

6.1. Timing of the Pt Spike and the LSE

The results in Chapter 5 demonstrate that the GISP2 Pt spike's age (on the GICC05modelext chronology) of 12.822 ka BP does not coincide with the GISP2 volcanogenic sulfate spike at 12.867 ka BP attributed to the LSE (Baldini et al., 2018). The Pt spike occurs ~60 years after the eruption itself, dated at 12.880±0.40 ka BP by MFM lake varves (Lane et al., 2015), and ~50 years after the interpreted GISP2 LSE sulfur spike. It is necessary to examine potential reasons for the chronological offset between the Pt spike and the LSE; in other words, if there are any factors that could have delayed the deposition of Pt into the GISP2 ice core for ~60 years following the LSE.

6.1.1. Atmospheric Dynamics

Volcanic sulfate aerosols usually persist in the atmosphere for ~1-3 years (Robock and Mao, 1995; Robock, 2000; Baldini et al., 2018); for example, aerosols

released during the AD 1991 Mt Pinatubo and AD 1980 Mt St Helens' eruptions resided in the atmosphere for 3 years (Pitari et al., 2016; Diallo et al., 2017). Both eruptions injected considerably less SO_2 into the atmosphere than the LSE, ~20 Mt (Baldini et al., 2018) and ~2.1 Mt SO_2 respectively (Pitari et al., 2016), compared with the LSE's ~83 Mt (Baldini et al., 2018) so the LSE's sulfate aerosol could have resided longer (see Section 2.2.3.3). Moreover, the highest concentration of sulfur six months after the eruption was located over NH high latitudes, particularly Greenland (Fig. 6.1), and the restriction of the LSE aerosol to the NH could allow the sulfate aerosol cloud to linger over Greenland for longer (Pinto et al., 1989).

Several interactions govern the removal of volcanogenic aerosol burden on the atmosphere, such as particle loss from the stratosphere to the troposphere where wet scavenging promotes aerosol particle washout during precipitation (Pitari et al., 2016). Moreover, the particularly dry conditions of the YD (Mayewski et al., 1994; see Section 2.1) perhaps prolonged the residence time of the remaining LSE aerosol particles after NH climate shifted towards YD conditions. The height of the LSE's Plinian plume (>20 km; Harms and Schmincke, 2000) allowed for injection of sulfate aerosol directly into the stratosphere, thus increasing its overall residence time in the atmosphere (Pitari et al., 2016). The shear of equatorial zonal winds may also impact aerosol residence time (Pitari et al., 2016); with a frequently varying, complex ocean-atmospheric interaction characteristic of the stadial-interstadial cycles, this seems plausible.

On the other hand, the aerosol of the ~73 ka BP super-eruption of Toba (VEI 8) persisted for potentially ~6-10 years (Zielinski et al., 1996; Robock et al., 2009; Timmreck et al., 2012), despite injecting 100-300 times the SO_2 of Mt Pinatubo into the atmosphere. Ash aggregation during large volcanic eruptions can limit residence time of finer particles by impacting aerodynamic response (Costa et al., 2010; Folch et al., 2010). Furthermore, most of the aerosol veil fallout occurs within the first year of aerosol advection (Oppenheimer, 2003), and Pt is a heavy metal expected to fallout first. Atmospheric processing impacts aerosol residence time (Pitari et al., 2016), however, there is no definitive evidence to suggest the magnitude of the eruption, amount of SO_2 injection or geographical distribution of the aerosol would allow volcanogenic aerosol to persist in the atmosphere for longer than the average residence time of 1~3 years (Robock and Mao, 1995; Robock, 2000; Baldini et al., 2018), and thus these factors do not explain the ~60-year delay between the LSE and deposition into the GISP2 ice core record.

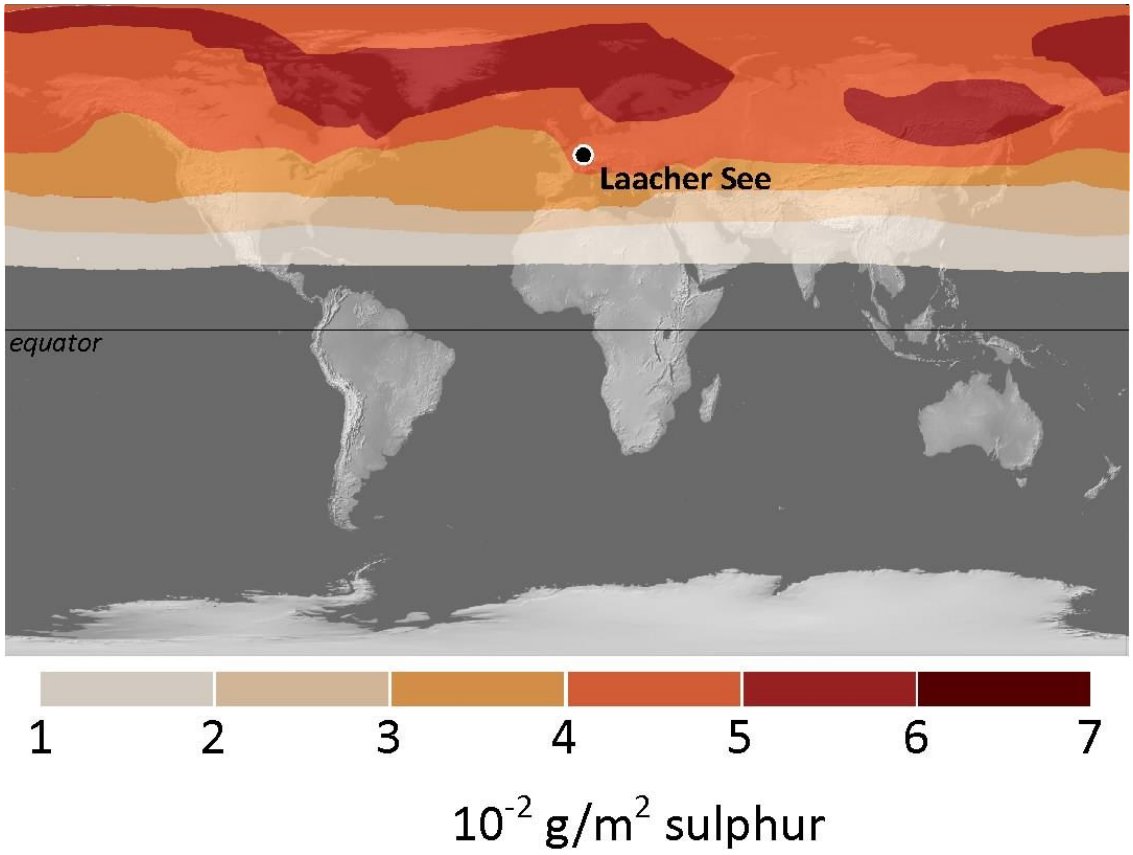

Figure 6.1: Distribution of the LSE volcanic aerosol six months following the eruption (12.880 ka BP), based on 15 Mt SO2 injection (Baldini et al., 2018; modified from Graf and Timmreck, 2001). Further details on the model and simulation are available in Graf and Timmreck (2001).

6.1.2. Post-depositional Processes

Although atmospheric input largely controls variability in particulate concentration, air-snow transfer and post-depositional modification may act to distort or filter the atmospheric signal of volcanic aerosol fallout prior to preservation in the ice core (Bales et al., 1992). Not only does precipitation (i.e. snowfall) deliver aerosol particulates to the ice core record, but particulate matter deposited by dry deposition – the removal of atmospheric pollutants through mass delivery to natural surfaces in the absence of precipitation – also contributes (Mohan, 2015). Snow deposition is the primary process in central Greenland in modern times, but deposition of aerosols by fog and dry deposition also play a significant role (Legrand & Mayewski, 1997). Low snow accumulation can result in surface roughness variability, generated by a combination of later snow accumulation, wind erosion and snow drift, and may cause local scale variability in particulate concentrations (Gabrielli and Vallelonga, 2015; Gautier et al., 2016) – problematic when only one ice core is considered. GISP2 accumulation rates were on average 0.07±0.01 m

ice/year during the YD (Alley, 2000), suggesting that dry deposition may have dominated as the remaining aerosol particles settled. Further large-scale variations in volcanic sulfate deposition are highlighted in various works (e.g. Gao et al., 2007), which emphasises the requirement for cross-correlation of anomalies between multiple ice cores.

Other factors impacting aerosol air-snow transfer of aerosol species include: i) reversible deposition (i.e. aerosol species re-enter the atmosphere), ii) chemical changes within the snow and iii) mobilisation within the snow (Alley, 2000). Interstitial air (within the porous snow and firn) exchanges with the above atmosphere, so air within ice bubbles is always younger than the surrounding ice (Goujon et al., 2003). Gas age-ice age differences (Δage) and close-off depth (firn to bubbly ice transition) are fairly well constrained in central Greenland (see Goujon et al., 2003), but do not take into account complex post-depositional processes that may alter snow chemistry before close-off depth is achieved. Furthermore, close-off depth is impacted by meteorological properties such as precipitation processes, wind flow velocity, solar radiation, surface air temperature and temperature gradient, which can also cause thermal fractionation of some gases (Bender et al., 1997; Salamatin & Lipenkov, 2008). In the Greenland ice sheet, pore close-off density (830 kg m^{-3}) is achieved at ~60m and therefore air exchange, meltwater infiltration and refreezing events can affect the deep firn layer (Harper et al., 2012) which may lead to mobilisation of trace constituents, although this process is poorly studied.

Petaev et al. (2013) discovered no iridium (another PGE) in the age range investigated, suggesting high levels of PGE fractionation. Atmospheric processing may play a role in fractionating the aerosol's volatile species (sulfate) from less volatile species (trace constituents such as Pt), however on such long timescales seems unlikely. Chronological offset in ice cores exists between CO_2 and the surrounding ice (Δage) due to post-depositional processes (Goujon et al., 2003), but no data exists for post-depositional fractionation of the PGEs or Pt mobilisation in ice cores and no plausible mechanism to explain this is currently available. However, a sudden increase in Pt (in comparison to older ice, although not to the same concentrations as the Pt spike) is observed concurrently with the LSE sulfate spike, suggesting the eruption is a plausible source of Pt. Therefore, another eruption closer to ~12.822 ka BP could cause the Pt spike, independent of atmospheric processing and post-depositional processes. The role of atmospheric and post-depositional processing in a geochemical context is discussed further in Section 6.2.

6.1.3. Alternative Explanations

None of the processes discussed above provide a viable explanation for the chronological mismatch between the Pt spike age and the LSE. Consequently, it is likely that the LSE occurred several decades prior to the Pt spike, and an alternative source was responsible for elevated Pt concentrations in the GISP2 core. The YDIH suggests a meteorite or airburst impacted the Laurentide ice sheet, with evidence including impact “markers” discovered in YDB sediments ~12.9 ka (e.g. Firestone et al., 2007; see Section 2.2.2 of this report). The age of the impact marker-rich YDB sediments is assumed fairly contemporaneous with the 12.822 ka BP Pt spike (Wolbach et al., 2018a), which indicates a possible extraterrestrial origin of platinum (Section 6.2).

Most YDIH sites were radiocarbon dated with reference to a carbon-rich black layer (“black mat”) formerly identified and cross-correlated at >50 North American study sites (Haynes, 2005; Firestone et al., 2007). Firestone et al. (2007) calculated the average age of all calibrated sites as 12.938± 0.25 ka BP, and in a later study, Wolbach et al. (2018b) use Bayesian analysis on the age of YDB events (i.e. bolide impact proxies, biomass burning proxies) across multiple climate records, calculating an age of 12.854±0.056 ka BP. Both ages are approximately coeval to the Pt spike, but a ~30-100 year offset remains. The ages in the latter study (within the ~95% confidence interval) range from ~12.77ka BP to ~12.98 ka BP (Wolbach et al., 2018b), which encompasses the 12.822 ka BP Pt spike. Moreover, a notable issue with the YDIH is a lack of chronological control between YDB study sites (Meltzer et al., 2014). Out of 29 prominent YDB sites (as of 2014), only three are considered to offer support to the YDIH, and problems include: i) no form of age control, ii) chronologically unrelated radiometric ages, iii) age-depth correlation issues and iv) a younger or older impact layer than ~12.9 ka (Meltzer et al., 2014). Therefore, it is difficult to link the YDIH meteorite impact or airburst to the Pt spike. However, the YDIH is discussed alongside the Pt spike in recent work (e.g. Wolbach et al., 2018a) and thus an attempt is made below to explain the chronological offset (~30-100 years) between the average age of impact marker-rich YDB sediments and the GISP2 Pt spike.

Like a volcanic aerosol, a meteorite impact or airburst could create a sulfate aerosol generated by sulfates contained within impacting bolides (Toon et al., 1997; Firestone et al., 2007). Atmospheric dust loading can also occur following impact,

carrying elements from the disturbed surface and the meteorite itself (Toon et al., 1997; Firestone et al., 2007). Dry deposition as the dust settles from the atmosphere or wet deposition as dust particles mix with rainwater and fall as precipitation can transport contaminants to the Earth's surface (Ponette-González et al., 2018) and could cause a slight delay in Pt deposition. Furthermore, atmospheric processing may affect the impact-induced sulfate or dust clouds similar to its effect on volcanogenic aerosol (Section 6.1.1). However, the average residence time of sulfate aerosol is short (Section 6.1.1), and dust is lost from the atmosphere on a similar timescale (Toon et al., 1997). Although impact models, particularly related to the Cretaceous-Paleogene boundary (~66 Ma), suggest a large meteorite impact can produce significant amounts of dust and aerosol (e.g. Pope, 1997), modern analogues of large bolide impact or airbursts (comparable to the YDIH) on Earth are unavailable, so there is considerable uncertainty on aerosol and dust generation. Poor dating accuracy of YDB sediments adds a layer of unreliability to the link between the GISP2 Pt spike and the YDIH suggested by some YDIH advocates (e.g. Wolbach et al., 2018a). Similar to volcanogenic aerosol from the LSE, the above processes are unable to provide a viable explanation for a ~30-100 year offset between YDB sediments and the GISP2 Pt spike.

Alternatively, if the GISP2 Pt spike is isolated as a local anomaly in contrast to the most recent YDIH work (Wolbach et al., 2018a), another, perhaps noncataclysmic meteorite impact event could explain the GISP2 Pt anomaly. The Cape York iron meteorite impacted Greenland, and a terrestrial age contemporaneous with the Pt spike is not ruled out, making it a possible origin of Pt (Boslough, 2013). However, Cape York is included in iron meteorite data in this report (Fig. 5.4a-f) and the geochemistry does not match the GISP2 Pt spike geochemistry (which is discussed further below).

6.2. Geochemistry

The geochemistry of the Pt spike is unusual. Petaev et al. (2013) highlighted that the high Pt/Ir and Pt/Al ratios at the Pt peak are dissimilar to known terrestrial or extraterrestrial materials. Further work in this study also shows the GISP2 Pt spike geochemistry is unlike the LST and other common meteorites and magmas studied in the literature (Chapter 5; Fig. 5.4a-f). Furthermore, the GISP2 Pt peak geochemistry (specifically the Pt/Ir ratio) does not match (see Fig. 6.2): i) historic volcanogenic sources in snow and ice, ii) YDB sediments in North America and

Europe, iii) Cretaceous-Tertiary (or Cretaceous-Paleogene) boundary (KTB) sediments, iv) impact melt rocks in craters created by bolide impacts or iv) glaciofluvial sediments from the recently discovered Hiawatha Glacier crater (Kjær et al., 2018). The Pt/Ir and Pt/Al ratios of the GISP2 Pt spike are highly fractionated – a level of fractionation not observed in literature values (Fig. 6.2). Furthermore, aluminium (Al) is often used as an indicator of crustal dust and exists at background levels around the time of the Pt spike, before increasing into the YD due to increased windiness (Mayewski et al., 1994; Petaev et al., 2013). Therefore, the possible Pt spike sources highlighted earlier (Section 6.0) are discussed further with fractionation processes in mind, in an attempt to explain the unusual, highly fractionated geochemical signature.

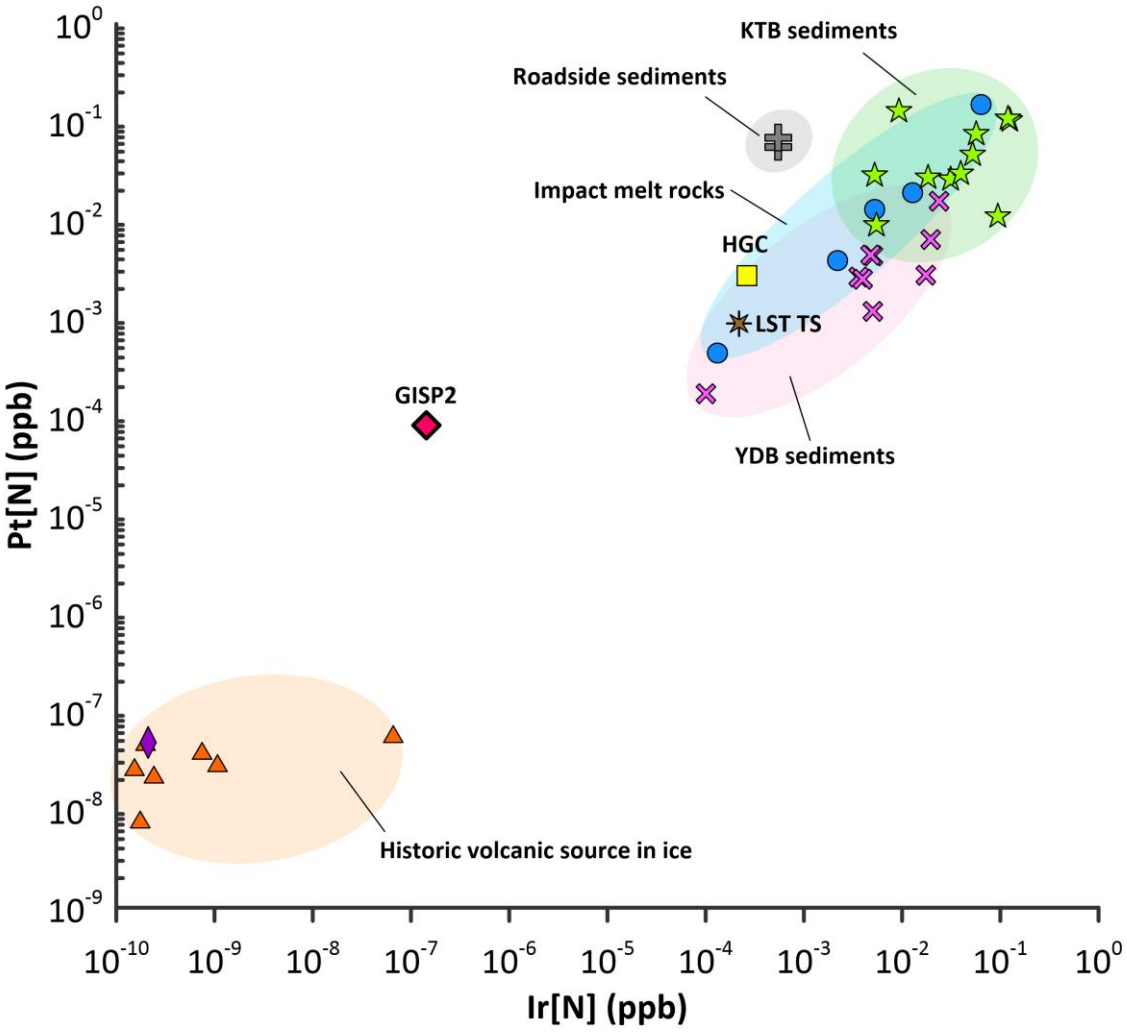

Figure 6.2: Pt (ppb) plotted against Ir (ppb) normalised [N] against CI chondrite (McDonough & Sun, 1995), showing Pt/Ir ratios of i) historic volcanic sources in ice, represented by triangles and the orange field (Soyol-Erdene et al., 2011; Gabrielli et al., 2008); ii) YDB sediments in North America and Europe, represented by crosses and the pink field (Firestone et al., 2007; Paquay et al., 2011; Andronikov et al., 2016; Moore et

al., 2017), iii) Cretaceous-Tertiary (Cretaceous-Paleogene) boundary (KTB) sediments, represented by stars and the green field (Evans et al., 1993b), iv) impact melt rocks in craters created by bolide impacts, represented by circles and the blue field (Evans et al., 1993a; Tagle et al., 2004), v) HGC (Hiawatha Glacier crater) glaciofluvial sediments represented by a yellow square (Kjær et al., 2018), vi) roadside sediments from the Manoa and Palolo urban watersheds, Hawaii (Sutherland et al., 2007), represented by grey crosses, vii) seawater represented by the purple diamond (Nozaki, 1997), viii) LST TS – Topsoil overlying the LST from locality LST1 (this study) and IX) GISP2 – the GISP2 Pt spike, represented by a red diamond (Petaev et al., 2013).

6.2.1. A Volcanic Source: Platinum-rich Volcanism

Volcanic-derived Pt is found in: i) Greenland ice cores (attributed to the 1991 eruptions of nearby Hekla volcano and potentially the more distal Mt Pinatubo) (Gabrielli et al., 2008), ii) Antarctic snow (credited to 20th century eruptions, most notably the 1991 Cerro Hudson eruption) (Soyol-Erdene et al., 2011) and iii) North American terrestrial deposits correlated to Laki (CE 1783-1784), Kuwae (CE 1452-1453), and Eldgjá (CE 934) (Tankersley et al., 2018). To understand a potential volcanic source of the GISP2 Pt spike discovered by Petaev et al. (2013), mechanisms of PGE enrichment in the volcanic system are discussed below.

6.2.1.1. PGE Enrichment in the Melt

The Platinum Group Elements (PGEs) are highly siderophile elements and exhibit a strong affinity for metals and sulfides (Lorand et al., 2008). Sulfur can exist in different species or valence states in a melt, determined by the magma oxidation state (Caroll & Rutherford, 1985). Oxidised conditions cause sulfur to dissolve as sulfate (S^{6+} in SO_4^{2-}), and in a reducing environment, sulfide (S^{2-}) – both are present in intermediate conditions (Edmonds & Mather, 2017). Sulfur species become concentrated in melts through crystallisation of non-sulfur bearing phases, ultimately reaching saturation and precipitating non-volatile, sulfur-bearing phases (Edmonds & Mather, 2017). In a sulfide-rich melt, PGEs preferentially form covalent bonds with sulfide ions over ionic bonds with oxygen ions in silicate melts (Mungall & Naldrett, 2008), thus becoming “trapped” in sulfide liquids or alloys (Lorand et al., 2008). PGEs demonstrate higher mobility in fluid-rich environments, with greater transport efficiency of the “platinum-PGEs” (Pt, Pd and Rh) relative to the “iridium-PGEs” (Ir, Ru, Os) (Rehkamper et al., 1997). When the denser (respective to silicate melts) sulfide liquid settles, it may separate out to form PGE ore deposits (Fig. 6.3). Alternatively, dependant on the timing of the eruption and sulfide liquid formation,

the sulfide melt inclusions are erupted with the magma as observed in deposits from Grímsvötn volcano, Iceland (Sigmarsson et al., 2013). On the other hand, the sulfide liquids may completely dissolve, liberating PGE into the magma (Mungall & Naldrett, 2008), so if the sulfide liquid was PGE-rich, the erupted rocks are probably PGE-rich. PGE liberation into the magma can also take place pre-magma ascent, where high degrees of melting stimulate PGEs (particularly platinum-PGEs) to dissolve into the silicate melt; most significant PGE deposits are formed in this way (Mungall & Naldrett, 2008).

Furthermore, the iridium-PGEs (and Rh) are mildly compatible (i.e. less soluble) in a silicate melt than Pd and Pt; Os-Ir alloys form which then settle out into a restite phase, leaving a Pd- and Pt-rich magma during crystal fractionation or partial melting processes (Barnes et al., 1985; Mungall & Naldrett, 2008). PGE concentration and fractionation in the melt is also dependent upon other factors such as alteration (Barnes et al., 1985). Therefore, the above factors suggest a Pt-rich, Ir-poor tephra is not implausible if PGEs are liberated into the melt with ideal timing, and this raises volcanism as an unlikely, but possible, source of the Pt-rich, Ir-poor geochemical spike observed in the GISP2 ice core (Petaev et al., 2013). However, the results of this study show the LST is Pt-poor (Chapter 5) and below the crustal abundance of 0.5 ppb (Tankersley et al., 2018) despite its sulfur-rich nature, suggesting that Pt was not concentrated within the erupted magma at the time of eruption.

6.2.1.2. PGE Enrichment in the Volcanic Aerosol

Despite the chronological lag of the Pt peak relative to the LSE, there is an initial Pt concentration increase associated with the Pt spike at 12.868 ka BP, contemporaneous with the LSE sulfate spike (Fig. 5.1). This observation suggests a possible link between the two. However, as discussed previously (Section 6.2.1.1), the LST is PGE-poor but sulfur-rich, which suggests either: i) the magma system conditions of the Laacher See were not suitable for PGE formation or ii) if PGEs were formed, pre- or syn- eruptive degassing of volatile gas phases could disperse the PGEs into the atmosphere (A Iveson, pers. comm., 19th July 2019). When sulfide solutions destabilise, sulfur and associated metals are transferred into the fluid phase (i.e. liberated into the melt or magmatic fluids); the result is sequestration or outgassing into the atmosphere in a volatile phase (Edmonds & Mather, 2017). The transport of sulfide and therefore trace metals toward the top of the magma chamber may also result from rising vapour bubbles carrying sulfide melt droplets in a sulfide-

melt saturated magma (Mungall et al., 2015), increasing the likelihood of trace species emission.

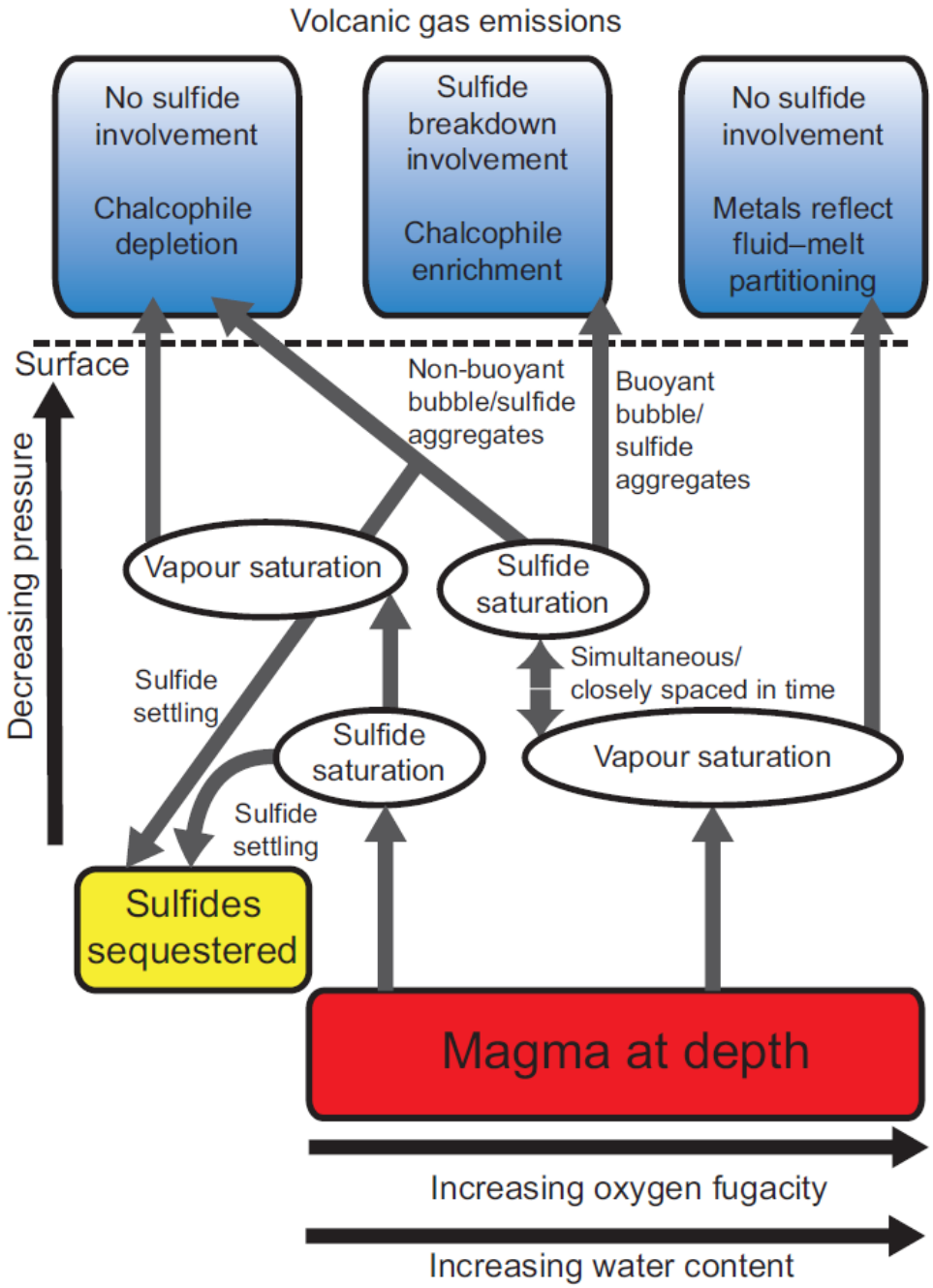

Figure 6.3: Schematic demonstrating the interaction of magmatic sulfides and exsolved aqueous fluids in melts through a variety of processes and their outputs (Edmonds & Mather, 2017).

A volcanic plume is a physical mixture of gases and solid phases, and metals are strongly partitioned to particulate phases (Hinckley 1991). For a metal to incorporate into the aerosol, it must undergo volatilisation during exsolution of major

volatile melt components, followed by conversion from gas to the particle phase (Aiuppa et al., 2003; Mather et al., 2003; 2012). The chemical composition of volcanic aerosol also comprises elements derived from conduit wall erosion processes (Aiuppa et al., 2003). To transport metals, chlorine (Cl), sulfur (S) and fluorine (F) behave as ligands and are therefore crucial in the exsolving gas phase (Aiuppa et al., 2003), as most trace metals are transported in the solid phase (Hinkley, 1991). Once a sulfate aerosol is formed following oxidation of sulfur-rich gases in the plume (see Section 2.2.3.3), atmospheric circulation advects the aerosol around the globe. Platinum-aerosol layers can potentially form with the sulfate aerosol, as metals are exhumed with more volatile species, and particles ~0.1mm in diameter are widely distributed (Tankersley et al., 2018).

The Role of Halogens. Volcanic eruptions may release volcanogenic halogens alongside sulfate aerosol, and these are key in the degassing and transport of trace metal species (Crowe et al., 1987; Mather et al., 2003, 2012). For example, work on Kilauea (Hawaii) was key to understanding trace metal degassing and behaviour in the volcanic plume (e.g. Crowe et al., 1987; Hinkley, 1991; Mather et al., 2012). Pre- or syn-eruptive degassing of the Laacher See was possibly enriched in Cl but F-poor (Harms & Schmincke, 2000). Chlorine- and S-complexes both demonstrate the ability to carry Pt in volcanic systems (e.g. Symonds et al., 1992; Simon & Pettke, 2009), therefore, the Cl- and S-rich volcanic plume of the LSE could carry Pt as S- or Cl- complexes in the aerosol phase. Furthermore, H_2O was degassed with Cl during Plinian phases (Harms & Schmincke, 2000), which aids the mobility of trace metal-chlorine complexes by forming a hydration shell (A. Iveson, pers. comms., 19th July, 2019). The thermodynamics of the plume plays an important role, as condensation caused by falling temperatures will lead to fall out of most trace constituents perhaps before they can travel considerable distances, and thermodynamic processes also promote considerable fractionation of different trace constituents (Crowe et al., 1987).

Chlorine concentrations in the GISP2 ice core begin to increase toward YD values around ~12.85 ka BP, with a noticeable spike at ~12.84 ka BP of 72 ppb (Mayewski et al., 1994) – almost contemporaneous with the Pt spike and shortly after the LSE sulfate spike (Fig. 6.4). A sudden, smaller increase in Pt and Cl concentrations compared to older ice occur almost simultaneously with the LSE sulfur spike (Fig. 6.4). A Cl peak in the GISP2 ice core likely resulted from the LSE's volcanogenic aerosol deposition, which may in turn have deposited some Pt onto the ice sheet.

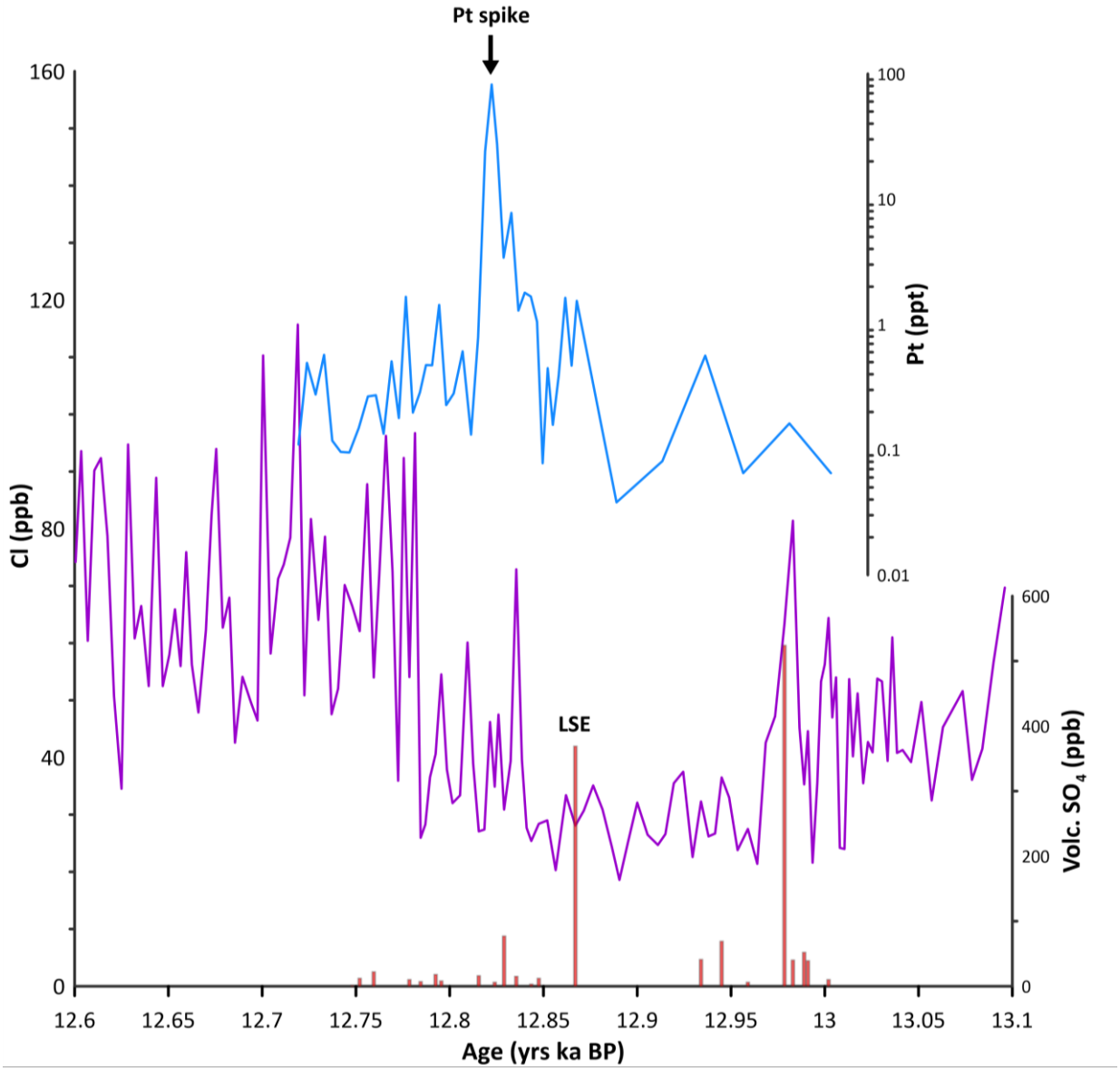

Figure 6.4: The purple line represents chlorine (Cl) and the red bars represent volcanogenic sulfate (Volc. SO_4) in ppb (Mayewski et al., 1994), and the blue line represents platinum (Pt) in ppt (Petaev et al., 2013). All concentrations are measured in the GISP2 ice core between the ages 12.60 ka BP to 13.10 ka BP.

In short, perhaps the Laacher See magma became oversaturated with respect to sulfide, forming sulfide liquid which then formed buoyant aggregates that carried sulfide and metals to the top of the magma chamber. The platinum-PGEs could have already fractionated from the less soluble iridium-PGEs at this point (Section 6.2.1.1). These aggregates then dissolve at the time of eruption, liberating metals into a fluid phase and very-late stage degassing delivers significant sulfur and trace metals into the atmosphere. However, vapour saturation would essentially need to happen before or simultaneously with sulfide saturation (Edmonds & Mather, 2017) to create the hypothetical scenario described above. Despite the

"ideal" geochemical conditions of the LSE (i.e. S-, Cl- and H_2O-rich in Plinian phases), there are other factors controlling volatile phases and the mobility of metals including (but not limited to) pressure, temperature and oxygen fugacity (Aiuppa et al., 2009). Therefore, despite the Pt-poor nature of the LST, the LSE could have contributed small amounts of Pt to the Greenland Ice Sheet through syn-eruptive degassing of Pt, which is then carried in complexes with the aerosol and deposited onto the ice sheet. This is represented by a sudden increase in Pt coinciding with the LSE sulfate spike. However, despite the possibility of the LSE causing a small Pt spike, it is unlikely that the LSE's volcanogenic aerosol persisted in the atmosphere for ~60 years after the eruption to cause the definitive GISP2 Pt spike.

6.2.1.3. Chemical and Atmospheric Processing in the Volcanic Cloud

During explosive eruptions, it takes approximately ten minutes for the volcanic plume to reach the stratosphere, therefore limiting chemical transformations in the eruption cloud (plume) before this point (Textor et al., 2003; Langmann, 2014). Upon reaching the stratosphere, SO_2 and H_2S react with hydroxide (OH) and are oxidised to form sulfuric acid within days to weeks (Robock, 2000; Langmann, 2014). Binary homogenous nucleation of sulphuric acid vapour and water vapour leads to the creation of new particles, thus converting sulfuric acid vapour to sulfate aerosol (Langmann, 2014). The CE 1991 Mt Pinatubo eruption is notable as the first opportunity during the instrumental era to study the interactions within a large volcanic plume as well as atmosphere-aerosol interactions. Volcanogenic sulfate aerosol from the 1991 Mt Pinatubo eruption reached peak stratospheric concentrations around three months following the eruption (Russell et al., 1996; Langmann, 2014).

In the presence of volcanic ash, large particles are subject to fast sedimentation, which restricts interaction between ash and volcanic gases (Langmann, 2014). However, sedimentation rates of smaller particles are slower and thus smaller particles persist in the lower stratosphere, as observed following the 1991 Mt Pinatubo eruption (Russell et al., 1996). Submicron ash particles in the lower stratospheric volcanic cloud aid condensation of volcanic gases, thus promoting growth of the aerosol layer (Langmann, 2014). Microphysical processes acting in the volcanic aerosol cloud are potentially self-limiting (Pinto et al., 1989 and references therein). A higher concentration of sulfate aerosol results in higher collision rates, which creates a higher distribution of larger aerosol particles, thus speeding up particle fallout and reducing aerosol residence time (Pinto et al., 1989).

Aerosol particles also impact stratospheric photochemistry – the absorption of radiation by particle surfaces and subsequent local heating can impact trace element abundance in the aerosol because reaction rate coefficients are dependent upon temperature (Pinto et al., 1989). Following the 1991 Mt Pinatubo eruption, atmospheric dynamic response to local heating also impacted aerosol dispersal (Timmreck & Graf, 2004).

The above chemical and atmospheric processes could result in fractionation of Pt from Ir. However, the refractory siderophile nature of all the PGEs (Lorand et al., 2008; Petaev & Jacobsen, 2004) should inhibit fractionation to the extent implied by the GISP2 Pt spike geochemistry. Furthermore, volcanic fallout of Holocene eruptions in snow and ice do not show the same correlation between the two elements (Fig. 6.2). Enhanced sulfur loading may also act to limit the number of aerosol particles and increase fallout speed of particles, thus reducing the residence time of the LSE aerosol and making it difficult to explain the time lag between the eruption and the GISP2 Pt spike. A shorter residence time is consistent with modelling by Graf and Timmreck (2001), although a much smaller estimate of sulfur loading (15 Mt) was used for the simulations. A smaller Pt/Ir ratio (~30) is observed at the two smaller Pt peaks contemporaneous with the LSE sulfate spike, which seems possible considering processes operating in the melt, aerosol and atmosphere.

6.2.1.4. Other Volcanic Eruptions

In summary, the LSE is unlikely the origin of the GISP2 Pt spike due to timing discrepancies and extreme geochemical fractionation of Pt, but a different volcanic eruption could have caused the GISP2 Pt spike. For example, a small sulfate peak (~80 ppb) is present in the GISP2 ice core at 12.829 ka BP (Fig. 5.1) – contemporaneous with the Pt peak. A smaller, local Icelandic volcano such as Hekla or Lake Torfadalsvatn could have caused the sulfate spike, carrying Pt within the aerosol. A sulfate peak at 13.03 ka BP was attributed to the proximal Hekla eruption (Muschitello et al., 2017), which also has a well-defined tephra layer along with the 12.646 ±65 ka BP Lake Torfadalsvatn eruption (Mortensen et al., 2005; Abbott & Davies, 2012). Eruptions of other Icelandic volcanoes, Laki (CE 1783-1784) and Eldgjá (CE 934), contributed to elevated Pt concentrations in North American sediments (Tankersley et al., 2018). Quiescent degassing from local volcanoes may also take place, however this would likely result in multiple Pt spikes in the ice. Alternatively, the geochemical sulfate anomalies could result from a larger, distal

eruption such as Nevado de Toluca, Mexico that occurred at 12.45±0.35 ka BP (Baldini et al., 2018), but it is unclear if this could also explain the GISP2 Pt spike. In short, another volcanic eruption as the source of the GISP2 Pt spike is plausible, but the unusual chemistry and extreme fractionation suggests that this possibility is unlikely.

6.2.2. An Extraterrestrial Source: Platinum-rich Meteorites

Meteorites are enriched in platinum (Anders & Grevasse, 1989; Sawlowicz, 1993; McDonough & Sun, 1995; Andronikov et al., 2014, 2015, 2016) in comparison to the continental crust (Wedepohl, 1995), and therefore, they represent a potential origin of the GISP2 Pt spike (Petaev et al., 2013). Iron meteorites are core fragments of parent planets formed in the early solar system and are often PGE-rich as a result of proto-planetary and late accretion processes (e.g. Buchwald, 1975; Crocket, 1972; Wasson, 1999, Wasson et al., 2007; Petaev & Jacobsen, 2004). The YDIH highlighted the Ir-rich nature of meteorites (e.g. Firestone et al., 2007; Moore et al., 2017) however a number of iron meteorites (particularly within class IIAB and IIIAB) are Ir-poor and Pt-rich (e.g. Wasson, 1999; Wasson et al., 2007) due to the poorly understood, complex nature of metal-silicate fractionation and core crystallisation in parent bodies (Petaev & Jacobsen, 2004). For example, the kamacite (Fe-Ni alloy) meteorite Sikhote-Alin demonstrates Ir-depletion and Pt-enrichment (Petaev & Jacobsen, 2004), but not to the extent of the extreme fractionation observed in the GISP2 ice core. Limited data are available on Al concentrations in iron meteorites, and thus it is difficult to find an extraterrestrial source with high Pt/Ir and Pt/Al ratios (Fig. 5.4a-f; Fig. 6.2). Petaev et al. (2013) hypothesised an iron meteorite with similar composition to Sikhote-Alin and a diameter of ~0.8km could produce the Pt distribution and geochemical ratios akin to the GISP2 Pt spike. YDB Pt concentrations may also result from amalgamation of meteorite material and the terrestrial rocks following impact (Sawlowicz, 1993; Wolbach et al., 2018a, 2018b). Aside from perhaps the newly discovered Hiawatha glacier crater, of which the age is poorly constrained (Kjær et al., 2018), there is no typical impact crater found at the YDB. Therefore, similar to volcanic eruptions, fractionation processes may act to produce the unusual geochemistry of the GISP2 Pt spike.

6.2.2.1. Primary Fractionation Processes in Meteorites

Condensation Fractionation. Meteorite impact would produce an ejecta cloud, with the highest temperatures located close to the impact site (Melosh, 1982).

Iridium and Pt have vaporisation temperatures of ~4500°C, and ~3800°C respectively (Hampson & Walker, 1961). Iridium would condense first, forming condensates with low Pt/Ir ratios, and later cloud expansion and cooling would lead to condensates with higher Pt/Ir ratios (Evans et al., 1993b). However, higher Pt/Ir ratios would likely exist at greater distances from the impact site, so if the Hiawatha glacier crater is assumed as the impact site, the GISP2 Pt spike geochemistry does not fit the model (Evans et al., 1993b). Without a definitive impact site, it is difficult to test whether condensation fractionation can explain the GISP2 Pt spike.

Oxidation Fractionation. Selective oxidation and thus fractionation of certain elements is possible. However there is poor understanding of important factors such as the PGE phase (whether PGEs are present as metals, oxides, ions or complexes) and their behaviour in the hot ejecta cloud, thermodynamic factors within the cloud such as temperature (T) gradient, relationship between T, O_2 availability and altitude of the cloud (Evans et al., 1993b). Modelling of large bolide impacts demonstrates how a non-permanent cavity in the atmosphere is created, through which impact material is rapidly introduced to a vacuum and quenched (Koeberl, 1986; Evans et al., 1993b), and debris is distributed over a wide area upon re-entry to Earth (Melosh, 1982; Koeberl, 1986). However, a lack of O_2 availability or condensation of the PGE-rich phase may occur prior to oxygen fugacity affecting fractionation of the PGEs (Evans et al., 1993a).

An Alternative Meteorite. The above primary fractionation processes are possible but theoretical (based upon modelling simulations) as no modern analogue of a large meteorite-generated ejecta cloud exists. Other factors, such as the GISP2 Pt spike's unusual geochemical ratios dissimilar to known meteorites and the chronological offset between YDB sediments and the GISP2 Pt spike, complicate linking the hypothesised YDIH impactor as the origin of the Pt anomaly. It would therefore seem that the YDIH requires two meteorite impacts: one for the Pt spike and one for the YD trigger. The noncataclysmic entry of the Cape York meteorite is already proposed as a potential Pt source, however its Pt/Ir ratio is not akin to the GISP2 Pt spike (Boslough, 2013). Like all meteorites discovered on Earth, there is no detail on the heterogeneity of the pre-entry body, and no data on fractionation processes discussed above (and others including ablation and precipitation) (Boslough, 2013), thus a link between the Pt spike and the Cape York meteorite is elusive.

6.2.3. Other Fractionation Processes

6.2.3.1. Alteration or Mobilisation in Snow or Ice

Some metals are prone to slow weathering during burial in snow or ice, or more rapid alteration when exposed on the ice exterior, for example there is evidence of Rare Earth Element (REE) mobilisation of meteorites in Antarctic ice (Floss & Crozaz, 1991). The iridium-PGEs, particularly Ir and Ru, are fairly inert and resistant to alteration or mobilisation by weathering (McCallum et al., 1976), but the platinum-PGEs are more mobile and so Pt could fractionate into secondary and heterogeneously dispersed carrier phases, resulting in Pt/Ir fractionation (Evans et al., 1993b).

The behaviour of PGEs during weathering is better researched in sediments, but still fairly poorly understood (e.g. Sawlowicz, 1993; Martín-Peinado & Rodríguez-Tovar, 2010; Moore et al., 2017). However, some natural processes such as “oxidation, hydration, effect of sulfuric acid generated by weathering of sulfides, effect of saline brines, presence of lower oxidation state oxyanions of sulfur and attack by organic acids” affect weathering of the PGEs and thus may contribute to the mobilisation of the elements post-deposition (Sawlowicz, 1993 pg 259 and references therein) in the snow and ice medium as well. A variable climate at the time of the Pt anomaly could lead to creation of ice ‘lenses” through exposure to higher summer temperatures igniting a process of thawing, percolation and solidification (Gabrielli et al., 2012; Gabrielli and Vallelonga, 2015). The influx of meltwater into the ice may affect concentrations of certain ionic species (particularly sulfate) in the natural firn layer (Eichler et al., 2001). Chlorine and fluoride also show depleted concentrations in upper firn layers at Vostok, Antarctica, suggesting that the compounds are partly discharged back into the atmosphere following deposition onto the ice surface (Wagnon et al., 1999; Eichler et al., 2001). If Pt was transported in a Cl-complex (for example), perhaps partial Pt liberation back into the atmosphere could occur, leading to elemental fractionation or later deposition. Furthermore, pressure melting point changes amplify the above mechanisms when the climate transitions into a temperate state (Gabrielli et al., 2012). However, these processes primarily impact sensitive alpine glaciers more than the remote centre of polar ice sheets, so the extent of disturbance on trace constituents at the GISP2 site is unclear (Gabrielli & Vallelonga, 2015). Little is known on PGE behaviour in the snow layer or ice column and thus it is difficult to determine whether processes within this medium could alter PGE concentrations after deposition, although it does present perhaps the simplest explanation for PGE fractionation.

6.3. Alternative Sources of Platinum

6.3.1. Volcanic Exhalations and Hydrothermal Fluids

Platinum and Pd are soluble at low to intermediate temperatures in comparison to the other PGEs, and therefore Cl, HS^- and OH^- complexes hosted in hydrothermal ore fluids can transport Pt and Pd (e.g. Mountain & Wood, 1988; Sawlowicz, 1993). Mid-ocean ridge settings show high levels of PGE-fractionation and enrichment in Pt, Pd and Au (Sawlowicz, 1993). For example, samples of sulfides and hematite-magnetite±pyrite±talc mounds in the Turtle Pits hydrothermal field have a Pt/Ir ratio of ~110 and a Pd/Ir ratio of ~130 (Pašava et al., 2007). Local exhalative activity could deposit Pt onto the Greenland Ice Sheet through degassing to the atmosphere and subsequent deposition, or perhaps erosion of hydrothermal condensates and increased windiness into the YD (Mayewski et al., 1994) distributed Pt to the ice sheet. However, the Pt/Ir ratio of the GISP2 Pt spike is ~570 which is approximately five times the values of Turtle Pits and therefore an exhalative hydrothermal source seems improbable.

6.3.2. Seawater

The influx of extraterrestrial or terrestrial material (and associated degradation products) would influence the chemical composition of seawater in the Pleistocene, as both are sources of PGEs either in dissolved or detrital phases (Sawlowicz, 1993). Element distribution in North Pacific seawater in the late 1990s had a Pt/Ir ratio of ~300-400 (Nozaki, 1997; Pašava et al., 2007), influenced by a combination of various sources including anthropogenic pollution. However, this demonstrates how sensitive seawater composition is to external influence. In Greenland ice, Cl and Na represent wind-blown sea salt, therefore concentration increase of these elements represents increased windiness (de Angelis et al., 1997; Mayewski et al.,1997; Wolbach et al., 2018a). A peak in Cl and Na around ~12.84 ka BP is observed in the GISP2 ice core, prior to general increased windiness in the YD (Mayewski et al., 1994; Wolbach et al., 2018a) and contemporaneous with the GISP2 Pt spike ~12.82 ka BP. If wind-blown sea salt is distributed to the Greenland Ice Sheet prior to PGEs precipitating out, then it could carry Pt to the remote ice sheet. This process may also lead to a lag of uncertain duration between the Pt source timing and the GISP2 Pt spike. However, Pt values in modern seawater (Nozaki, 1997) are orders of magnitude lower than at the GISP2 Pt spike (Fig. 6.2).

6.3.3. Contamination of the Ice

Platinum is a trace element in ice, and so for such a high concentration of Pt alongside low Ir concentrations presented by Petaev et al. (2013), contamination of the ice with Pt during drilling, sampling and analysis is considered as a possible source. However, Petaev et al. (2013) applied very high levels of quality control during their research, suggesting that external and internal (their laboratory) contamination is unlikely.

Corrections were made for interferences of LuO and HfO with Ir and Pt, and elevated concentrations occur over a range of ice depths, so the likelihood of ICP-MS error as the Pt spike origin is unlikely (Petaev et al., 2013). “Real” ice core samples were cleaned prior to analysis, and composite samples that were not precleaned and were tested in a different analytical session also showed elevated Pt concentrations – an overall consistency within the ice samples provides evidence against contamination at laboratory level (Petaev et al., 2013). Therefore, any possible contamination is likely to have occurred prior to research by Petaev et al. (2013). However, rigorous quality control techniques are employed at each stage of ice core drilling to eliminate contamination, for example, drill liquid (which is used to prevent borehole deformation in bores >100m deep) contamination is monitored, and ice “sticks” are extracted from the centre of the drilled core (Warming et al., 2013). Water alone is highly unlikely to mobilise the PGEs as they are fairly insoluble, and therefore drilling and slicing are unlikely contamination sources (Petaev et al., 2013). If the PGEs are in F^-- or Cl^--complexes (Section 6.2.3), they could mobilise readily (Eichler et al., 2001), but no data is available on this phenomenon during ice core drilling. Likelihood of contamination is low and is therefore not considered as a viable option for the GISP2 Pt spike origin.

6.3.4. Pt Nugget Effect

Heterogeneous dispersion of Pt, Pd and Ir can occur, leading to high variability within any one sample even after duplicate testing – a phenomenon aptly named the “nugget effect” (Firestone et al., 2007; Moore et al., 2017). The nugget effect is more common when measuring elements at low concentrations, and therefore could affect Pt in the ice measured in ppt (Moore et al., 2017). However, the presence of consistent Pt concentrations, and importantly increasing and subsequently decreasing concentrations across both the precleaned “real” samples

and the composite samples (not precleaned) demonstrates the Pt nugget effect is not applicable to the GISP2 Pt spike (Petaev et al., 2013).

6.4. Summary and Further Implications

The GISP2 Pt spike occurs ~60 years after $\delta^{18}O$ began decreasing in the NGRIP ice core, marking the GS-1 (YD) onset in the north Atlantic (Fig. 5.1). The geochemistry of the Pt anomaly is unlike common meteorites, volcanic rocks, the LSE (this report), YDB sediments, KTB sediments and Holocene volcanic eruptions in snow and ice (Figs. 5.4a-f; 6.2). Due to the chronological offset of the LSE and the Pt spike, and Pt-poor nature of the LST, it is unlikely that the LSE was the cause of the GISP2 Pt spike. A sudden, smaller increase of Pt (two small peaks) observed in the GISP2 ice core is contemporaneous with the LSE sulfate spike (Figs. 6.2; 6.4), and thus the LSE is a possible source of Pt at this particular time.

The geochemical ratios of the GISP2 Pt spike lie closest to meteorites (Fig. 5.4a-f), so the suggestion of multiple injections of highly fractionated iron meteorites not yet observed on Earth as the Pt spike origin is not implausible (Petaev et al., 2013), although the hypothesis of an “unknown” meteorite is untestable. A well-constrained impact crater for the hypothesised YDIH impactor does not exist (Kennett et al., 2009). Although the newly discovered Hiawatha Crater dates overlap with the GISP2 Pt spike timing (Kjær et al., 2018), the dates have very large uncertainties and debate exists whether the feature beneath the Greenland Ice Sheet is actually an impact crater. Atmospheric processing could explain the extreme fractionation, either of the volcanic aerosol of a different volcanic eruption (i.e. not the LSE due to the discussed chronological offset), or of a meteorite impact of standard composition, such as the Cape York meteorite (Boslough, 2013). Furthermore, alteration or remobilisation after deposition in snow or ice could fractionate the volatile PGEs to an extent not observed in the original meteoritic or volcanogenic source rocks (T. Meisel, pers. comm, 24th June 2019).

6.4.1. The Younger Dryas

This study suggests the LSE is unlikely to be the GISP2 Pt spike source because of the chronological offset between the eruption and the GISP2 Pt spike, as well as geochemical differences. This study also suggests that the GISP2 Pt spike is not contemporaneous with the $\delta^{18}O$ decrease in NGRIP demarcating the

beginning of GS-1 (Fig. 5.1), implying that the Pt spike source was not the initial trigger of the YD.

Although not the primary objective of the study, these results support a link between the LSE and the YD. The volcanogenic sulfate spike at 12.867 ka BP in the GISP2 ice core, contemporaneous with $\delta^{18}O$ decrease in the NGRIP ice core (and thus GS-1 onset), is consistent with the timing of the sulfur-rich Laacher See eruption, as noted in previous research (Baldini et al., 2018). Sulfur-rich eruptions create an aerosol haze that advects around the globe, directly impacting the Earth's radiative budget and indirectly influencing atmospheric circulation (Rampino & Self, 1984; Robock & Mao, 1995; Robock, 2000). The aerosol persists for an average of ~1-3 years (Robock & Mao, 1995; Robock, 2000; Baldini et al., 2018), although some may persist for longer (Robock et al., 2009; Timmreck et al., 2012). Therefore, the ~83 Mt SO_2 released during the LSE formed a volcanogenic aerosol that feasibly persisted for longer than average, and the restriction of the aerosol to one hemisphere may have increased its residence time and almost certainly amplified its radiative impact (Pinto et al., 1989; Toohey et al., 2019). Volcanogenic halogens released by the LSE (notably Cl), could have intensified initial radiative effects (Cadoux et al., 2014; Baldini et al., 2018).

Nonetheless the initial sulfur-loading caused subsequent radiative budget impacts, likely leading to SST decrease (Rampino & Self, 1984; Robock, 2000, 2002). The LSE occurred during a sensitive deglacial climate (with intermediate ice conditions), which perhaps exacerbated the initial forcing and catalysed positive long-term climate feedback (Zhang et al., 2014, 2017; Baldini et al., 2018). Lower SSTs lead to a series of positive feedback events including arctic sea ice expansion and reduced ocean-atmosphere heat flux, which eventually generates further cooling and sea-ice growth (Broecker, 2006b; Serreze and Francis, 2006; Miller et al., 2012; Lehner et al., 2013; Baldini et al., 2018). Melting of southward-extending sea ice results in freshwater input, ultimately causing NADW shutdown and subsequently weakening AMOC (Lehner et al., 2013; Baldini et al., 2018). Atmospheric circulation changes, including southward forcing of the ITCZ and NH polar front, may lead to more sea ice expansion and thus further cooling and AMOC deterioration (Renssen et al., 2015; Baldini et al. 2015b, 2018).

The same positive feedback chains, starting with short-term cooling generated by volcanogenic aerosol, sea-ice growth and AMOC weakening, are proposed for other geological periods, such as the Little Ice Age (Miller et al., 2012) and other Greenland stadials (Baldini et al., 2015a). The above chain of events

suggests that the well-constrained LSE (12.880 ka BP) is the simplest explanation for the initial GS-1 cooling that eventually led to the Younger Dryas cooling event.

Rather than requiring a cataclysmic trigger such as an impact, substantial research supports the YD as one of many rapid climate change events (see Rasmussen et al., 2016) intrinsic to “intermediate” climate states during transitions from glacial maxima to interglacials (e.g. Sima et al., 2004; Broecker et al., 2010; Baldini et al., 2018).

Although the Pt spike origin remains unclear, it may represent a subsequent radiative cooling event that could have exacerbated initial cooling forced by the LSE or a meltwater pulse. If the Pt spike source was an iron meteorite impacting the Greenland Ice Sheet (see Firestone et al., 2007; Petaev et al., 2013), the initial impacts may include: i) ozone depletion, ii) wildfires, iii) water vapour and ice release into the atmosphere and iv) destabilisation of the LIS (Toon et al., 1997; Firestone et al., 2007; Wolbach et al., 2018a, 2018b). Factors i), ii) and iii) could impact the Earth’s radiative budget which cause a cascade of climate feedbacks and ultimately cooling (Toon et al., 1997; Firestone et al., 2007; Wolbach et al., 2018a, b), and factor iv) may lead to a meltwater pulse, suppressing the NADW and weakening AMOC which eventually drives climate cooling (Berger, 1990; Alley, 2000; Broecker et al., 2010; Schenk et al., 2018; Baldini et al., 2018). However, a large iron meteorite impact such as that advocated by the YDIH has no modern analogue, therefore the climate effects are poorly understood. Furthermore, airburst physics relating to meteorites are complex (Chyba et al., 1993; Boslough et al., 2013) and this brings into question whether an iron meteorite could distribute Pt to the ice sheet unless it directly impacted the ice sheet, or instead, impacted continental crust and produced ejecta debris (and associated aerosol) that was a mixture of meteoritic and target rock compositions (Sawlowicz, 1993; Wolbach et al., 2018a, 2018b). A well-defined YDB impact crater remains undiscovered, because the Hiawatha glacier crater is poorly constrained (Kjær et al., 2018), and ice cores covering the YD interval show no evidence of a physical disturbance, suggesting that a direct, cataclysmic impact to the Greenland Ice sheet is an unlikely cause of the Pt spike. Alternatively, a noncataclysmic meteorite impact, such as the Cape York meteorite, could explain the Pt spike (Boslough, 2013), but would have minimal climate implications.

Although this study has no implications on the meltwater pulse hypothesis as there is no link between the Pt spike and a meltwater pulse, it is speculated that, because meltwater input indisputably occurred during the last deglacial period

(Baldini et al., 2018), this could have amplified climate response to catalyse the YD. Whether this was a catastrophic meltwater release suggested by the meltwater pulse hypothesis (e.g. Johnson and McClure, 1976; Rooth, 1982; Broecker et al., 1989; Berger, 1990; Alley, 2000; Broecker et al., 2010), or freshwater input caused by melting of southward-extending sea ice as part of positive feedback mechanisms (Lehner et al., 2013; Baldini et al., 2018) following an initial trigger (i.e. the LSE or a bolide impact) is unclear. It is tenable that the LSE, a bolide impact and a meltwater pulse occurred in close proximity, reinforcing each individual event's short-term climate impacts.

In short, this research suggests that the most parsimonious series of events leading to the YD were: i) the LSE triggering GS-1, alone or in combination with a meltwater pulse, and ii) a noncataclysmic bolide impact or a different Pt-rich eruption ~60 years later responsible for the GISP2 Pt concentration spike. The radiative effects associated with the event causing the Pt spike may have contributed to the severity of the YD, but were clearly not the main trigger due to the chronological offset.

6.5. Future Work

To provide further insight into the source of the Pt spike, more geochemical analyses in addition to that already conducted by Petaev et al. (2013), are required. The analysis of "meteoritic" elements such as Ni, Cr, Co, Cu and Ru and "volcanic" elements such as Ti, Zr, Ag, La, Ce, Au, Cd, Hg, Sr, Se, As, Sb, Ta, Pb and the rare earth elements (Sawlowicz, 1993; Gabrielli et al., 2008; Lowe et al., 2011; Andronikov et al., 2014, 2015, 2016) would help to "fingerprint" either a volcanogenic or meteoritic source of the Pt spike. The analysis of Pt, further elements analysed by Petaev et al. (2013), and the elements discussed above in other ice cores (such as NGRIP) would aid understanding of the Pt anomaly's origin, and analysis of those elements across a longer time period at close sampling intervals would demonstrate whether the Pt peak is a unique event or not. Further studies should focus on determining sources of the other sulfate spikes in the GISP2 ice core, Pt-rich eruptions, Pt mobilisation in the volcanic aerosol, the role of atmospheric processing and the potential for fractionation of PGEs in the aerosol, and lastly PGE fractionation in the snow or ice by alteration or remobilisation after deposition.

7. Conclusion

This report has presented evidence that the LSE is not the source of the GISP2 Pt spike, firstly because there is a chronological discrepancy between the interpreted LSE sulfur spike (12.687 ka BP) and the Pt spike (12.822 ka BP) in the same ice core and secondly by showing that the LST has low Pt concentrations. The LSE formed a volcanogenic aerosol that was advected around the globe. Platinum aerosol layers can form within the volcanogenic aerosol, travelling in a volatile phase or as complexes with volcanogenic halogens (Symonds et al., 1992; Simon & Pettke, 2009; Mather et al., 2012; Tankersley et al., 2018). However, there is no evidence to suggest the LSE's magnitude, large amount of SO_2 injection directly into the stratosphere (as a result of plume height >20km) or restriction to the NH could have prolonged the volcanogenic aerosol's lifetime beyond the average ~1-3 years (Robock and Mao, 1995; Harms & Schmincke, 2000; Robock, 2000; Baldini et al., 2018). Post-depositional processes, such as snow drift, wind erosion, reversible deposition, infiltration and refreezing events and mobilisation or chemical changes in the snow may act to distort the trace element signal at the time of deposition or shortly after (Bales et al., 1992; Alley, 2000; Harper et al., 2012; Gabrielli and Vallelonga, 2015; Gautier et al., 2016). Chronological offset in ice cores exists between CO_2 and the surrounding ice (Δage) due to post-depositional processes (Goujon et al., 2003), however, there is no evidence available to suggest PGE fractionation or Pt mobilisation occurs post-deposition into the ice core, and no viable process to explain such a phenomenon exists.

Therefore, no known mechanism exists to explain the delay of ~60 years between the eruption and the GISP2 Pt spike. Additionally, new detailed geochemical analyses of the LST (this report) demonstrate that the material has low Pt concentrations. Consequently, it is unlikely that the LSE is the source of high Pt concentrations at the GISP2 Pt spike.

An alternative explanation for the Pt spike is that it is derived from a large iron meteorite impact, as suggested by Petaev et al. (2013). Recent research on the YDIH links the Pt spike to the YD (e.g. Wolbach et al., 2018a, b), however, there are chronological discrepancies between YDB sites (the mean age of the YDB layer is 12.938± 0.25 BP; Firestone et al., 2007) and the GISP2 Pt spike. A large bolide impact could generate significant amounts of dust and an aerosol akin to explosive volcanic eruptions (Toon et al., 1997; Firestone et al., 2007). Similar to volcanogenic

aerosol from the LSE, atmospheric processing and post-depositional processes do not provide an explanation for a ~30-100-year offset between YDB sediments and the GISP2 Pt spike. Therefore, it is highly unlikely the hypothesised YDIH impactor is the origin of elevated Pt concentrations at the GISP2 Pt spike. Alternatively, if the GISP2 Pt spike is considered the result of another impact with more localised effects, a noncataclysmic impact, such as the Cape York meteorite impact, could deposit Pt onto the Greenland Ice Sheet (Boslough, 2013).

The unusual geochemistry of the Pt spike (i.e. high Pt/Ir and Pt/Al ratios) is difficult to link to common meteorites or magmas (Fig. 5.3a-f). This report explored the potential of Pt enrichment and fractionation in the melt and volcanic aerosol, in reference to the LSE and other volcanic eruptions (represented by other sulfate spikes in the GISP2 ice core). Despite the Pt-poor nature of the LST deposits, it is possible that Pt-rich magma degassed volatiles and trace species prior to or during the eruption, aided by the sulfur-rich nature of the LSE and presence of volcanogenic halogens (such as Cl, forming Pt-Cl-complexes), and was transported to the Greenland Ice Sheet (Aiuppa et al., 2003; Mungall & Naldrett, 2008; Mather et al., 2012; Edmonds & Mather, 2017; Tankersley et al., 2018). Platinum fractionation could also occur during chemical or atmospheric processing of the volcanic cloud (e.g. Langmann, 2014). However, no evidence of such high levels of fractionation exists in other possibly Pt-rich eruptions in ice cores (Fig. 6.2). Although the chronological offset suggests the LSE was not the source of the GISP2 Pt spike, the LSE may have contributed to two smaller Pt peaks in the GISP2 ice core, contemporaneous with the LSE sulfate spike (Fig. 6.4). However, the results of this report cannot confirm whether the LSE aerosol was Pt-rich, but can confirm the proximal tephra was not. Alternatively, the GISP2 Pt spike could result from a local, less explosive eruption occurring closer in time; for example, related to the volcanic eruption responsible for a small sulfate spike in the GISP2 ice core at 12.829 ka BP (Fig. 5.1). Another fractionation process includes alteration or mobilisation following deposition of volcanogenic aerosol onto the ice sheet. The possibility of fractionation of Pt due to meltwater influx, mobilisation of ionic species carrying Pt-complexes (e.g. Cl^-) and reversible deposition (Sawlowicz, 1993; Eichler et al., 2001; Gabrielli et al., 2012; Gabrielli and Vallelonga, 2015) is perhaps the simplest explanation for the highly fractionated Pt/Ir ratio of the GISP2 Pt spike, however more research is required to understand the mobility of PGEs in the firn and ice layers.

In addition to a chronological offset, early YDIH advocates suggested an Ir-rich impactor, whereas the GISP2 Pt spike is Ir-poor (Petaev et al., 2013), and GISP2 Pt spike geochemistry does not match other known meteorites (Fig. 5.3a-f). Therefore, the hypothesised YDIH impactor as the GISP2 Pt spike origin is unlikely, and instead, another impact by an “unknown” meteorite, unrelated to the YDIH is a potential Pt source. Aside from the poorly constrained Hiawatha glacier crater (Kjær et al., 2018), there is currently no impact crater dated to this time period. A noncataclysmic entry of a meteorite body (Cape York) was previously proposed (Boslough, 2013), however its geochemical signature is dissimilar from the GISP2 Pt spike. Condensation or oxidation fractionation, ablation or precipitation following impact could explain the extreme fractionation of Pt/Ir, however these mechanisms are poorly understood.

Alternative plausible sources of Pt were discussed, including seawater in a sea-salt aerosol (Nozaki, 1997), volcanic exhalations and hydrothermal deposits (e.g. Sawlowicz, 1993; Pašava et al., 2007), contamination of the ice and the Pt nugget effect (e.g. Firestone et al., 2007; Moore et al., 2017), but were ultimately ruled out as Pt sources.

This report supports the LSE as the simplest explanation for the YD cooling. Initial cooling was driven by the LSE aerosol and subsequent climate feedback within a sensitive deglacial climate prolongs the climate impacts (Baldini et al., 2018). Changes in the Earth’s radiation budget caused by the LSE aerosol and leading to SST decrease (Rampino & Self, 1984; Robock, 2000, 2002) may have caused a cascade of climate feedbacks including sea ice growth, atmospheric circulation changes, AMOC weakening and ultimately cooling (Broecker, 2006b; Serreze and Francis, 2006; Miller et al., 2012; Lehner et al., 2013; Renssen et al., 2015; Baldini et al., 2018). However, the possibility exists that these effects were extended by another event affecting the Earth’s radiative budget, which could have amplified the initial aerosol cooling. The Pt spike in the GISP2 ice core ~60 years after GS-1 onset (the cooling leading to the YD) could represent a non-cataclysmic bolide impact of an unknown type of iron meteorite, or an unidentified volcanic eruption that could have led to radiative cooling. However, as the GISP2 Pt spike source is still enigmatic, it is difficult to ascertain whether the elevated Pt represents an event that did affect the Earth’s radiative budget, and whether it had any climate implications. This report provides no evidence to confirm or deny the possibility of more than one event occurring close in time, for example, the LSE, a bolide impact

and a meltwater pulse, and such timing could have substantial climate repercussions and possibly prolong the YD.

Further research is required to determine the origin of the GISP2 Pt spike, including analysis of additional “meteoric” and “volcanic” elements in the GISP2 ice core, analysis of other ice cores (e.g. NGRIP) for Pt and additional elements within the same interval studied in the GISP2 ice core by Petaev et al. (2013), and analysis for Pt in older and younger sections of ice to determine whether the GISP2 Pt spike of 12.822 ka BP was unique or simply part of the glacial-deglacial sequence.

Appendices

Appendix 1: (a) lab certificate of analyses, (b) quality control and (c) full analytical results of the Laacher See tephra samples by Activation Laboratories (ActLabs) and spider diagrams of trace element geochemistry (provided by ActLabs).

Appendix 1a:

Quality Analysis ...  *Innovative Technologies*

Date Submitted: 15-Feb-19
Invoice No.: A19-02357
Invoice Date: 10-May-19
Your Reference: LAACHER SEE

Durham University
Dept of Earth Sciences
Science Labs
Durham DH1 3LE
United Kingdom

ATTN: Charlotte Green

CERTIFICATE OF ANALYSIS

18 Crushed Rock samples were submitted for analysis.

The following analytical package(s) were requested:

Code 1B (3+) Nickel Sulphide INAA(INAAGEO)

Code 1C-Res Fire Assay-ICP/MS

Code 4LITHO (11+) Major Elements Fusion ICP(WRA)/Trace Elements Fusion ICP/MS(WRA4B2)

REPORT **A19-02357**

Notes:

We recommend reanalysis by fire assay Au, Pt, Pd Code 8 if values exceed upper limit.

We recommend using option 4B1 for accurate levels of the base metals Cu, Pb, Zn, Ni and Ag. Option 4B-INAA for As, Sb, high W >100ppm, Cr >1000ppm and Sn >50ppm by Code 5D. Values for these elements provided by Fusion ICP/MS, are order of magnitude only and are provided for general information. Mineralized samples should have the Quant option selected or request assays for values which exceed the range of option 4B1. Total includes all elements in % oxide to the left of total.

Appendix 1b:

Report Number: A19-02357

Report Date: 10/5/2019

Analyte Symbol	Au	Pt	Pd	SiO2	Al2O3	Fe2O3(T)	MnO	MgO	CaO	Na2O
Unit Symbol	ppb	ppb	ppb	%	%	%	%	%	%	%
Detection Limit	1	0.1	0.1	0.01	0.01	0.01	0.001	0.01	0.01	0.01
Analysis Method	FA-MS	FA-MS	FA-MS	FUS-ICP	FUS-ICP	FUS-ICP	FUS-ICP	FUS-ICP	FUS-ICP	FUS-ICP
NIST 694 Meas				11.08	1.9	0.73	0.014	0.33	42.39	0.87
NIST 694 Cert				11.2	1.8	0.79	0.0116	0.33	43.6	0.86
DNC-1 Meas				47.29	18.8	9.96	0.146	10.1	11.38	1.92
DNC-1 Cert				47.15	18.34	9.97	0.15	10.13	11.49	1.89
GBW 07113 Meas				71.26	12.7	3.14	0.138	0.14	0.59	2.48
GBW 07113 Cert				72.8	13	3.21	0.14	0.16	0.59	2.57
W-2a Meas				52.87	15.37	10.82	0.166	6.31	11.37	2.26
W-2a Cert				52.4	15.4	10.7	0.163	6.37	10.9	2.14
SY-4 Meas				50.66	20.28	6.15	0.108	0.51	8.17	6.92
SY-4 Cert				49.9	20.69	6.21	0.108	0.54	8.05	7.1
BIR-1a Meas				48.67	15.45	11.34	0.173	9.6	13.61	1.82
BIR-1a Cert				47.96	15.5	11.3	0.175	9.7	13.3	1.82
PK2 Meas	4660	4450	5590							
PK2 Cert	4785	4749	5918							
PK2 Meas	4770	4580	5700							
PK2 Cert	4785	4749	5918							
PK2 Meas	4830	4650	5730							
PK2 Cert	4785	4749	5918							
CDN-PGMS-29 Meas	93	534	689							
CDN-PGMS-29 Cert	88	550	677							

Report Number: A19-02357

Report Date: 10/5/2019

Analyte Symbol	Au	Pt	Pd	SiO2	Al2O3	Fe2O3(T)	MnO	MgO	CaO	Na2O
Unit Symbol	ppb	ppb	ppb	%	%	%	%	%	%	%
Detection Limit	1	0.1	0.1	0.01	0.01	0.01	0.001	0.01	0.01	0.01
Analysis Method	FA-MS	FA-MS	FA-MS	FUS-ICP	FUS-ICP	FUS-ICP	FUS-ICP	FUS-ICP	FUS-ICP	FUS-ICP
CDN-PGMS-29 Meas	82	522	654							
CDN-PGMS-29 Cert	88	550	677							
LST 001A Orig	2	0.1	0.1							
LST 001A Dup	2	0.1	0.1							
LST 007A Orig	2	< 0.1	< 0.1							
LST 007A Dup	6	0.1	0.1							
LST 008 Orig				54.76	17.73	3.4	0.133	0.65	7.05	4.82
LST 008 Dup				54.68	18.1	3.39	0.132	0.64	7	4.84
Method Blank				< 0.01	< 0.01	< 0.01	0.003	< 0.01	< 0.01	< 0.01
Method Blank	2	< 0.1	0.1							
Method Blank	2	< 0.1	0.1							
Method Blank	2	< 0.1	0.1							

Report Number: A19-02357

Report Date: 10/5/2019

Analyte Symbol	K2O	TiO2	P2O5	LOI	Total	Sc	Be	V	Ba	Sr
Unit Symbol	%	%	%	%	%	ppm	ppm	ppm	ppm	ppm
Detection Limit	0.01	0.001	0.01		0.01	1	1	5	2	2
Analysis Method	FUS-ICP	FUS-ICP	FUS-ICP	FUS-ICP	FUS-ICP	FUS-ICP	FUS-ICP	FUS-ICP	FUS-ICP	FUS-ICP
NIST 694 Meas	0.55	0.115	30.14					1535		
NIST 694 Cert	0.51	0.11	30.2					1740		
DNC-1 Meas	0.23	0.486	0.07			31		144	107	144
DNC-1 Cert	0.234	0.48	0.07			31		148	118	144
GBW 07113 Meas	5.36	0.283	0.04			5	4	< 5	501	41
GBW 07113 Cert	5.43	0.3	0.05			5	4	5	506	43
W-2a Meas	0.64	1.091	0.22			36	< 1	269	179	202
W-2a Cert	0.626	1.06	0.14			36	1.3	262	182	190
SY-4 Meas	1.69	0.283	0.12			< 1	3	6	347	1203
SY-4 Cert	1.66	0.287	0.131			1.1	2.6	8	340	1191
BIR-1a Meas	0.02	0.97	0.01			44	< 1	319	9	108
BIR-1a Cert	0.03	0.96	0.021			44	0.58	310	6	110
LST 008 Orig	6.53	0.82	0.17	3.94	100	2	2	69	1289	1046
LST 008 Dup	6.53	0.838	0.16	3.94	100.3	1	2	68	1283	1069
Method Blank	< 0.01	< 0.001	< 0.01			< 1	< 1	< 5	< 2	< 2

Report Number: A19-02357

Report Date: 10/5/2019

Analyte Symbol	Y	Zr	Cr	Co	Ni	Cu	Zn	Ga	Ge	As
Unit Symbol	ppm	ppm	ppm	ppm	ppm	ppm	ppm	ppm	ppm	ppm
Detection Limit	1	2	20	1	20	10	30	1	1	5
Analysis Method	FUS-ICP	FUS-ICP	FUS-MS	FUS-MS	FUS-MS	FUS-MS	FUS-MS	FUS-MS	FUS-MS	FUS-MS
DNC-1 Meas	14	33								
DNC-1 Cert	18	38								
GBW 07113 Meas	43	387								
GBW 07113 Cert	43	403								
TDB-1 Meas			250		110	330	150			
TDB-1 Cert			251		92	323	155			
W-2a Meas	18	86	90	43	80	110	80	17		< 5
W-2a Cert	24	94	92	43	70	110	80	17		1.2
DTS-2b Meas			> 10000	131	3390					
DTS-2b Cert			15500	120	3780					
SY-4 Meas	111	544		2			100	36		
SY-4 Cert	119	517		2.8			93	35		
BIR-1a Meas	12	13								
BIR-1a Cert	16	18								
ZW-C Meas			60				1000	95		
ZW-C Cert			56				1050	99		
USZ 44-2007 Meas			200				550	62		44
USZ 44-2007 Cert			200				534	64		43.7
REE-1 Meas			280	1	30	80				115
REE-1 Cert			277	1.58	24.7	79.7				124
LST 008 Orig	18	241	< 20	3	< 20	< 10	50	17	< 1	< 5

Report Number: A19-02357

Report Date: 10/5/2019

Analyte Symbol	Y	Zr	Cr	Co	Ni	Cu	Zn	Ga	Ge	As
Unit Symbol	ppm	ppm	ppm	ppm	ppm	ppm	ppm	ppm	ppm	ppm
Detection Limit	1	2	20	1	20	10	30	1	1	5
Analysis Method	FUS-ICP	FUS-ICP	FUS-MS	FUS-MS	FUS-MS	FUS-MS	FUS-MS	FUS-MS	FUS-MS	FUS-MS
LST 008 Dup	19	237	< 20	2	< 20	< 10	60	17	1	< 5
Method Blank	1	2	< 20	< 1	< 20	< 10	< 30	< 1	< 1	< 5

Report Number: A19-02357

Report Date: 10/5/2019

Analyte Symbol	Rb	Nb	Mo	Ag	In	Sn	Sb	Cs	La	Ce
Unit Symbol	ppm	ppm	ppm	ppm	ppm	ppm	ppm	ppm	ppm	ppm
Detection Limit	2	1	2	0.5	0.2	1	0.5	0.5	0.1	0.1
Analysis Method	FUS-MS	FUS-MS	FUS-MS	FUS-MS	FUS-MS	FUS-MS	FUS-MS	FUS-MS	FUS-MS	FUS-MS
TDB-1 Meas	20								16.4	38.3
TDB-1 Cert	23								17	41
W-2a Meas	19	6					0.8	0.8	10.6	23
W-2a Cert	21	7.9					0.79	0.99	10	23
SY-4 Meas	51	14						1.5	58.3	123
SY-4 Cert	55	13						1.5	58	122
ZW-C Meas	> 1000	209				> 1000	4.6	264	29.8	102
ZW-C Cert	8500	198				1300	4.2	260	30	97
NCS DC86318 Meas	373							11	> 2000	409
NCS DC86318 Cert	369.42							10.28	1960	430
SARM 3 Meas		981								
SARM 3 Cert		978								
USZ 44-2007 Meas	582					115			427	1130
USZ 44-2007 Cert	641					126			434	1000
REE-1 Meas		> 1000						1	1760	> 3000
REE-1 Cert		4050						1.07	1661	3960
LST 008 Orig	114	104	5	0.6	< 0.2	1	< 0.5	1	84.8	153
LST 008 Dup	114	103	5	0.5	< 0.2	1	< 0.5	0.9	86.9	155
Method Blank	< 2	< 1	< 2	< 0.5	< 0.2	< 1	< 0.5	< 0.5	< 0.1	< 0.1

Report Number: A19-02357

Report Date: 10/5/2019

Analyte Symbol	Pr	Nd	Sm	Eu	Gd	Tb	Dy	Ho	Er	Tm
Unit Symbol	ppm	ppm	ppm	ppm	ppm	ppm	ppm	ppm	ppm	ppm
Detection Limit	0.05	0.1	0.1	0.05	0.1	0.1	0.1	0.1	0.1	0.05
Analysis Method	FUS-MS	FUS-MS	FUS-MS	FUS-MS	FUS-MS	FUS-MS	FUS-MS	FUS-MS	FUS-MS	FUS-MS
TDB-1 Meas		23.9		2.03			6.5			
TDB-1 Cert		23		2.1			8			
W-2a Meas		12.9	3.3	1.13		0.6	3.8	0.8	2.2	0.31
W-2a Cert		13	3.3	1		0.63	3.6	0.76	2.5	0.38
SY-4 Meas	15.2	57.5	13.2	2.08	14.5	2.7	19.3	4.4	14.3	2.28
SY-4 Cert	15	57	12.7	2	14	2.6	18.2	4.3	14.2	2.3
ZW-C Meas	9.67	25.3	6.9		4.7					
ZW-C Cert	9.5	25	6.6		4.7					
NCS DC86318 Meas	757			19	> 1000		> 1000	612	> 1000	264
NCS DC86318 Cert	740			18.91	2095		3220	560	1750	270
USZ 44-2007 Meas	118	441	127		132	27.2	198	42.9		
USZ 44-2007 Cert	122	434	120		117	25	165	37		
REE-1 Meas		1450		24.7	439		889	211	712	
REE-1 Cert		1456		23.5	433		847	208	701	
LST 008 Orig	14.8	46.6	6.5	1.8	4.2	0.6	3.5	0.7	2.1	0.27
LST 008 Dup	15.2	47.9	6.6	1.83	4.2	0.6	3.5	0.7	2	0.28
Method Blank	< 0.05	< 0.1	< 0.1	< 0.05	< 0.1	< 0.1	< 0.1	< 0.1	< 0.1	< 0.05

Report Number: A19-02357

Report Date: 10/5/2019

Analyte Symbol	Yb	Lu	Hf	Ta	W	Tl	Pb	Bi	Th	U
Unit Symbol	ppm	ppm	ppm	ppm	ppm	ppm	ppm	ppm	ppm	ppm
Detection Limit	0.1	0.01	0.2	0.1	1	0.1	5	0.4	0.1	0.1
Analysis Method	FUS-MS	FUS-MS	FUS-MS	FUS-MS	FUS-MS	FUS-MS	FUS-MS	FUS-MS	FUS-MS	FUS-MS
TDB-1 Meas	3.2								2.6	
TDB-1 Cert	3.4								2.7	
W-2a Meas	2	0.31	2.4	0.4			8		2.1	0.5
W-2a Cert	2.1	0.33	2.6	0.5			9.3		2.4	0.53
SY-4 Meas	15.6	2.16	10.5				10		1.3	0.9
SY-4 Cert	14.8	2.1	10.6				10		1.4	0.8
ZW-C Meas				84.8	334	33.6				19.3
ZW-C Cert				82	320	34				20
NCS DC86316 Meas			774		6				196	
NCS DC86316 Cert			712		5.01				202	
NCS DC86318 Meas	> 1000	250							65	
NCS DC86318 Cert	1840	260							67	
USZ 44-2007 Meas	141		405	125			164		200	56.5
USZ 44-2007 Cert	123		400	123			149		202	57
REE-1 Meas			486							
REE-1 Cert			479							
LST 008 Orig	1.9	0.29	4.6	6.4	2	0.1	8	< 0.4	8.6	2.2
LST 008 Dup	1.9	0.28	4.6	6.4	1	0.1	11	< 0.4	8.6	2.2
Method Blank	< 0.1	< 0.01	< 0.2	< 0.1	< 1	< 0.1	< 5	< 0.4	< 0.1	< 0.1

Report Number: A19-02357

Report Date: 10/5/2019

Analyte Symbol	Os	Ir	Ru	Rh	Pt	Pd	Au	Mass
Unit Symbol	ppb	ppb	ppb	ppb	ppb	ppb	ppb	g
Detection Limit	2	0.1	5	0.2	5	2	0.5	
Analysis Method	NI-FINA	NI-FINA	NI-FINA	NI-FINA	NI-FINA	NI-FINA	NI-FINA	NI-FINA
OREAS 13b (Ni-S Fire Assay) Meas	14	17.1	68	< 0.2	178	124	205	
OREAS 13b (Ni-S Fire Assay) Cert	12	17.9	78	43	204	134	201	
AMIS 0367 (Ni-S) Meas					1630	790	178	
AMIS 0367 (Ni-S) Cert					1800	860	180	
AMIS 0414 (Ni-S) Meas					2050	1300		
AMIS 0414 (Ni-S) Cert					2200	1370		
LST 003A Orig	< 2	< 0.1	< 5	< 0.2	< 5	< 2	0.8	25
LST 003A Dup	< 2	< 0.1	< 5	< 0.2	< 5	< 2	1.5	25
Method Blank	< 2	< 0.1	< 5	< 0.2	< 5	< 2	0.8	25

Appendix 1c:

Report Number: A19-02357

Report Date: 10/5/2019

Analyte Symbol	Re	Au	Pt	Pd	SiO2
Unit Symbol	ppb	ppb	ppb	ppb	%
Detection Limit		1	0.1	0.1	0.01
Analysis Method	NI-FINA	FA-MS	FA-MS	FA-MS	FUS-ICP
LST 001		2	0.2	0.1	55.92
LST 001A		2	0.1	0.1	61.73
LST 002		2	< 0.1	< 0.1	56.29
LST 002A		2	0.1	0.1	63.57
LST 003		1	< 0.1	< 0.1	56.73
LST 003A		2	0.2	0.2	63.08
LST 003B		4	0.4	0.6	68.02
LST 004		2	< 0.1	< 0.1	57.25
LST 005		2	< 0.1	< 0.1	56.88
LST 006		2	< 0.1	< 0.1	57.4
LST 007		2	< 0.1	< 0.1	57.79
LST 007A		4	< 0.1	< 0.1	58.72
LST 008		5	< 0.1	0.1	54.72
SAMPLE A		2	< 0.1	< 0.1	56.28
SAMPLE B		2	< 0.1	0.2	58.55
SAMPLE C		2	0.1	< 0.1	56.63
SAMPLE D		2	< 0.1	< 0.1	55.29
LST1 TS		7	0.9	0.6	58.1

Report Number: A19-02357

Report Date: 10/5/2019

Analyte Symbol	Al2O3	Fe2O3(T)	MnO	MgO	CaO
Unit Symbol	%	%	%	%	%
Detection Limit	0.01	0.01	0.001	0.01	0.01
Analysis Method	FUS-ICP	FUS-ICP	FUS-ICP	FUS-ICP	FUS-ICP
LST 001	20.59	1.92	0.48	0.07	0.4
LST 001A	17.65	3.24	0.379	0.55	0.65
LST 002	21.09	1.99	0.471	0.09	0.43
LST 002A	16.88	3.53	0.369	0.61	0.58
LST 003	20.68	1.92	0.42	0.09	0.5
LST 003A	17.08	3.83	0.325	0.57	0.43
LST 003B	14.52	6.75	0.168	1.5	0.32
LST 004	20.6	2.26	0.272	0.18	1.01
LST 005	20.51	2.1	0.27	0.12	0.98
LST 006	20.08	2.45	0.241	0.21	1.27
LST 007	19.19	2.92	0.181	0.35	1.9
LST 007A	20.01	2.77	0.205	0.34	1.71
LST 008	17.92	3.4	0.132	0.65	7.03
SAMPLE A	21.37	1.92	0.424	0.08	0.5
SAMPLE B	19.86	2.93	0.186	0.37	1.91
SAMPLE C	20.37	2.07	0.269	0.12	0.99
SAMPLE D	18.75	3.82	0.141	0.76	5.34
LST1 TS	17.79	5.53	0.219	1.16	2.16

Report Number: A19-02357

Report Date: 10/5/2019

Analyte Symbol	Na2O	K2O	TiO2	P2O5	LOI
Unit Symbol	%	%	%	%	%
Detection Limit	0.01	0.01	0.001	0.01	
Analysis Method	FUS-ICP	FUS-ICP	FUS-ICP	FUS-ICP	FUS-ICP
LST 001	10.53	4.89	0.138	0.02	3.58
LST 001A	7.11	3.83	0.329	0.08	3.85
LST 002	10.35	4.88	0.146	0.03	3.47
LST 002A	6.82	3.64	0.339	0.07	3.7
LST 003	10.18	4.97	0.154	0.02	3.12
LST 003A	6.47	3.75	0.357	0.06	3.34
LST 003B	1.16	2.68	0.778	0.17	3.73
LST 004	8.74	5.64	0.252	0.04	3.19
LST 005	8.67	5.67	0.219	0.03	4.03
LST 006	7.5	5.91	0.309	0.04	3.83
LST 007	5.94	6.5	0.532	0.08	3.32
LST 007A	6.98	6.27	0.462	0.07	1.3
LST 008	4.83	6.53	0.829	0.16	3.94
SAMPLE A	10.35	5.11	0.155	0.01	3.04
SAMPLE B	6.16	6.59	0.535	0.09	3.11
SAMPLE C	8.58	5.72	0.221	0.03	3.75
SAMPLE D	4.82	6.72	0.946	0.18	2.38
LST1 TS	2.2	3.71	1.064	0.31	7.99

Report Number: A19-02357

Report Date: 10/5/2019

Analyte Symbol	Total	Sc	Be	V	Ba
Unit Symbol	%	ppm	ppm	ppm	ppm
Detection Limit	0.01	1	1	5	2
Analysis Method	FUS-ICP	FUS-ICP	FUS-ICP	FUS-ICP	FUS-ICP
LST 001	98.55	< 1	20	8	14
LST 001A	99.4	3	14	32	137
LST 002	99.21	< 1	19	8	16
LST 002A	100.1	4	12	35	140
LST 003	98.79	< 1	16	9	19
LST 003A	99.29	5	10	38	153
LST 003B	99.8	14	2	96	446
LST 004	99.44	< 1	7	20	114
LST 005	99.48	< 1	7	16	85
LST 006	99.24	< 1	6	25	140
LST 007	98.72	< 1	3	42	408
LST 007A	98.85	1	4	37	302
LST 008	100.1	1	2	68	1286
SAMPLE A	99.25	< 1	17	9	22
SAMPLE B	100.3	< 1	3	43	404
SAMPLE C	98.76	< 1	7	17	86
SAMPLE D	99.16	2	2	78	1472
LST1 TS	100.2	9	3	105	867

Report Number: A19-02357

Report Date: 10/5/2019

Analyte Symbol	Sr	Y	Zr	Cr	Co
Unit Symbol	ppm	ppm	ppm	ppm	ppm
Detection Limit	2	1	2	20	1
Analysis Method	FUS-ICP	FUS-ICP	FUS-ICP	FUS-MS	FUS-MS
LST 001	9	31	2109	< 20	< 1
LST 001A	64	27	1422	40	6
LST 002	10	30	2045	< 20	1
LST 002A	62	27	1337	60	7
LST 003	13	27	1752	< 20	1
LST 003A	41	24	1115	60	7
LST 003B	85	25	187	130	18
LST 004	79	17	859	< 20	1
LST 005	62	15	854	< 20	1
LST 006	112	15	689	< 20	1
LST 007	313	15	438	< 20	2
LST 007A	229	15	540	< 20	2
LST 008	1057	19	239	< 20	3
SAMPLE A	14	28	1778	< 20	< 1
SAMPLE B	314	15	453	< 20	2
SAMPLE C	65	16	858	< 20	< 1
SAMPLE D	1217	19	244	< 20	3
LST1 TS	486	24	341	90	15

Report Number: A19-02357

Report Date: 10/5/2019

Analyte Symbol	Ni	Cu	Zn	Ga	Ge
Unit Symbol	ppm	ppm	ppm	ppm	ppm
Detection Limit	20	10	30	1	1
Analysis Method	FUS-MS	FUS-MS	FUS-MS	FUS-MS	FUS-MS
LST 001	< 20	< 10	250	55	3
LST 001A	< 20	< 10	190	41	2
LST 002	< 20	< 10	230	52	2
LST 002A	20	10	170	38	2
LST 003	< 20	< 10	220	51	2
LST 003A	20	< 10	140	35	2
LST 003B	60	20	390	19	2
LST 004	< 20	< 10	120	33	2
LST 005	< 20	< 10	130	34	1
LST 006	< 20	< 10	110	30	1
LST 007	< 20	< 10	80	23	1
LST 007A	< 20	< 10	90	26	1
LST 008	< 20	< 10	60	17	< 1
SAMPLE A	< 20	< 10	210	49	2
SAMPLE B	< 20	< 10	80	24	1
SAMPLE C	< 20	< 10	120	33	1
SAMPLE D	< 20	< 10	60	18	< 1
LST1 TS	40	20	100	22	1

Report Number: A19-02357

Report Date: 10/5/2019

Analyte Symbol	As	Rb	Nb	Mo	Ag
Unit Symbol	ppm	ppm	ppm	ppm	ppm
Detection Limit	5	2	1	2	0.5
Analysis Method	FUS-MS	FUS-MS	FUS-MS	FUS-MS	FUS-MS
LST 001	12	540	352	2	5.1
LST 001A	18	398	210	2	4
LST 002	10	511	337	2	5.2
LST 002A	10	357	187	2	3.8
LST 003	13	497	301	2	4.8
LST 003A	9	320	157	2	2.8
LST 003B	9	142	11	< 2	0.6
LST 004	8	298	155	3	2.1
LST 005	< 5	306	160	3	2
LST 006	< 5	265	147	3	1.8
LST 007	< 5	178	123	3	1
LST 007A	< 5	207	126	4	1.3
LST 008	< 5	114	104	5	0.6
SAMPLE A	9	480	295	2	4.3
SAMPLE B	< 5	184	123	3	1.2
SAMPLE C	7	295	157	3	2
SAMPLE D	< 5	116	108	5	0.5
LST1 TS	7	130	84	< 2	0.8

Report Number: A19-02357

Report Date: 10/5/2019

Analyte Symbol	In	Sn	Sb	Cs	La
Unit Symbol	ppm	ppm	ppm	ppm	ppm
Detection Limit	0.2	1	0.5	0.5	0.1
Analysis Method	FUS-MS	FUS-MS	FUS-MS	FUS-MS	FUS-MS
LST 001	< 0.2	2	1.7	12.7	224
LST 001A	< 0.2	2	1.5	9.8	158
LST 002	< 0.2	2	1.4	11.9	210
LST 002A	< 0.2	2	1.4	8.8	146
LST 003	< 0.2	2	1.4	11	204
LST 003A	< 0.2	2	1.2	7.6	128
LST 003B	< 0.2	2	0.7	4.4	41.8
LST 004	< 0.2	1	0.7	4.9	139
LST 005	< 0.2	1	0.6	4.9	138
LST 006	< 0.2	1	0.5	3.8	126
LST 007	< 0.2	1	< 0.5	2.1	104
LST 007A	< 0.2	1	< 0.5	2.7	109
LST 008	< 0.2	1	< 0.5	0.9	85.9
SAMPLE A	< 0.2	2	1.3	10.8	197
SAMPLE B	< 0.2	1	< 0.5	2.2	106
SAMPLE C	< 0.2	1	0.6	4.7	136
SAMPLE D	< 0.2	1	< 0.5	1	90.6
LST1 TS	< 0.2	3	0.9	2.9	83.3

Report Number: A19-02357

Report Date: 10/5/2019

Analyte Symbol	Ce	Pr	Nd	Sm	Eu
Unit Symbol	ppm	ppm	ppm	ppm	ppm
Detection Limit	0.1	0.05	0.1	0.1	0.05
Analysis Method	FUS-MS	FUS-MS	FUS-MS	FUS-MS	FUS-MS
LST 001	277	17	35.3	3.4	0.44
LST 001A	203	13.6	33.3	4.2	0.69
LST 002	262	16.2	34	3.3	0.44
LST 002A	189	13.2	32.3	4.2	0.75
LST 003	250	15.6	32.2	3.1	0.44
LST 003A	168	12	30.7	4.2	0.76
LST 003B	82.9	9.56	35	6.7	1.43
LST 004	174	11.6	25.5	2.7	0.48
LST 005	172	11.1	24.2	2.2	0.4
LST 006	164	11.1	26.1	2.7	0.56
LST 007	152	12.2	32.8	4	1.01
LST 007A	154	11.9	29.9	3.4	0.86
LST 008	154	15	47.3	6.5	1.82
SAMPLE A	243	15.1	31.2	3.1	0.41
SAMPLE B	153	12	31.9	3.6	0.97
SAMPLE C	167	10.8	23.5	2.5	0.43
SAMPLE D	165	16.3	52	7.2	2.11
LST1 TS	151	13.9	46.4	7.1	1.75

Report Number: A19-02357

Report Date: 10/5/2019

Analyte Symbol	Gd	Tb	Dy	Ho	Er
Unit Symbol	ppm	ppm	ppm	ppm	ppm
Detection Limit	0.1	0.1	0.1	0.1	0.1
Analysis Method	FUS-MS	FUS-MS	FUS-MS	FUS-MS	FUS-MS
LST 001	2.5	0.5	3.5	0.9	3.6
LST 001A	3	0.5	3.7	0.8	3
LST 002	2.1	0.4	3.3	0.8	3.4
LST 002A	3.1	0.5	3.6	0.8	3
LST 003	2	0.4	3	0.8	3.2
LST 003A	3	0.6	3.5	0.8	2.7
LST 003B	5.6	0.9	5	1	2.7
LST 004	1.7	0.3	2	0.5	2
LST 005	1.4	0.3	2	0.5	1.8
LST 006	1.8	0.3	1.9	0.5	1.7
LST 007	2.5	0.4	2.5	0.5	1.6
LST 007A	2.2	0.4	2.3	0.5	1.7
LST 008	4.2	0.6	3.5	0.7	2
SAMPLE A	2	0.4	3	0.8	3.1
SAMPLE B	2.4	0.4	2.3	0.5	1.7
SAMPLE C	1.5	0.3	1.9	0.4	1.8
SAMPLE D	4.7	0.7	3.9	0.7	2.2
LST1 TS	4.9	0.8	4.5	0.9	2.6

Report Number: A19-02357

Report Date: 10/5/2019

Analyte Symbol	Tm	Yb	Lu	Hf	Ta
Unit Symbol	ppm	ppm	ppm	ppm	ppm
Detection Limit	0.05	0.1	0.01	0.2	0.1
Analysis Method	FUS-MS	FUS-MS	FUS-MS	FUS-MS	FUS-MS
LST 001	0.72	6.1	1.13	37	6.3
LST 001A	0.58	4.9	0.88	25	4.5
LST 002	0.69	5.9	1.06	35.8	6.1
LST 002A	0.56	4.5	0.81	23.6	4.1
LST 003	0.6	5.4	1.05	31.3	5.8
LST 003A	0.51	3.9	0.72	19.2	3.5
LST 003B	0.41	2.9	0.43	5.1	0.9
LST 004	0.36	2.9	0.55	14.8	4.1
LST 005	0.34	2.7	0.55	14.4	3.9
LST 006	0.32	2.6	0.47	11.3	4.1
LST 007	0.3	2	0.35	7.6	4.9
LST 007A	0.29	2.2	0.4	9.4	4.6
LST 008	0.28	1.9	0.29	4.6	6.4
SAMPLE A	0.61	5.3	0.98	30.8	5.6
SAMPLE B	0.28	2	0.35	7.8	4.9
SAMPLE C	0.34	2.8	0.52	14.3	3.8
SAMPLE D	0.31	2	0.31	4.9	6.9
LST1 TS	0.38	2.6	0.43	7.5	4.6

Report Number: A19-02357

Report Date: 10/5/2019

Analyte Symbol	W	Tl	Pb	Bi	Th
Unit Symbol	ppm	ppm	ppm	ppm	ppm
Detection Limit	1	0.1	5	0.4	0.1
Analysis Method	FUS-MS	FUS-MS	FUS-MS	FUS-MS	FUS-MS
LST 001	< 1	1.1	52	0.4	95.6
LST 001A	< 1	0.9	45	< 0.4	65
LST 002	< 1	1.1	47	< 0.4	89.3
LST 002A	< 1	0.9	37	< 0.4	59.3
LST 003	< 1	1	47	0.4	79.7
LST 003A	< 1	0.8	27	< 0.4	49.1
LST 003B	< 1	0.6	15	< 0.4	11.1
LST 004	< 1	0.6	24	< 0.4	35.7
LST 005	< 1	0.5	25	< 0.4	35.7
LST 006	< 1	0.4	20	< 0.4	28.2
LST 007	< 1	0.2	14	< 0.4	16.8
LST 007A	< 1	0.3	15	< 0.4	21
LST 008	2	0.1	10	< 0.4	8.6
SAMPLE A	< 1	0.9	42	< 0.4	78.6
SAMPLE B	< 1	0.2	13	< 0.4	17.2
SAMPLE C	< 1	0.5	22	< 0.4	35.1
SAMPLE D	< 1	0.1	8	< 0.4	8.8
LST1 TS	1	0.4	30	< 0.4	13.4

Report Number: A19-02357

Report Date: 10/5/2019

Analyte Symbol	U	Os	Ir	Ru	Rh
Unit Symbol	ppm	ppb	ppb	ppb	ppb
Detection Limit	0.1	2	0.1	5	0.2
Analysis Method	FUS-MS	NI-FINA	NI-FINA	NI-FINA	NI-FINA
LST 001	26.2	< 2	< 0.1	< 5	< 0.2
LST 001A	18.1	< 2	< 0.1	< 5	< 0.2
LST 002	24.8	< 2	< 0.1	< 5	< 0.2
LST 002A	16.2	< 2	0.2	< 5	< 0.2
LST 003	22.1	< 2	< 0.1	< 5	< 0.2
LST 003A	13.4	< 2	< 0.1	< 5	< 0.2
LST 003B	2.8	< 2	< 0.1	< 5	< 0.2
LST 004	9.6	< 2	< 0.1	< 5	< 0.2
LST 005	9.4	< 2	< 0.1	< 5	< 0.2
LST 006	7.4	9	< 0.1	< 5	< 0.2
LST 007	4.3	< 2	< 0.1	< 5	< 0.2
LST 007A	5.4	< 2	< 0.1	< 5	< 0.2
LST 008	2.2	< 2	< 0.1	< 5	< 0.2
SAMPLE A	21.6	< 2	< 0.1	< 5	< 0.2
SAMPLE B	4.5	< 2	< 0.1	< 5	< 0.2
SAMPLE C	9.4	< 2	< 0.1	< 5	< 0.2
SAMPLE D	2.3	< 2	< 0.1	< 5	< 0.2
LST1 TS	3.5	< 2	< 0.1	< 5	< 0.2

Report Number: A19-02357

Report Date: 10/5/2019

Analyte Symbol	Pt	Pd	Au	Mass
Unit Symbol	ppb	ppb	ppb	g
Detection Limit	5	2	0.5	
Analysis Method	NI-FINA	NI-FINA	NI-FINA	NI-FINA
LST 001	< 5	< 2	0.7	25
LST 001A	< 5	< 2	0.8	25
LST 002	< 5	< 2	< 0.5	25
LST 002A	< 5	< 2	0.8	25
LST 003	< 5	< 2	1	25
LST 003A	< 5	< 2	1.1	25
LST 003B	< 5	< 2	2.6	25
LST 004	< 5	< 2	1.4	25
LST 005	< 5	< 2	1.1	25
LST 006	< 5	< 2	0.7	25
LST 007	< 5	< 2	1.4	25
LST 007A	< 5	< 2	0.6	25
LST 008	< 5	< 2	< 0.5	25
SAMPLE A	< 5	< 2	< 0.5	25
SAMPLE B	< 5	< 2	0.5	25
SAMPLE C	< 5	< 2	1.1	25
SAMPLE D	< 5	< 2	0.7	25
LST1 TS	< 5	< 2	4.3	25

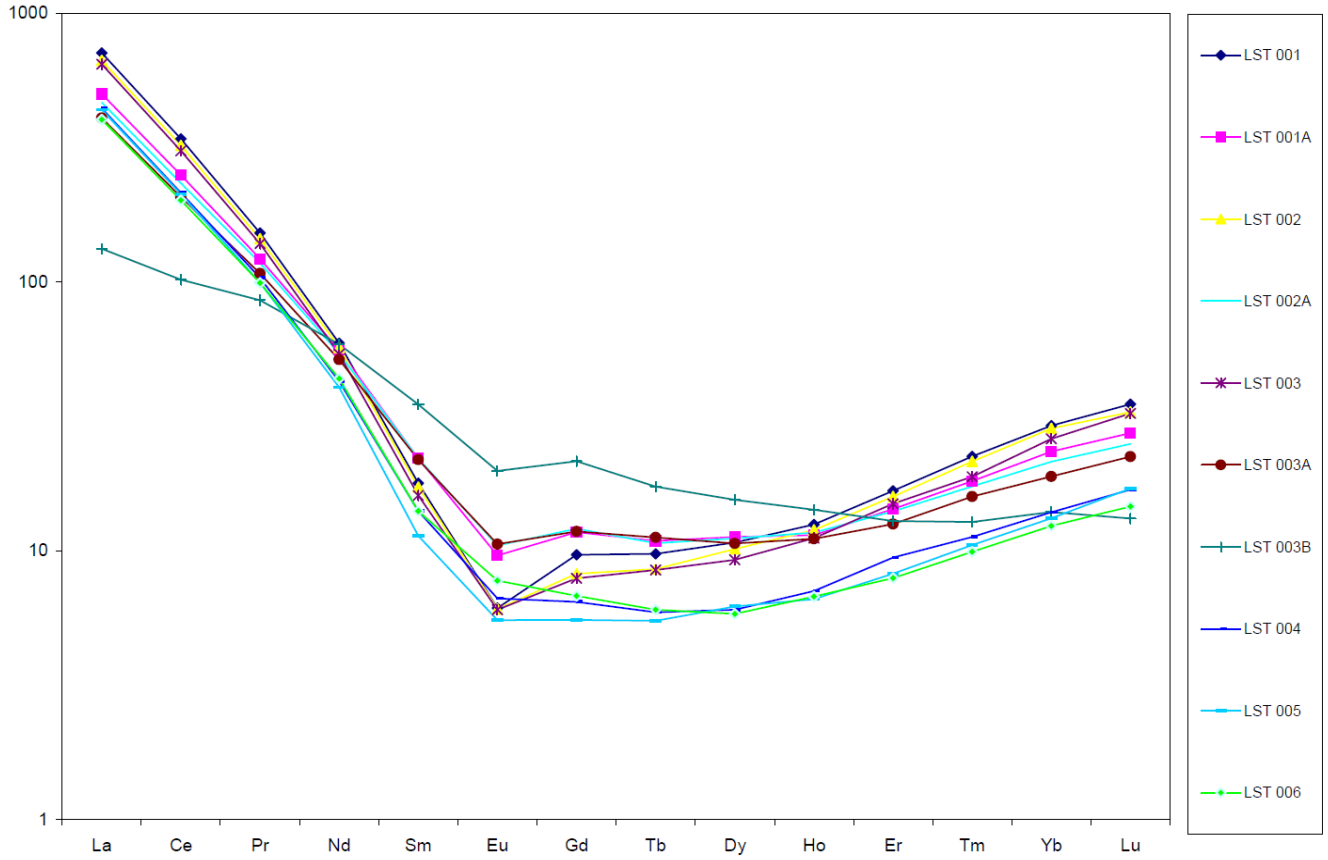
1000
100
10
1
La
Ce
Pr
Nd
Sm
Eu
Gd
Tb
Dy
Ho
Er
Tm
Yb
Lu
LST 001
LST 001A
LST 002
LST 002A
LST 003
LST 003A
LST 003B
LST 004
LST 005
LST 006

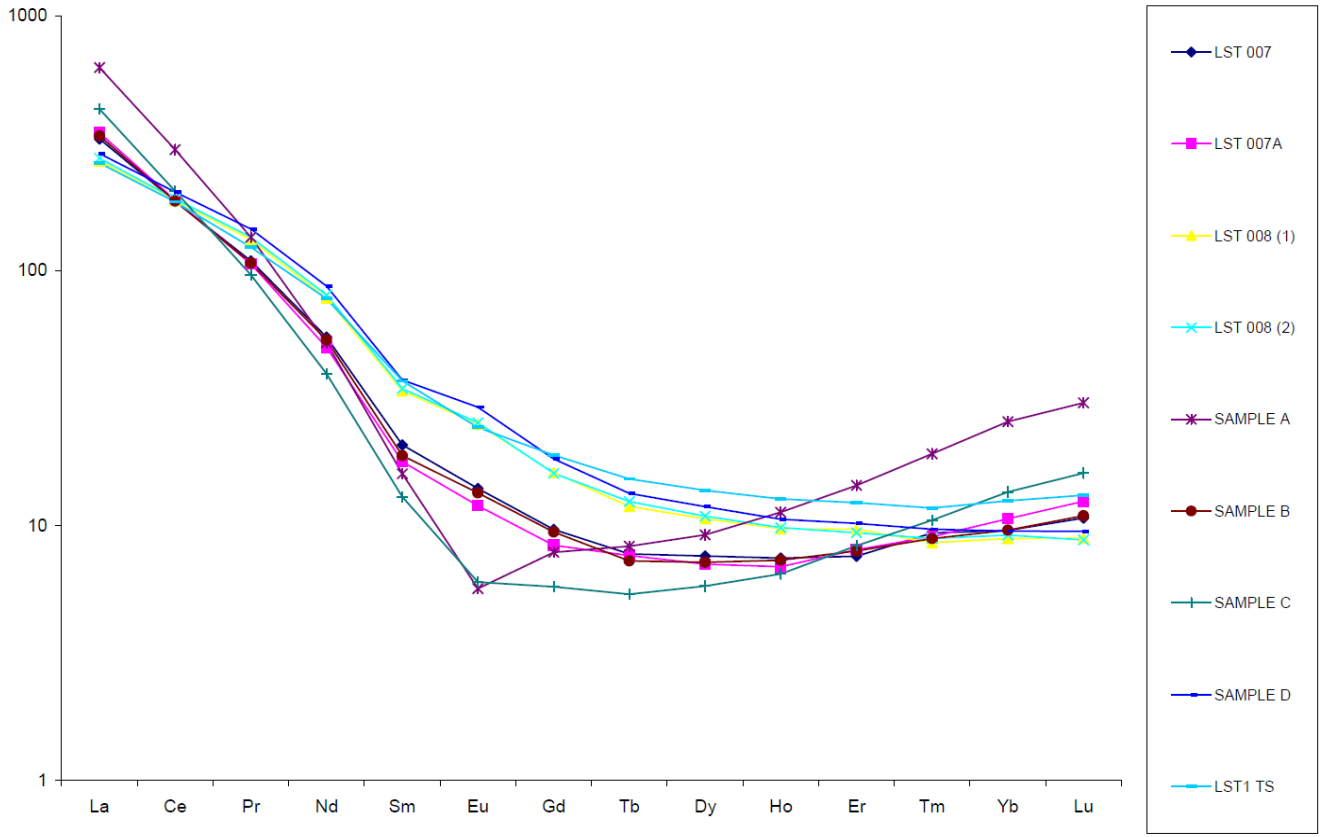
1000
100
10
1
La
Ce
Pr
Nd
Sm
Eu
Gd
Tb
Dy
Ho
Er
Tm
Yb
Lu
LST 007
LST 007A
LST 008 (1)
LST 008 (2)
SAMPLE A
SAMPLE B
SAMPLE C
SAMPLE D
LST1 TS

Bibliography

Abbott, P.M. and Davies, S.M., 2012. Volcanism and the Greenland ice-cores: the tephra record. *Earth Science Reviews*, *115*(3), pp.173-191.

ActLabs, 2019. *Lithogeochemistry and Whole Rock Analysis.* Activation Laboratories, viewed 25th March 2019 < https://actlabs.com/geochemistry/lithogeochemistry-and-whole-rock-analysis/>

Aiuppa, A., Baker, D.R. and Webster, J.D., 2009. Halogens in volcanic systems. *Chemical Geology*, 263(1-4), pp.1-18.

Aiuppa, A., Dongarrà, G., Valenza, M., Federico, C. and Pecoraino, G., 2003. Degassing of trace volatile metals during the 2001 eruption of Etna. *Washington DC American Geophysical Union Geophysical Monograph Series*, *139*, pp.41-54.

Alley, R. B., 2000: The Younger Dryas cold interval as viewed from central Greenland. *Quaternary Science Reviews, 19,* pp. 213–226.

Alley, R.B. and Clark, P.U., 1999. The deglaciation of the northern hemisphere: a global perspective. *Annual Review of Earth and Planetary Sciences*, *27*(1), pp.149-182.

Anders, E. and Grevesse, N., 1989. Abundances of the elements: Meteoritic and solar. *Geochimica et Cosmochimica acta*, *53*(1), pp.197-214.

Andersen, K.K., Svensson, A., Johnsen, S.J., Rasmussen, S.O., Bigler, M., Röthlisberger, R., Ruth, U., Siggaard-Andersen, M.L., Steffensen, J.P., Dahl-Jensen, D. and Vinther, B.M., 2006. The Greenland ice core chronology 2005, 15–42 ka. Part 1: constructing the time scale. *Quaternary Science Reviews*, *25*(23-24), pp.3246-3257.

Andronikov, A.V., Rudnickaitė, E., Lauretta, D.S., Andronikova, I.E., Kaminskas, D., Šinkūnas, P. and Melešytė, M., 2015. Geochemical evidence of the presence of volcanic and meteoritic materials in Late Pleistocene lake sediments of Lithuania. *Quaternary International*, *386*, pp.18-29.

Andronikov, A.V., Subetto, D.A., Lauretta, D.S., Andronikova, I.E., Drosenko, D.A., Kuznetsov, D.D., Sapelko, T.V. and Syrykh, L.S., 2014, July. In search for fingerprints of an extraterrestrial event: Trace element characteristics of sediments from the lake Medvedevskoye (Karelian Isthmus, Russia). In *Doklady Earth Sciences* (Vol. 457, No. 1, pp. 819-823). Pleiades Publishing.

Andronikov, A.V., Van Hoesel, A., Andronikova, I.E. and Hoek, W.Z., 2016. Trace element distribution and implications in sediments across the Allerød–Younger Dryas boundary in the Netherlands and Belgium. *Geografiska Annaler: Series A, Physical Geography*, *98*(4), pp.325-345.

Baales, M., Jöris, O., Street, M., Bittmann, F., Weninger, B. and Wiethold, J., 2002. Impact of the Late Glacial eruption of the Laacher See volcano, central Rhineland, Germany. *Quaternary Research*, *58*(3), pp.273-288.

Baldini, J.U., Brown, R.J. and McElwaine, J.N., 2015a. Was millennial scale climate change during the Last Glacial triggered by explosive volcanism? *Scientific reports*, *5*, p.17442.

Baldini, J.U., Brown, R.J. and Mawdsley, N., 2018. Evaluating the link between the sulfur-rich Laacher See volcanic eruption and the Younger Dryas climate anomaly. *Climate of the Past*, *14*(7), pp.969-990.

Baldini, L.M., McDermott, F., Baldini, J.U., Arias, P., Cueto, M., Fairchild, I.J., Hoffmann, D.L., Mattey, D.P., Müller, W., Nita, D.C. and Ontañón, R., 2015b. Regional temperature, atmospheric circulation, and sea-ice variability within the Younger Dryas Event constrained using a speleothem from northern Iberia. *Earth and Planetary Science Letters*, *419*, pp.101-110.

Bales, R., Dibb, J. and Neftel, A., 1992. The GISP2 ice core and snow-atmosphere chemical exchange. *Eos, Transactions American Geophysical Union*, *73*(19), pp.213-213.

Barker, S., Chen, J., Gong, X., Jonkers, L., Knorr, G. and Thornalley, D., 2015. Icebergs not the trigger for North Atlantic cold events. *Nature*, *520*(7547), p.333.

Barnes, S.J., Naldrett, A.J. and Gorton, M.P., 1985. The origin of the fractionation of platinum-group elements in terrestrial magmas. *Chemical Geology*, *53*(3-4), pp.303-323.

Bender, M., Sowers, T. and Brook, E., 1997. Gases in ice cores. *Proceedings of the National Academy of Sciences*, *94*(16), pp.8343-8349.

Berger, W. H., 1990. The Younger Dryas cold spell – a quest for causes. *Global Planetary Change, 89,* pp. 219–237*.*

Bogaard, P.V. and Schmincke, H.U., 1985. Laacher See Tephra: A widespread isochronous late Quaternary tephra layer in central and northern Europe. *Geological Society of America Bulletin*, *96*(12), pp.1554-1571.

Boslough, M.B., 2001. Impact-induced climate change due to an orbiting debris ring. In *ISDC 2001: The National Space Society's 20 th Annual International Space Development Conference*.

Boslough, M., 2013. Greenland Pt anomaly may point to noncataclysmic Cape York meteorite entry. *Proceedings of the National Academy of Sciences*, *110*(52), pp.E5035-E5035.

Boslough, M., Harris, A.W., Chapman, C. and Morrison, D., 2013. Younger Dryas impact model confuses comet facts, defies airburst physics. *Proceedings of the National Academy of Sciences*, *110*(45), pp.E4170-E4170.

Boyle, E.A. and Keigwin, L., 1987. North Atlantic thermohaline circulation during the past 20,000 years linked to high-latitude surface temperature. *Nature*, *330*(6143), pp.35-40.

Brauer, A., Endres, C., Günter, C., Litt, T., Stebich, M. and Negendank, J.F., 1999a. High resolution sediment and vegetation responses to Younger Dryas climate

change in varved lake sediments from Meerfelder Maar, Germany. *Quaternary Science Reviews*, *18*(3), pp.321-329.

Brauer, A., Endres, C. and Negendank, J.F., 1999b. Lateglacial calendar year chronology based on annually laminated sediments from Lake Meerfelder Maar, Germany. *Quaternary International*, *61*(1), pp.17-25.

Brauer, A., Haug, G.H., Dulski, P., Sigman, D.M. and Negendank, J.F., 2008. An abrupt wind shift in western Europe at the onset of the Younger Dryas cold period. *Nature Geoscience*, *1*(8), p.520.

Broecker, W.S., Kennett, J.P., Flower, B.P., Teller, J.T., Trumbore, S., Bonani, G. and Wolfli, W., 1989. Routing of meltwater from the Laurentide Ice Sheet during the Younger Dryas cold episode. *Nature, 341,* pp. 318-321.

Broecker, W.S., 2006a. Was the Younger Dryas triggered by a flood?. *Science*, *312*(5777), pp.1146-1148.

Broecker, W.S., 2006b. Abrupt climate change revisited. *Global and Planetary Change*, *54*(3-4), pp.211-215.

Broecker, W.S., Denton, G.H., Edwards, R.L., Cheng, H., Alley, R.B. and Putnam, A.E., 2010. Putting the Younger Dryas event into context. *Quaternary Science Reviews*, *29*, pp. 1078-1081.

Buchwald, V.F., 1975. Handbook of iron meteorites. *Theier History, Distribuition*.

Buizert, C., Gkinis, V., Severinghaus, J.P., He, F., Lecavalier, B.S., Kindler, P., Leuenberger, M., Carlson, A.E., Vinther, B., Masson-Delmotte, V. and White, J.W., 2014. Greenland temperature response to climate forcing during the last deglaciation. *Science*, *345*(6201), pp.1177-1180.

Cadoux, A., Scaillet, B., Bekki, S., Oppenheimer, C. and Druitt, T.H., 2015. Stratospheric ozone destruction by the Bronze-Age Minoan eruption (Santorini volcano, Greece). *Scientific reports*, *5*, p.12243.

Carlson, A.E., 2013. The Younger Dryas Climate Event. In: Elias S.A. (ed.) *The Encyclopedia of Quaternary Science, vol. 3, pp. 126-134*. Amsterdam: Elsevier

Carroll, M.R. and Rutherford, M.J., 1985. Sulfide and sulfate saturation in hydrous silicate melts. *Journal of Geophysical Research: Solid Earth*, *90*(S02), pp.C601-C612.

Chiang, J.C., Lee, S.Y., Putnam, A.E. and Wang, X., 2014. South Pacific Split Jet, ITCZ shifts, and atmospheric North–South linkages during abrupt climate changes of the last glacial period. *Earth and Planetary Science Letters*, 406, pp.233-246.

Chyba, C.F., Thomas, P.J. and Zahnle, K.J., 1993. The 1908 Tunguska explosion: atmospheric disruption of a stony asteroid. *Nature*, *361*(6407), p.40.

Clark, P.U., Dyke, A.S., Shakun, J.D., Carlson, A.E., Clark, J., Wohlfarth, B., Mitrovica, J.X., Hostetler, S.W. and McCabe, A.M., 2009. The last glacial maximum. *Science*, *325*(5941), pp.710-714.

Clark, P.U., Marshall, S.J., Clarke, G.K., Hostetler, S.W., Licciardi, J.M. and Teller, J.T., 2001. Freshwater forcing of abrupt climate change during the last glaciation. *Science*, *293*(5528), pp.283-287.

Clark, P.U., Shakun, J.D., Baker, P.A., Bartlein, P.J., Brewer, S., Brook, E., Carlson, A.E., Cheng, H., Kaufman, D.S., Liu, Z. and Marchitto, T.M., 2012. Global climate evolution during the last deglaciation. *Proceedings of the National Academy of Sciences*, *109*(19), pp.E1134-E1142.

Condron, A. and Winsor, P., 2012. Meltwater routing and the Younger Dryas. *Proceedings of the National Academy of Sciences*, *109*(49), pp.19928-19933.

Costa, A., Folch, A. and Macedonio, G., 2010. A model for wet aggregation of ash particles in volcanic plumes and clouds: 1. Theoretical formulation. *Journal of Geophysical Research: Solid Earth*, *115*(B9).

Coulter, S.E., Pilcher, J.R., Plunkett, G., Baillie, M., Hall, V.A., Steffensen, J.P., Vinther, B.M., Clausen, H.B. and Johnsen, S.J., 2012. Holocene tephras highlight complexity of volcanic signals in Greenland ice cores. *Journal of Geophysical Research: Atmospheres*, *117*(D21).

Crocket, J.H., 1972. Some aspects of the geochemistry of Ru, Os, Ir and Pt in iron meteorites. *Geochimica et Cosmochimica Acta*, *36*(5), pp.517-535.

Crowe, B.M., Finnegan, D.L., Zoller, W.H. and Boynton, W.V., 1987. Trace element geochemistry of volcanic gases and particles from 1983–1984 eruptive episodes of Kilauea volcano. *Journal of Geophysical Research: Solid Earth, 92*(B13), pp.13708-13714.

Cuffey, K.M. and Clow, G.D., 1997. Temperature, accumulation, and ice sheet elevation in central Greenland through the last deglacial transition. *Journal of Geophysical Research: Oceans*, *102*(C12), pp.26383-26396.

Daulton, T.L., Pinter, N. and Scott, A.C., 2010. No evidence of nanodiamonds in Younger–Dryas sediments to support an impact event. *Proceedings of the National Academy of Sciences*, *107*(37), pp.16043-16047.

Day, J.M., 2013. Hotspot volcanism and highly siderophile elements. *Chemical Geology*, *341*, pp.50-74.

De Angelis, M., Steffensen, J.P., Legrand, M., Clausen, H. and Hammer, C., 1997. Primary aerosol (sea salt and soil dust) deposited in Greenland ice during the last climatic cycle: Comparison with east Antarctic records. *Journal of Geophysical Research: Oceans*, *102*(C12), pp.26681-26698.

Denniston, R.F., Wyrwoll, K.H., Polyak, V.J., Brown, J.R., Asmerom, Y., Wanamaker Jr, A.D., LaPointe, Z., Ellerbroek, R., Barthelmes, M., Cleary, D. and Cugley, J., 2013. A stalagmite record of Holocene Indonesian–Australian summer monsoon variability from the Australian tropics. *Quaternary Science Reviews*, *78*, pp.155-168.

Denton, G.H., Anderson, R.F., Toggweiler, J.R., Edwards, R.L., Schaefer, J.M. and Putnam, A.E., 2010. The last glacial termination. *Science*, *328*(5986), pp.1652-1656.

Diallo, M., Ploeger, F., Konopka, P., Birner, T., Müller, R., Riese, M., Garny, H., Legras, B., Ray, E., Berthet, G. and Jégou, F., 2017. Significant contributions of

volcanic aerosols to decadal changes in the stratospheric circulation. *Geophysical Research Letters, 44*(20), pp.10-780.

Edmonds, M. and Mather, T.A., 2017. Volcanic sulfides and outgassing. *Elements*, *13*(2), pp.105-110.

Eichler, A., Schwikowski, M. and Gäggeler, H.W., 2001. Meltwater-induced relocation of chemical species in Alpine firn. *Tellus B: Chemical and Physical Meteorology*, *53*(2), pp.192-203.

EPICA Community Members., Barbante, C., Barnola, J.M., Becagli, S., Beer, J., Bigler, M., Boutron, C., Blunier, T., Castellano, E., Cattani, O. and Chappellaz, J., 2006. One-to-one coupling of glacial climate variability in Greenland and Antarctica. *Nature*, *444*(7116), p.195.

European Project for Ice Coring in Antarctica Community Members, 2006. One-to-one coupling of glacial climate variability in Greenland and Antarctica. *Nature*, *444*(7116), pp.195-198.

Evans, N.J., Gregoire, D.C. and Goodfellow, W.D., 1993a. Use of platinum-group elements for impactor identification: Terrestrial impact craters and Cretaceous-Tertiary boundary. *Geochimica et Cosmochimica Acta, 57*(15), pp.3737-3748.

Evans, N.J., Gregoire, D.C., Goodfellow, W.D., McInnes, B.I., Miles, N. and Veizer, J.Á.N., 1993b. Ru/Ir ratios at the Cretaceous-Tertiary boundary: Implications for PGE source and fractionation within the ejecta cloud. *Geochimica et Cosmochimica Acta, 57*(13), pp.3149-3158.

Firestone, R. B., West, A., Kennett, J. P., Becker, L., Bunch, T. E., Revay, Z. S., Schultz, P. H., Belgya, T., Kennett, D. J., Erlandson, J. M., Dickenson, O. J., Goodyear, A. C., Harris, R. S., Howard, G. A., Kloosterman, J. B., Lechler, P., Mayewski, P. A., Montgomery, J., Poreda, R., Darrah, T., Hee, S. S. Q., Smitha, A. R., Stich, A., Topping,W.,Wittke, J. H., and Wolbach, W. S., 2007. Evidence for an extraterrestrial impact 12,900 years ago that contributed to the megafaunal extinctions and the Younger Dryas cooling. *Proceedings of the National Academy of Sciences, 104*(41), pp. 16016–16021

Firestone, R.B., West, A., Revay, Zs., Hagstrum, J.T., Belgya, T., Que Hee, S.S., Smith, A.R., 2010. Analysis of the Younger Dryas impact layer. *Journal of Siberian Federal University, Engineering & technologies, 3(1),* pp. 30-62

Fisher, T.G., Yansa, C.H., Lowell, T.V., Lepper, K., Hajdas, I. and Ashworth, A., 2008. The chronology, climate, and confusion of the Moorhead Phase of glacial Lake Agassiz: new results from the Ojata Beach, North Dakota, USA. *Quaternary Science Reviews*, *27*(11-12), pp.1124-1135.

Floss, C. and Crozaz, G., 1991. Ce anomalies in the LEW85300 eucrite: evidence for REE mobilization during Antarctic weathering. *Earth and Planetary Science Letters*, *107*(1), pp.13-24.

Folch, A., Costa, A., Durant, A. and Macedonio, G., 2010. A model for wet aggregation of ash particles in volcanic plumes and clouds: 2. Model application. *Journal of Geophysical Research: Solid Earth*, *115*(B9).

Fritts, H.C., 1966. Growth-rings of trees: their correlation with climate. *Science*, *154*(3752), pp.973-979.

Fuchs, N.A., 1989. *The mechanics of aerosols.* Dover Publications.

Gabrielli, P., Barbante, C., Plane, J.M., Boutron, C.F., Jaffrezo, J.L., Mather, T.A., Stenni, B., Gaspari, V., Cozzi, G., Ferrari, C. and Cescon, P., 2008. Siderophile metal fallout to Greenland from the 1991 winter eruption of Hekla (Iceland) and during the global atmospheric perturbation of Pinatubo. *Chemical Geology*, *255*(1-2), pp.78-86.

Gabrielli, P., Barbante, C., Carturan, L.U.C.A., Cozzi, G., Dalla Fontana, G., Dinale, R., Draga, G., Gabrieli, J., Kehrwald, N., Mair, V. and Mikhalenko, V.N., 2012. Discovery of cold ice in a new drilling site in the Eastern European Alps. *Geografia Fisica e Dinamica Quaternaria*, *35*(1), pp.101-105.

Gabrielli, P. and Vallelonga, P., 2015. Contaminant records in ice cores. In *Environmental Contaminants* (pp. 393-430). Springer, Dordrecht.

Gao, C., Oman, L., Robock, A. and Stenchikov, G.L., 2007. Atmospheric volcanic loading derived from bipolar ice cores: Accounting for the spatial distribution of volcanic deposition. *Journal of Geophysical Research: Atmospheres*, *112*(D9).

Gat, J.R., 1996. Oxygen and hydrogen isotopes in the hydrologic cycle. *Annual Review of Earth and Planetary Sciences*, *24*(1), pp.225-262.

Gautier, E., Savarino, J., Erbland, J., Lanciki, A. and Possenti, P., 2016. Variability of sulfate signal in ice core records based on five replicate cores. *Climate of the Past*, *12*(1), pp.103-113.

GeoRoc, 2019. *Geochemistry of Rocks of the Oceans and Continents (GeoRoc) electronic database.* Max Planck Institute for Chemistry (Mainz). [Online] Available from: http://georoc.mpch-mainz.gwdg.de/georoc/ (Last accessed: 28 February 2019).

GERM, 2019. Geochemical Earth Reference Model (GERM) electronic database. [Online] Available from: https://earthref.org/GERM/ (Last accessed: 14 December 2018).

Gnos, E., Hofmann, B.A., Al-Kathiri, A., Lorenzetti, S., Eugster, O., Whitehouse, M.J., Villa, I.M., Jull, A.T., Eikenberg, J., Spettel, B. and Krähenbühl, U., 2004. Pinpointing the source of a lunar meteorite: Implications for the evolution of the Moon. *Science*, *305*(5684), pp.657-659.

Goujon, C., Barnola, J.M. and Ritz, C., 2003. Modeling the densification of polar firn including heat diffusion: Application to close-off characteristics and gas isotopic fractionation for Antarctica and Greenland sites. *Journal of Geophysical Research: Atmospheres*, *108*(D24).

Graf, H.F. and Timmreck, C., 2001. A general climate model simulation of the aerosol radiative effects of the Laacher See eruption (10,900 BC). *Journal of Geophysical Research: Atmospheres*, *106*(D14), pp.14747-14756.

Hajdas, I., Ivy-Ochs, S.D., Bonani, G., Loiter, A.F., Zolitschka, B. and Schlüchter, C., 1995. Radiocarbon age of the Laacher See tephra: 11,230±40 BP. *Radiocarbon*, *37*(2), pp.149-154.

Hampson Jr, R.F. and Walker, R.F., 1961. Vapor pressures of platinum, iridium, and rhodium. *J. of Res. of the NBS--A. Physics and Chemistry*, *65*(4).

Harms, E. and Schmincke, H.U., 2000. Volatile composition of the phonolitic Laacher See magma (12,900 yr BP): implications for syn-eruptive degassing of S, F, Cl and H 2 O. *Contributions to Mineralogy and Petrology*, *138*(1), pp.84-98.

Harper, J., Humphrey, N., Pfeffer, W.T., Brown, J. and Fettweis, X., 2012. Greenland ice-sheet contribution to sea-level rise buffered by meltwater storage in firn. *Nature, 491*(7423), p.240.

Haynes Jr, C.V., 2005. Clovis, pre-Clovis, climate change, and extinction. *Paleoamerican Origins: Beyond Clovis*, pp.113-132.

Hinkley, T.K., 1991. Distribution of metals between particulate and gaseous forms in a volcanic plume. *Bulletin of volcanology*, *53*(5), pp.395-400.

Hoffman, E.L., 1992. Instrumental neutron activation in geoanalysis. Journal of *Geochemical Exploration, 44(1-3*), pp.297-319.

Hoffman, E.L. and Dunn, B., 2002. Sample preparation and bulk analytical methods for PGE. *The Geology, Geochemistry, Mineralogy and Mineral Beneficiation of Platinum-Group Elements (LJ Cabri ed.). Can. Inst. Min. Metall. Spec*, *54*, pp.1-11.

Hoffman, E.L., Naldrett, A.J., Van Loon, J.C., Hancock, R.G.V. and Manson, A., 1978. The determination of all the platinum group elements and gold in rocks and ore by neutron activation analysis after preconcentration by a nickel sulphide fire-assay technique on large samples. *Analytica Chimica Acta*, *102*, pp.157-166.

Holliday, V., Surovell, T. and Johnson, E., 2016. A blind test of the Younger Dryas impact hypothesis. *PloS one*, *11*(7), p.e0155470.

Hough, R.M., Gilmour, I., Pillinger, C.T., Langenhorst, F. and Montanari, A., 1997. Diamonds from the iridium-rich KT boundary layer at Arroyo el Mimbral, Tamaulipas, Mexico. *Geology*, *25*(11), pp.1019-1022.

Johnson, R.G. and McClure, B.T., 1976. A model for Northern Hemisphere continental ice sheet variation. *Quaternary Research, 6, 973–985.*

Kennett, D.J., Kennett, J.P., West, A., Mercer, C., Hee, S.Q., Bement, L., Bunch, T.E., Sellers, M. and Wolbach, W.S., 2009. Nanodiamonds in the Younger Dryas boundary sediment layer. *Science*, *323*(5910), pp.94-94.

Kennett, J.P. and Shackleton, N.J., 1975. Laurentide ice sheet meltwater recorded in Gulf of Mexico deep-sea cores. *Science*, *188*(4184), pp.147-150.

Kinzie, C.R., Que Hee, S.S., Stich, A., Tague, K.A., Mercer, C., Razink, J.J., Kennett, D.J., DeCarli, P.S., Bunch, T.E., Wittke, J.H. and Israde-Alcantara, I., 2014.

Nanodiamond-rich layer across three continents consistent with major cosmic impact at 12,800 cal BP. *The Journal of Geology*, *122*(5), pp.475-506.

Kjær, K.H., Larsen, N.K., Binder, T., Bjørk, A.A., Eisen, O., Fahnestock, M.A., Funder, S., Garde, A.A., Haack, H., Helm, V. and Houmark-Nielsen, M., 2018. A large impact crater beneath Hiawatha Glacier in northwest Greenland. *Science advances*, *4*(11), p.eaar8173.

Koeberl, C., 1986. Geochemistry of tektites and impact glasses. *Annual Review of Earth and Planetary Sciences, 14(*1), pp.323-350.

Lane, C.S., Brauer, A., Blockley, S.P. and Dulski, P., 2013. Volcanic ash reveals time-transgressive abrupt climate change during the Younger Dryas. *Geology*, *41*(12), pp.1251-1254.

Lane, C.S., Brauer, A., Martín-Puertas, C., Blockley, S.P., Smith, V.C. and Tomlinson, E.L., 2015. The Late Quaternary tephrostratigraphy of annually laminated sediments from Meerfelder Maar, Germany. *Quaternary Science Reviews*, *122*, pp.192-206.

Langmann, B., 2014. On the role of climate forcing by volcanic sulphate and volcanic ash. *Advances in Meteorology*, 2014.

Lehner, F., Born, A., Raible, C.C. and Stocker, T.F., 2013. Amplified inception of European Little Ice Age by sea ice–ocean–atmosphere feedbacks. *Journal of climate*, *26*(19), pp.7586-7602.

Legrand, M. and Mayewski, P., 1997. Glaciochemistry of polar ice cores: a review. *Reviews of geophysics*, *35*(3), pp.219-243.

Leydet, D.J., Carlson, A.E., Teller, J.T., Breckenridge, A., Barth, A.M., Ullman, D.J., Sinclair, G., Milne, G.A., Cuzzone, J.K. and Caffee, M.W., 2018. Opening of glacial Lake Agassiz's eastern outlets by the start of the Younger Dryas cold period. *Geology*, *46*(2), pp.155-158.

Lorand, J.P., Luguet, A. and Alard, O., 2008. Platinum-group elements: a new set of key tracers for the Earth's interior. *Elements*, *4*(4), pp.247-252.

Lotter, A.F., Birks, H.J.B. and Zolitschka, B., 1995. Late-glacial pollen and diatom changes in response to two different environmental perturbations: volcanic eruption and Younger Dryas cooling. *Journal of Paleolimnology*, *14*(1), pp.23-47.

Lotter, A.F., Eicher, U., Siegenthaler, U. and Birks, H.J.B., 1992. Late-glacial climatic oscillations as recorded in Swiss lake sediments. *Journal of Quaternary Science*, *7*(3), pp.187-204.

Lowe, D.J., 2011. Tephrochronology and its application: a review. *Quaternary Geochronology*, *6*(2), pp.107-153.

Lowe, J.J. and Walker, M.J., 2014. *Reconstructing quaternary environments*. Routledge.

Lowell, T., Waterson, N., Fisher, T., Loope, H., Glover, K., Comer, G., Hajdas, I., Denton, G., Schaefer, J., Rinterknecht, V. and Broecker, W., 2005. Testing the Lake Agassiz meltwater trigger for the Younger Dryas. *Eos, Transactions American Geophysical Union*, *86*(40), pp.365-372.

Mahaney, W.C., Somelar, P., West, A., Krinsley, D., Allen, C.C., Pentlavalli, P., Young, J.M., Dohm, J.M., LeCompte, M., Kelleher, B. and Jordan, S.F., 2017. Evidence for cosmic airburst in the Western Alps archived in Late Glacial paleosols. *Quaternary International*, *438*, pp.68-80.

Martín-Peinado, F.J. and Rodríguez-Tovar, F.J., 2010. Mobility of iridium in terrestrial environments: implications for the interpretation of impact-related mass-extinctions. *Geochimica et Cosmochimica Acta, 74*(15), pp.4531-4542.

Mather, T.A., Pyle, D.M. and Oppenheimer, C., 2003. Tropospheric volcanic aerosol. *Geophysical Monograph-American Geophysical Union*, *139*, pp.189-212.

Mather, T.A., Witt, M.L.I., Pyle, D.M., Quayle, B.M., Aiuppa, A., Bagnato, E., Martin, R.S., Sims, K.W.W., Edmonds, M., Sutton, A.J. and Ilyinskaya, E., 2012. Halogens and trace metal emissions from the ongoing 2008 summit eruption of Kīlauea volcano, Hawaii. *Geochimica et Cosmochimica Acta*, *83*, pp.292-323.

Mayewski, P.A., Meeker, L.D., Twickler, M.S., Whitlow, S., Yang, Q., Lyons, W.B. and Prentice, M., 1997. Major features and forcing of high-latitude northern hemisphere atmospheric circulation using a 110,000-year-long glaciochemical series. *Journal of Geophysical Research: Oceans*, *102*(C12), pp.26345-26366.

Mayewski, P.A., Meeker, L.D., Whitlow, S.L., Twickler, M.S., Morrison, M.C., Bloomfield, P., Bond, G.C., Alley, R.B., Gow, A.J., Meese, D.A. and Grootes, P.M., 1994. Changes in atmospheric circulation and ocean ice cover over the North Atlantic during the last 41,000 years. *Science*, *263*(5154), pp.1747-1751.

McDonough, W.F. and Sun, S.S., 1995. The composition of the Earth. *Chemical geology*, *120*(3-4), pp.223-253.

McManus, J.F., Francois, R., Gherardi, J.M., Keigwin, L.D. and Brown-Leger, S., 2004. Collapse and rapid resumption of Atlantic meridional circulation linked to deglacial climate changes. *Nature*, *428*(6985), p.834.

Meese, D.A., Gow, A.J., Alley, R.B., Zielinski, G.A., Grootes, P.M., Ram, M., Taylor, K.C., Mayewski, P.A. and Bolzan, J.F., 1997. The Greenland Ice Sheet Project 2 depth-age scale: methods and results. *Journal of Geophysical Research: Oceans*, *102*(C12), pp.26411-26423.

Meissner, K.J. and Clark, P.U., 2006. Impact of floods versus routing events on the thermohaline circulation. *Geophysical Research Letters*, *33*(15).

Melosh, H. J. (1982) The mechanics of large meteoroid impacts in the Earth's oceans. In *Geological Implications of Impacts of Large Asteroids and Comets on the Earth* (ed. Silver, L.T. and Schultz, P.H.); GSA Spec. Paper 190, pp. 121-127.

Meltzer, D.J., Holliday, V.T., Cannon, M.D. and Miller, D.S., 2014. Chronological evidence fails to support claim of an isochronous widespread layer of cosmic impact

indicators dated to 12,800 years ago. *Proceedings of the National Academy of Sciences*, *111*(21), pp.E2162-E2171.

Mercer, J.H., 1969. The Alleröd oscillation: A European climatic anomaly?. *Arctic and Alpine Research*, *1*(4), pp.227-234.

MetBase, 2019. *Meteorite Information Database (Metbase) electronic database.* GeoPlatform UG, Germany. [Online] Available from: http://www.metbase.org (Last accessed: 26 April 2019).

Miller, G.H., Geirsdóttir, Á., Zhong, Y., Larsen, D.J., Otto-Bliesner, B.L., Holland, M.M., Bailey, D.A., Refsnider, K.A., Lehman, S.J., Southon, J.R. and Anderson, C., 2012. Abrupt onset of the Little Ice Age triggered by volcanism and sustained by sea-ice/ocean feedbacks. *Geophysical Research Letters*, *39*(2).

Mohan, S.M., 2016. An overview of particulate dry deposition: measuring methods, deposition velocity and controlling factors. *International journal of environmental science and technology*, *13*(1), pp.387-402.

Moore, C.R., West, A., LeCompte, M.A., Brooks, M.J., Daniel Jr, I.R., Goodyear, A.C., Ferguson, T.A., Ivester, A.H., Feathers, J.K., Kennett, J.P. and Tankersley, K.B., 2017. Widespread platinum anomaly documented at the Younger Dryas onset in North American sedimentary sequences. *Scientific reports*, *7*, p.44031.

Mortensen, A.K., Bigler, M., Grönvold, K., Steffensen, J.P. and Johnsen, S.J., 2005. Volcanic ash layers from the Last Glacial Termination in the NGRIP ice core. *Journal of Quaternary Science: Published for the Quaternary Research Association*, *20*(3), pp.209-219.

Mountain, B.W. and Wood, S.A., 1988. Chemical controls on the solubility, transport and deposition of platinum and palladium in hydrothermal solutions; a thermodynamic approach. *Economic Geology*, *83*(3), pp.492-510.

Mungall, J.E., Brenan, J.M., Godel, B., Barnes, S.J. and Gaillard, F., 2015. Transport of metals and sulphur in magmas by flotation of sulphide melt on vapour bubbles. *Nature Geoscience*, *8*(3), p.216.

Mungall, J.E. and Naldrett, A.J., 2008. Ore deposits of the platinum-group elements. *Elements*, *4*(4), pp.253-258.

Murton, J.B., Bateman, M.D., Dallimore, S.R., Teller, J.T. and Yang, Z., 2010. Identification of Younger Dryas outburst flood path from Lake Agassiz to the Arctic Ocean. *Nature*, *464*(7289), p.740.

Muschitiello, F., Pausata, F.S., Watson, J.E., Smittenberg, R.H., Salih, A.A., Brooks, S.J., Whitehouse, N.J., Karlatou-Charalampopoulou, A. and Wohlfarth, B., 2015. Fennoscandian freshwater control on Greenland hydroclimate shifts at the onset of the Younger Dryas. *Nature Communications*, *6*, p.8939.

Napier, B., Asher, D., Bailey, M. and Steel, D., 2015. Centaurs as a hazard to civilization. *Astronomy & Geophysics*, *56*(6), pp.6-24.

Nozaki, Y., 1997. A fresh look at element distribution in the North Pacific Ocean. *EOS Trans., American Geophysical Union*, *78*, p.221.

Olausson, E., 1963. Evidence of climatic changes in North Atlantic deep-sea cores, with remarks on isotopic paleotemperature analysis. *Progress in oceanography*, *3*, pp.221-252.

Oppenheimer, C., 2003. Ice core and palaeoclimatic evidence for the timing and nature of the great mid-13th century volcanic eruption. *International Journal of Climatology: A Journal of the Royal Meteorological Society*, *23*(4), pp.417-426.

Paquay, F.S., Goderis, S., Ravizza, G., Vanhaeck, F., Boyd, M., Surovell, T.A., Holliday, V.T., Haynes, C.V. and Claeys, P., 2009. Absence of geochemical evidence for an impact event at the Bølling–Allerød/Younger Dryas transition. *Proceedings of the National Academy of Sciences*, *106*(51), pp.21505-21510.

Park C, Schmincke H-U (2019 in press). Multistage damming of the Rhine River by tephra fallout during the 12,900 BP Plinian Laacher See Eruption (Germany). Syn-eruptive Rhine damming. *International Journal of Volcanology and Geothermal Research*.

Pašava, J., Vymazalová, A. and Petersen, S., 2007. PGE fractionation in seafloor hydrothermal systems: examples from mafic-and ultramafic-hosted hydrothermal fields at the slow-spreading Mid-Atlantic Ridge. *Mineralium Deposita*, *42*(4), pp.423-431.

Petaev, M.I. and Jacobsen, S.B., 2004. Differentiation of metal-rich meteoritic parent bodies: I. Measurements of PGEs, Re, Mo, W, and Au in meteoritic Fe-Ni metal. *Meteoritics & Planetary Science*, *39*(10), pp.1685-1697.

Petaev, M.I., Huang, S., Jacobsen, S.B. and Zindler, A., 2013. Large Pt anomaly in the Greenland ice core points to a cataclysm at the onset of Younger Dryas. *Proceedings of the National Academy of Sciences*, *110*(32), pp.12917-12920.

Pino, M., Abarzúa, A.M., Astorga, G., Martel-Cea, A., Cossio-Montecinos, N., Navarro, R.X., Lira, M.P., Labarca, R., LeCompte, M.A., Adedeji, V. and Moore, C.R., 2019. Sedimentary record from Patagonia, southern Chile supports cosmic-impact triggering of biomass burning, climate change, and megafaunal extinctions at 12.8 ka. *Scientific reports*, *9*(1), p.4413.

Pinter, N., Scott, A.C., Daulton, T.L., Podoll, A., Koeberl, C., Anderson, R.S. and Ishman, S.E., 2011. The Younger Dryas impact hypothesis: A requiem. *Earth-Science Reviews*, *106*(3), pp.247-264.

Pinto, J.P., Turco, R.P. and Toon, O.B., 1989. Self-limiting physical and chemical effects in volcanic eruption clouds. *Journal of Geophysical Research: Atmospheres, 94*(D8), pp.11165-11174.

Pitari, G., Di Genova, G., Mancini, E., Visioni, D., Gandolfi, I. and Cionni, I., 2016. Stratospheric aerosols from major volcanic eruptions: a composition-climate model study of the aerosol cloud dispersal and e-folding time. *Atmosphere*, *7*(6), p.75.

Ponette-González, A.G., Collins, J.D., Manuel, J.E., Byers, T.A., Glass, G.A., Weathers, K.C. and Gill, T.E., 2018. Wet dust deposition across Texas during the

2012 drought: An overlooked pathway for elemental flux to ecosystems. *Journal of Geophysical Research: Atmospheres*, *123*(15), pp.8238-8254.

Pope, K.O., Baines, K.H., Ocampo, A.C. and Ivanov, B.A., 1997. Energy, volatile production, and climatic effects of the Chicxulub Cretaceous/Tertiary impact. *Journal of Geophysical Research: Planets*, *102*(E9), pp.21645-21664.

Rasmussen, S.O., Andersen, K.K., Svensson, A.M., Steffensen, J.P., Vinther, B.M., Clausen, H.B., Siggaard-Andersen, M.L., Johnsen, S.J., Larsen, L.B., Dahl-Jensen, D. and Bigler, M., 2006. A new Greenland ice core chronology for the last glacial termination. Journal of Geophysical Research: Atmospheres, 111(D6).

Rasmussen, S.O., Bigler, M., Blockley, S.P., Blunier, T., Buchardt, S.L., Clausen, H.B., Cvijanovic, I., Dahl-Jensen, D., Johnsen, S.J., Fischer, H. and Gkinis, V., 2014. A stratigraphic framework for abrupt climatic changes during the Last Glacial period based on three synchronized Greenland ice-core records: refining and extending the INTIMATE event stratigraphy. *Quaternary Science Reviews*, *106*, pp.14-28.

Rach, O., Brauer, A., Wilkes, H. and Sachse, D., 2014. Delayed hydrological response to Greenland cooling at the onset of the Younger Dryas in western Europe. *Nature Geoscience*, *7*(2), p.109.

Rampino, M.R. and Self, S., 1984. Sulphur-rich volcanic eruptions and stratospheric aerosols. *Nature*, *310*(5979), p.677.

Rauch, S. and Morrison, G.M., 2008. Environmental relevance of the platinum-group elements. *Elements*, *4*(4), pp.259-263.

Rehkämper, M., Halliday, A.N., Barfod, D., Fitton, J.G. and Dawson, J.B., 1997. Platinum-group element abundance patterns in different mantle environments. *Science*, *278*(5343), pp.1595-1598.

Renssen, H., van Geel, B., van der Plicht, J. and Magny, M., 2000. Reduced solar activity as a trigger for the start of the Younger Dryas?. *Quaternary International*, *68*, pp.373-383.

Renssen, H., Mairesse, A., Goosse, H., Mathiot, P., Heiri, O., Roche, D.M., Nisancioglu, K.H. and Valdes, P.J., 2015. Multiple causes of the Younger Dryas cold period. *Nature Geoscience, 8(12),* p.946.

Riede, F., 2016. Changes in mid-and far-field human landscape use following the Laacher See eruption (c. 13,000 BP). *Quaternary International*, *394*, pp.37-50.

Robock, A., Ammann, C.M., Oman, L., Shindell, D., Levis, S. and Stenchikov, G., 2009. Did the Toba volcanic eruption of~ 74 ka BP produce widespread glaciation?. *Journal of Geophysical Research: Atmospheres, 114(*D10).

Robock, A. and Mao, J., 1995. The volcanic signal in surface temperature observations. *Journal of Climate*, *8*(5), pp.1086-1103.

Robock, A., 2000. Volcanic eruptions and climate. *Reviews of geophysics*, *38*(2), pp.191-219.

Robock, A., 2002. The climatic aftermath. *Science*, *295*(5558), pp.1242-1244.

Rooth, C., 1982. Hydrology and ocean circulation. *Progress in Oceanography, 11,* pp. 131–149.

Russell, P.B., Livingston, J.M., Pueschel, R.F., Bauman, J.J., Pollack, J.B., Brooks, S.L., Hamill, P., Thomason, L.W., Stowe, L.L., Deshler, T. and Dutton, E.G., 1996. Global to microscale evolution of the Pinatubo volcanic aerosol derived from diverse measurements and analyses. *Journal of Geophysical Research: Atmospheres, 101*(D13), pp.18745-18763.

Salamatin, A.N. and Lipenkov, V.Y., 2008. Simple relations for the close-off depth and age in dry-snow densification. *Annals of Glaciology*, *49*, pp.71-76.

Sawlowicz, Z., 1993. Iridium and other platinum-group elements as geochemical markers in sedimentary environments. *Palaeogeography, Palaeoclimatology, Palaeoecology*, *104*(1-4), pp.253-270.

Schenk, F., Väliranta, M., Muschitiello, F., Tarasov, L., Heikkilä, M., Björck, S., Brandefelt, J., Johansson, A.V., Näslund, J.O. and Wohlfarth, B., 2018. Warm summers during the Younger Dryas cold reversal. *Nature Communications*, *9*(1), p.1634.

Schmincke, H.U., 2004. *Volcanism* (Vol. 28). Springer Science & Business Media.

Schmincke, H.U., Park, C. and Harms, E., 1999. Evolution and environmental impacts of the eruption of Laacher See Volcano (Germany) 12,900 a BP. *Quaternary International, 61(1*), pp.61-72.

Schmitt, A.K., Wetzel, F., Cooper, K.M., Zou, H. and Wörner, G., 2010. Magmatic longevity of Laacher See Volcano (Eifel, Germany) indicated by U–Th dating of intrusive carbonatites. *Journal of Petrology*, *51*(5), pp.1053-1085.

Schneider, D.P., Ammann, C.M., Otto-Bliesner, B.L. and Kaufman, D.S., 2009. Climate response to large, high-latitude and low-latitude volcanic eruptions in the Community Climate System Model. *Journal of Geophysical Research: Atmospheres*, *114*(D15).

Scott, E.R.D. and Krot, A.N., 2014. Chondrites and Their Components. In: Holland, H.D. and Turekian, K.K. eds. *Treatise on Geochemistry.* Elsevier, pp. 9144.

Seierstad, I.K., Abbott, P.M., Bigler, M., Blunier, T., Bourne, A.J., Brook, E., Buchardt, S.L., Buizert, C., Clausen, H.B., Cook, E. and Dahl-Jensen, D., 2014. Consistently dated records from the Greenland GRIP, GISP2 and NGRIP ice cores for the past 104 ka reveal regional millennial-scale δ18O gradients with possible Heinrich event imprint. *Quaternary Science Reviews*, *106*, pp.29-46.

Serreze, M.C. and Francis, J.A., 2006. The Arctic amplification debate. *Climatic change*, *76*(3-4), pp.241-264.

Shakun, J.D. and Carlson, A.E., 2010. A global perspective on Last Glacial Maximum to Holocene climate change. *Quaternary Science Reviews*, *29*(15), pp.1801-1816.

Shinohara, H., 2008. Excess degassing from volcanoes and its role on eruptive and intrusive activity. *Reviews of Geophysics*, *46*(4).

Sigmarsson, O., Haddadi, B., Carn, S., Moune, S., Gudnason, J., Yang, K. and Clarisse, L., 2013. The sulfur budget of the 2011 Grímsvötn eruption, Iceland. *Geophysical Research Letters*, *40*(23), pp.6095-6100.

Sima, A., Paul, A. and Schulz, M., 2004. The Younger Dryas—an intrinsic feature of late Pleistocene climate change at millennial timescales. *Earth and Planetary Science Letters, 222*(3-4), pp.741-750.

Sime, L.C., Hopcroft, P.O. and Rhodes, R.H., 2019. Impact of abrupt sea ice loss on Greenland water isotopes during the last glacial period. *Proceedings of the National Academy of Sciences*, *116*(10), pp.4099-4104.

Simon, A.C. and Pettke, T., 2009. Platinum solubility and partitioning in a felsic melt–vapor–brine assemblage. *Geochimica et cosmochimica acta, 73(2),* pp.438-454.

Soyol-Erdene, T.O., Huh, Y., Hong, S. and Hur, S.D., 2011. A 50-year record of platinum, iridium, and rhodium in Antarctic snow: volcanic and anthropogenic sources. *Environmental science & technology*, *45*(14), pp.5929-5935.

Sun, N., Brandon, A., Forman, S.L., Waters, M.R. and Stafford Jr., T.W., 2018. Highly siderophile elements and Os isotope constraints on the Younger Dryas Impact Hypothesis: A case study from Hall's Cave, Texas. In: Geological Society of America Annual Meeting; 2018 Nov 4-7, Indianapolis, Indiana, USA. Geological Society of America *Abstracts with Programs.*, *50*(6)

Sutherland, R.A., Pearson, D.G. and Ottley, C.J., 2007. Platinum-group elements (Ir, Pd, Pt and Rh) in road-deposited sediments in two urban watersheds, Hawaii. *Applied Geochemistry, 22(7),* pp.1485-1501.

Svensson, A., Andersen, K.K., Bigler, M., Clausen, H.B., Dahl-Jensen, D., Davies, S.M., Johnsen, S.J., Muscheler, R., Rasmussen, S.O., Röthlisberger, R. and Steffensen, J.P., 2006. The Greenland ice core chronology 2005, 15–42 ka. Part 2: comparison to other records. *Quaternary Science Reviews*, *25*(23-24), pp.3258-3267.

Symonds, R.B., Reed, M.H. and Rose, W.I., 1992. Origin, speciation, and fluxes of trace-element gases at Augustine volcano, Alaska: Insights into magma degassing and fumarolic processes. *Geochimica et Cosmochimica Acta, 56(2),* pp.633-657.

Tagle, R., Erzinger, J., Hecht, L., Schmitt, R.T., Stöffler, D. and Claeys, P., 2004. Platinum group elements in impactites of the ICDP Chicxulub drill core Yaxcopoil-1: Are there traces of the projectile?. Meteoritics & Planetary Science, 39(6), pp.1009-1016.

Tankersley, K.B., Dunning, N.P., Owen, L.A., Huff, W.D., Park, J.H., Kim, C., Lentz, D.L. and Sparks-Stokes, D., 2018. Positive Platinum anomalies at three late Holocene high magnitude volcanic events in Western Hemisphere sediments. *Scientific reports*, *8*(1), p.11298.

Teller, J.T. and Leverington, D.W., 2004. Glacial Lake Agassiz: A 5000 yr history of change and its relationship to the δ18O record of Greenland. *Geological Society of America Bulletin*, *116*(5-6), pp.729-742.

Teller, J.T., Boyd, M., Yang, Z., Kor, P.S. and Fard, A.M., 2005. Alternative routing of Lake Agassiz overflow during the Younger Dryas: new dates, paleotopography, and a re-evaluation. *Quaternary Science Reviews*, *24*(16-17), pp.1890-1905.

Textor, C., Graf, H.F., Timmreck, C. and Robock, A., 2003. Emissions from volcanoes. In *Emissions of Atmospheric Trace Compounds* (pp. 269-303). Springer, Dordrecht.

Timmreck, C., Graf, H.F. and Steil, B., 2004. Aerosol chemistry interactions after the Mt. Pinatubo eruption. *Volcanism and the Earth's Atmosphere, 139*, pp.213-225.

Timmreck, C., Graf, H.F., Zanchettin, D., Hagemann, S., Kleinen, T. and Krüger, K., 2012. Climate response to the Toba super-eruption: Regional changes. *Quaternary International*, *258*, pp.30-44.

Toohey, M., Krüger, K., Schmidt, H., Timmreck, C., Sigl, M., Stoffel, M. and Wilson, R., 2019. Disproportionately strong climate forcing from extratropical explosive volcanic eruptions. *Nature Geoscience*, *12*(2), p.100.

Toon, O.B., Zahnle, K., Morrison, D., Turco, R.P. and Covey, C., 1997. Environmental perturbations caused by the impacts of asteroids and comets. *Reviews of Geophysics*, *35*(1), pp.41-78.

van den Bogaard, P. and Schmincke, H.U., 1985. Laacher See Tephra: A widespread isochronous late Quaternary tephra layer in central and northern Europe. *Geological Society of America Bulletin*, *96*(12), pp.1554-1571.

van den Bogaard, P., Schmincke, H.U., Freundt, A., and Park, C.: Thera and the Aegean World, Third International Congress, Santorini, Greece, 463–485, 1989.

Van Hoesel, A., Hoek, W.Z., Pennock, G.M. and Drury, M.R., 2014. The Younger Dryas impact hypothesis: a critical review. *Quaternary Science Reviews*, *83*, pp.95-114.

Vinther, B.M., Clausen, H.B., Johnsen, S.J., Rasmussen, S.O., Andersen, K.K., Buchardt, S.L., Dahl-Jensen, D., Seierstad, I.K., Siggaard-Andersen, M.L., Steffensen, J.P. and Svensson, A., 2006. A synchronized dating of three Greenland ice cores throughout the Holocene. *Journal of Geophysical Research: Atmospheres*, *111*(D13).

Wagnon, P., Delmas, R.J. and Legrand, M., 1999. Loss of volatile acid species from upper firn layers at Vostok, Antarctica. *Journal of Geophysical Research: Atmospheres*, *104*(D3), pp.3423-3431.

Warming, E., Svensson, A., Vallelonga, P. and Bigler, M., 2013. A technique for continuous detection of drill liquid in ice cores. *Journal of glaciology*, *59*(215), pp.503-506.

Wasson, J.T., 1999. Trapped melt in IIIAB irons; solid/liquid elemental partitioning during the fractionation of the IIIAB magma. *Geochimica et Cosmochimica Acta*, *63*(18), pp.2875-2889.

Wasson, J.T., Huber, H. and Malvin, D.J., 2007. Formation of IIAB iron meteorites. *Geochimica et Cosmochimica Acta*, *71*(3), pp.760-781.

Wedepohl, K.H., 1995. The composition of the continental crust. *Geochimica et cosmochimica Acta*, *59*(7), pp.1217-1232.

White, W.M., 2013. *Geochemistry*. Wiley-Blackwell

Wittke, J.H., Weaver, J.C., Bunch, T.E., Kennett, J.P., Kennett, D.J., Moore, A.M., Hillman, G.C., Tankersley, K.B., Goodyear, A.C., Moore, C.R. and Daniel, I.R., 2013. Evidence for deposition of 10 million tonnes of impact spherules across four

continents 12,800 y ago. *Proceedings of the National Academy of Sciences*, *110*(23), pp.E2088-E2097.

Wolbach, W.S., Ballard, J.P., Mayewski, P.A., Adedeji, V., Bunch, T.E., Firestone, R.B., French, T.A., Howard, G.A., Israde-Alcántara, I., Johnson, J.R., Kimbel, D., Kinzie, C.R., Kurbatov, A., Kletetschka, G., LeCompte, M.A., Mahaney, W.C., Melott, A.L., Maiorana-Boutilier, A., Mitra, S., Moore, C.R., Napier, W.M., Parlier, J., Tankersley, K.B., Thomas, B.C., Wittke, J.H., West, A. and Kennett, J.P., 2018a. Extraordinary biomass-burning episode and impact winter triggered by the Younger Dryas cosmic impact~ 12,800 years ago. 1. Ice cores and glaciers. *The Journal of Geology*, *126*(2), pp.165-184.

Wolbach, W.S., Ballard, J.P., Mayewski, P.A., Parnell, A.C., Cahill, N., Adedeji, V., Bunch, T.E., Domínguez-Vázquez, G., Erlandson, J.M., Firestone, R.B., French, T.A., Howard, G., Israde-Alcántara, Johnson, J.R., Kimbel, D., Kinzie, C.R., Kurbatov, A., Kletetschka, G., LeCompte, M.A., Mahaney, W.C., Melott, A.L., A., Mitra, A.L., Maiorana-Boutilier, A., Moore, C.R., Napier, W.M., Parlier, J., Tankersley, K.B., Thomas, B.C., Wittke, J.H., West, A. and Kennett, J.P., 2018b. Extraordinary biomass-burning episode and impact winter triggered by the Younger Dryas cosmic impact~ 12,800 years ago. 2. Lake, marine, and terrestrial sediments. *The Journal of Geology*, *126*(2), pp.185-205.

Wörner, G. and Schmincke, H.U., 1984. Mineralogical and chemical zonation of the Laacher See tephra sequence (East Eifel, W. Germany). *Journal of Petrology*, *25*(4), pp.805-835.

Wörrier, G., Beusen, J.M., Duchateau, N., Gijbels, R. and Schmincke, H.U., 1983. Trace element abundances and mineral/melt distribution coefficients in phonolites from the Laacher See Volcano (Germany). *Contributions to Mineralogy and Petrology*, *84*(2-3), pp.152-173.

Wu, Y., Sharma, M., LeCompte, M.A., Demitroff, M.N. and Landis, J.D., 2013. Origin and provenance of spherules and magnetic grains at the Younger Dryas boundary. *Proceedings of the National Academy of Sciences*, *110*(38), pp.E3557-E3566.

Wunsch, C., 2006. Abrupt climate change: An alternative view. *Quaternary Research*, *65*(02), pp.191-203.

Zhang, X., Lohmann, G., Knorr, G. and Purcell, C., 2014. Abrupt glacial climate shifts controlled by ice sheet changes. *Nature, 512(7514),* p.290.

Zhang, X., Knorr, G., Lohmann, G. and Barker, S., 2017. Abrupt North Atlantic circulation changes in response to gradual CO 2 forcing in a glacial climate state. *Nature Geoscience, 10(7),* p.518.

Zhu, H., Bozdağ, E., Peter, D. and Tromp, J., 2012. Structure of the European upper mantle revealed by adjoint tomography. *Nature Geoscience*, *5*(7), p.493.

Zielinski, G.A., Mayewski, P.A., Meeker, L.D., Whitlow, S. and Twickler, M.S., 1996. A 110,000-yr record of explosive volcanism from the GISP2 (Greenland) ice core. *Quaternary Research, 45(2),* pp.109-118.

Zoller, W.H., Parrington, J.R. and Kotra, J.M.P., 1983. Iridium enrichment in airborne particles from Kilauea volcano: January 1983. *Science*, *222*(4628), pp.1118-1121.